UNIVERSIDADE D
COIMBRA

Pedro Ricardo Palma Mina da Cruz

Stator Fault Diagnosis in Six-Phase Permanent Magnet Synchronous Machines Under Transient Conditions

Dissertation under the scope of the Master's Degree in Electrical and Computer Engineering, specialisation in Energy, supervised by Prof. Dr. Sérgio Manuel Ângelo da Cruz and presented to the Department of Electrical and Computer Engineering of the Faculty of Sciences and Technology of the University of Coimbra

July 2023

UNIVERSIDADE D
COIMBRA

Department of Electrical and Computer Engineering
Faculty of Sciences and Technology
University of Coimbra

Stator Fault Diagnosis in Six-Phase Permanent Magnet Synchronous Machines Under Transient Conditions

Pedro Ricardo Palma Mina da Cruz

Members of the jury:

President: Prof. Dr. Mário João Simões Ferreira dos Santos
Vocal: Prof. Dr. Fernando José Teixeira Estêvão Ferreira
Supervisor: Prof. Dr. Sérgio Manuel Ângelo da Cruz

July 2023

For my parents and grandparents

Acknowledgements

I am deeply grateful to my advisor, Dr. Sérgio Cruz, for his determined support and guidance throughout this dissertation. His expertise and insight have been invaluable to me and have played a crucial role in the success of this thesis.

I am grateful to Instituto de Telecomunicações for all the material provided, as well as to Direção Geral do Ensino Superior, for making it possible for me to continue my studies and come to college, by granting me a scholarship. I would like to extend a special thanks to Dr. Pedro Gonçalves, who worked on this very same machine since its conception, developing it over the past years to what it is now, and that was always made available to lend a helping hand.

I am deeply thankful to my friends and family for their love and support, not only during this thesis, but throughout my life. Without their encouragement and motivation, without all the fun and laughter and the welcome day-to-day distractions, I would not have been able to complete this journey.

I would also like to thank my colleagues at the Laboratório de Sistemas Eletromecânicos for their friendship and words of encouragement during the duration of this thesis.

Lastly, I am grateful to everyone who has supported me throughout my education, since when I was just a little kid until this very moment. Without your influence, I would never have gotten here.

Abstract

In the past couple of decades the permanent magnet synchronous machine (PMSM) has gained great attention due to some inherent advantages such as its high torque density, high power density and high efficiency. The development of multiphase PMSMs (m-PMSM), such as the six-phase asymmetrical configuration, has further extended the potential of PMSMs for high-reliability applications, for instance in safety and mission-critical systems, where the increased fault-tolerance brought by this machine is much required. However, these advanced arrangements are not immune to faults, such as interturn short-circuits (ITSCs) in the stator windings, which can result in catastrophic failures if left undetected. Additionally, the applications where these machines are used mostly involve accelerations/decelerations and load torque variations, which make the fault diagnosis more challenging. To detect, and locate, the interturn short-circuit, under non-stationary conditions, two methods were developed in this thesis. The first method makes use of the short-time Fourier transform (STFT) and a novel order-tracking technique to extract the related fault features. The second method makes use of the multiple reference frames (MRF) theory to directly extract the same fault features. Experimental results demonstrate that both methods are effective and sensitive in the detection of ITSCs, in both speed varying and load torque varying conditions. These techniques improve the reliability of six-phase PMSM drive systems ensuring a safe operation under stationary and non-stationary conditions.

Resumo

Nos últimos anos, a máquina síncrona de ímanes permanentes tem ganho grande atenção devido a vantagens que lhe são inerentes, como a alta densidade de binário, a alta densidade de potência e a elevada eficiência. O desenvolvimento de máquinas multifásicas, como a configuração de seis fases assimétrica, tem estendido o potencial da máquina síncrona de ímanes permanentes para aplicações que requerem um elevado grau de fiabilidade, por exemplo em sistemas de segurança critica, onde a elevada tolerância a falhas característica desta máquina é fortemente necessária. No entanto, estas configurações avançadas não são totalmente imunes a falhas, como é o caso do curto-circuito entre as espiras dos enrolamentos do estator, que pode causar avarias catastróficas se não for detetado a tempo. Adicionalmente, as aplicações onde estas máquinas são utilizadas envolvem maioritariamente acelerações/desacelerações, o que aumenta a dificuldade na deteção da falha. Para detetar, e localizar, um curto-circuito entre espiras, em regime transitório, foram desenvolvidos dois métodos nesta dissertação. O primeiro método faz uso da transformada de Fourier de curto termo aliada a uma técnica de pesquisa de ordens harmónicas por forma a extrair a informação relativa à falha. O segundo método por sua vez faz uso da teoria de referenciais múltiplos para extrair diretamente a informação relativa à falha, sem a necessidade de utilizar técnicas de tempo-frequência. Os resultados experimentais permitem concluir que ambos os métodos são sensíveis na deteção do curto-circuito entre espiras, tanto em condições de velocidade variável como também de binário de carga variável. Estas técnicas aqui desenvolvidas aumentam a fiabilidade em acionamentos de máquinas síncronas de ímanes permanentes com seis fases, assegurando uma maior segurança quando a máquina funciona tanto em regime permanente, como em regime transitório.

Contents

List of Tables

List of Figures

List of Symbols

a	Wavelet scaling factor	
b	Wavelet translation factor	
e_α, i_β	Induced voltages in the alpha and beta-axis	V
e_d, e_q	Induced voltages in the direct and quadrature-axis	V
f	Frequency	Hz
f_c	Cutoff frequency	Hz
f_s	Supply frequency	Hz
f_{sh}	Stator teeth harmonics	Hz
f_{ss}	Stator slot harmonics	Hz
f_t	Space harmonics	Hz
h	Window function	
$H(x)$	Hilbert transform of signal x	
i_α, i_β	Currents in the alpha and beta-axis	A
i_d, i_q	Currents in the direct and quadrature-axis	A
i_f	Fault current	A
J	Coupling matrix	
k	Number of locations in time at each level	
l	Number of levels of resolution	
L	Self-inductance	H
L_{dq}	Inductance in the direct-and quadrature-axis	H
L_{xy}	Inductance in the xy-axis	H
L_{z12}	Inductance in the z1z2-axis	H
M	Mutual inductance	H
μ	Ratio between N_f and N_t	
N_t	Number of turns per winding	
N_f	Number of shorted turns	
N_{ss}	Number of stator slots	
n	Counter for the number of W intervals	
ω_m	Mechanical angular frequency	rad/s
ω_r	Electrical angular frequency	rad/s
p	Position signal	deg
p'	New position signal	deg
p'_{norm}	Normalisation of the new position signal	
Φ	Kernel	
ϕ	Initial phase angle	rad
Ψ^0_{PM}	Zero sequence no-load flux linkage	Wb
Ψ_{PM}	No-load flux linkage	Wb
ψ	Mother wavelet	

R_f	Fault Resistance	Ω
R_s	Stator Resistance	Ω
s_0	DWT positive constant 2	
T_s	Sampling Period	s
t	Time variable	s
τ_0	DWT positive constant 1	
τ	Time axis of a time-frequency representation	s
U_{dc}	DC-link voltage	V
u^0	Zero sequence component voltage	V
u_α, u_β	Voltages in the alpha-and beta-axis	V
u_d, u_q	Voltages in the direct-and quadrature-axis	V
v	Consecutive positive integers	
v_o	Consecutive positive odd integers	
W	Position sampling width	deg
x	Generic signal	
y	Spatial Domain Transform output signal	

List of Acronyms

AC	Alternating Current
AI	Artificial Intelligence
CW	Choi-Williams Distribution
CWT	Continuous Wavelet Transform
DC	Direct Current
DFT	Discrete Fourier Transform
DTC	Direct Torque Control
DWT	Discrete Wavelet Transform
EMD	Empirical Mode Decomposition
EEMD	Ensemble Empirical Mode Decomposition
EMF	Electromotive Force
EKF	Extended Kalman Filter
ESO	Extended State Observer
FEA	Finite Element Analysis
FEM	Finite Element Method
FFT	Fast Fourier Transform
FI	Fault Index
FOC	Field Oriented Control
FS	Fault Severity
HT	Hilbert Transform
IM	Induction Machine
LPF	Low-Pass Filter
LSPMSM	Line-Start Permanent Magnet Synchronous Machine
ITSC	Interturn Short-circuit
m-PMSM	Multiphase Permanent Magnet Synchronous Machine
MCSA	Motor Current Signature Analysis
MVSA	Motor Voltage Signature Analysis
MMF	Magnetomotive Force
MRA	Multiple Resolution Analysis
MRF	Multiple Reference Frames
MUSIC	Multiple Signal Classification
PCC	Predictive Current Control
PM	Permanent Magnet
PMSM	Permanent Magnet Synchronous Machine
PWM	Pulse-Width Modulation
PWV	Pseudo Wigner-Ville Distribution
RMS	Root Mean Square

SDT	Spatial-Domain Transform
SPWV	Smoothed Pseudo Wigner-Ville Distribution
STFT	Short-Time Fourier Transform
TFR	Time-frequency Representation
UMP	Unbalanced Magnetic Pull
VSD	Vector Space Decomposition
WT	Wavelet Transform
WV	Wigner-Ville Distribution
ZAM	Zhao-Atlas-Marks Distribution
ZSVC	Zero-Sequence Voltage Component

"In any given moment we have two options: to step forward into growth or back into safety."

—*Abraham Maslow*

Chapter 1

Introduction

The worldwide demand to minimise carbon emissions as lead to rapid advancements in the field of electrical machines and drives. Systems that consume hydraulic, pneumatic, and mechanical power are now being replaced by electrical systems, which reduce fuel consumption, operating costs, acoustic noise, to name a few advantages.

Among all electrical machines, PMSMs have emerged as a popular choice in various applications, including the so called "more-electric" initiative, which originated in the aerospace industry, with the goal of transitioning aircraft from hydraulic and pneumatic systems to electrically driven systems. The inclination towards PMSMs is a result of its intrinsic characteristics such as high-power and high-torque densities, which effectively downsize the dimensions of the machine as well as its weight and increase its efficiency, due to the elimination of copper losses in the rotor. Classical three-phase PMSMs have been extensively studied in the literature and are currently used in various applications. However, some limitations of these machines, such as a low fault tolerance, have motivated researchers to seek for other alternatives. One of such alternatives is the six-phase PMSM (6-PMSM). This configuration can be either symmetrical, where the two sets of three-phase windings are spatially shifted by 60°, or asymmetrical, where the two sets are spatially shifted by 30° [1]. Multiphase PMSMs (m-PMSMs) offer several advantages over their three-phase counterparts, including increased fault tolerance and higher torque density. In fact, in the event of a single phase or winding failure, a 6-PMSM can continue to operate with diminished performance. On the other hand, a 3-PMSM would come to a complete stop in the presence of such fault. Since 6-PMSMs possess two separate three–phase winding groups, these machines can be supplied from two separate inverters with reduced power rating, alleviating the electrical stress and thermal dissipation in the power devices [2].

1.1 Motivation

Regardless of their advantages, m-PMSMs are not immune to the destructive nature of interturn short-circuits (ITSCs), which are one of the most severe faults in electric machinery. These faults arise due to the degradation of the windings insulation system which is mostly caused by electrical and thermal stresses. An ITSC increases the working temperature of the machine, which may have implications for the rotor permanent magnets, and can lead to more severe types of short-circuits, eventually resulting in the catastrophic failure of the machine, and potentially endangering human safety, taking into account the different safety critical applications this machine is contemplated for, such as traction, wind energy systems and the aerospace industry. In fact, most of these applications are set under non-stationary operating conditions, which poses as an obstacle to the detection of such type of faults.

While the detection of ITSCs in traditional three-phase PMSMs has gathered a considerable amount of attention throughout the years, most existing research focuses on stationary operating conditions [3], [4].

The majority of these techniques are signal-based methods applied to the analysis of the stator currents [5]–[7] as well as the stator voltages [8]. In fact, the most recognised fault detection method is the Motor Current Signature Analysis (MCSA), followed by the Motor Voltage Signature Analysis (MVSA). These methods make use of the Fast Fourier Transform (FFT) to extract certain fault signatures (features). Other signals used in signal-based methods include the flux, electromagnetic torque and active/reactive power [3]. Unfortunately, most of the aforementioned methods are only applicable when the machine is working under stationary operating conditions, due to the employment of the FFT. Some methods can detect the ITSCs under non-stationary conditions through the usage of time-frequency representations (TFRs), replacing the FFT, such as the Short-Time Fourier Transform [9], the Wavelet Transform (WT) [10], [11] and other more complex TFRs [12].

Another methodology used for the detection of ITSCs relies on mathematical modelling to estimate certain parameters such as the back electromotive force (back-EMF) [13] and the resistance and inductance [4]. These model-based methods can overcome the dynamic conditions of the drive by applying residual analysis [13], [14]. Extended-kalman filters (EKFs) have also been used to detect ITSCs under non-stationary conditions [15].

Regarding m-PMSMs, most fault detection methods available in the literature are focused on open-phase faults [16]–[18], while others focused on high-resistance connections faults [17], [19] and demagnetisation faults [20]. Albeit the recent developments in ITSC studies [21], [22] and in ITSC fault tolerance [23], [24] for m-PMSMs, the ITSC fault detection has yet to receive the attention it deserves. To the best knowledge of the author, and according to the available literature, very few papers tried to propose a method for the detection of this fault in stationary conditions, let alone non-stationary conditions. In [25] a novel method for the detection of an ITSC was proposed, based on the measurement of the pulse-width modulation (PWM) ripple current. This method used the ripple current generated by the switching inverter as a means to detect the interturn fault in a five-phase PMSM drive. Another PWM based method was developed in [26] which can detect the ITSC in a six-phase fault tolerant PMSM by extracting the PWM harmonic current root mean square (RMS) value. In [27] a method for the ITSC detection was proposed by observing the DC component in the torque deviation for a fault-tolerant five-phase brushless PMSM. In [28] a series of methods were implemented for the detection of the ITSC in a six-phase PMSM, based on the stator currents, stator voltages, zero-sequence voltage component and active/reactive powers. Unfortunately, all these methods require the steady-state operation of the machine.

1.2 Objectives

Given the lack of ITSC fault detection methods in m-PMSMs under non-stationary conditions in the literature, this thesis aims to contribute to the body of knowledge on fault detection techniques available in the literature by developing a technique that is able to detect this types of faults in m-PMSMs under the mentioned dynamic operation. This will help address the current gap in the literature and provide real value to the reliability of multiphase drive systems. Here are the principal objectives set by this thesis:

a) To study the ITSC fault, understanding what causes it and what are its effects on the machine performance.

b) To explore the best signal(s) to analyse as well as ways to extract the fault features

in transient conditions.

c) To develop a fault index, which, based on the extracted features, is sensitive to the ITSC, capable of quantifying the fault extent (fault severity) and to study for the possibility of locating the respective faulty phase.

d) To make computational tests of the developed method(s) for different fault scenarios and operating conditions.

e) To validate experimentally the said method(s) and their effectiveness in detecting the ITSC, through extensive testing, in real-world conditions.

1.3 Thesis Outline

The remainder of this thesis is organised as follows.

In Chapter 2 the different types of faults that can happen in PMSMs are studied and an explanation to what might cause such faults is given. The effect of the interturn short-circuit (ITSC) fault in the machine's parameters are also studied. Furthermore, a review is made on the different ITSC fault detection methods used in the literature. Finally, fault feature extraction techniques are enumerated.

In Chapter 3 two methods were developed to detect and also locate the ITSC. The first method employed the short-time Fourier transform (STFT) to extract the fault feature. Additionally, an algorithm was developed, and coupled with the STFT, to simplify the fault feature frequency tracking. The second method made use of the multiple reference frames (MRF) theory to directly extract the fault features without the need of time-frequency representations.

In Chapter 4 a co-simulation was used to join the modelled machine, in ANSYS/Simplorer ambient, with the control strategy, implemented in MATLAB/Simulink. Several operation modes were simulated and presented, which include a speed variation, a load torque variation, and a combined speed and load torque variation, as well as different numbers of shorted turns and two levels of fault resistance, simulating an incipient and a direct short-circuit, in an effort to evaluate the proposed methods sensitivity to detect the ITSC and quantify its severity.

In Chapter 5, several experimental results were presented, were the machine worked as motor and as a generator, in the same speed/load variations made in Chapter 4, with the intent of validating the proposed methods in a real-world application.

Finally, Chapter 6 summarises the findings, draws conclusions and suggests tasks for a future work.

Chapter 2

Faults and Detection Methods

2.1 Types of Faults

Regarding rotating electric machines [1], and not the entire electric drive, there are three major natures in terms of faults in the system. These natures can be categorised as: mechanical, electrical, and, for the case of PMSMs, magnetic. A categorisation of the most common types of faults is presented in Fig. 2.1.

Removing the focus off the machine itself, the electrical drive would see two extra categories of faults being added. These are the sensor faults and the power electronic converters faults.

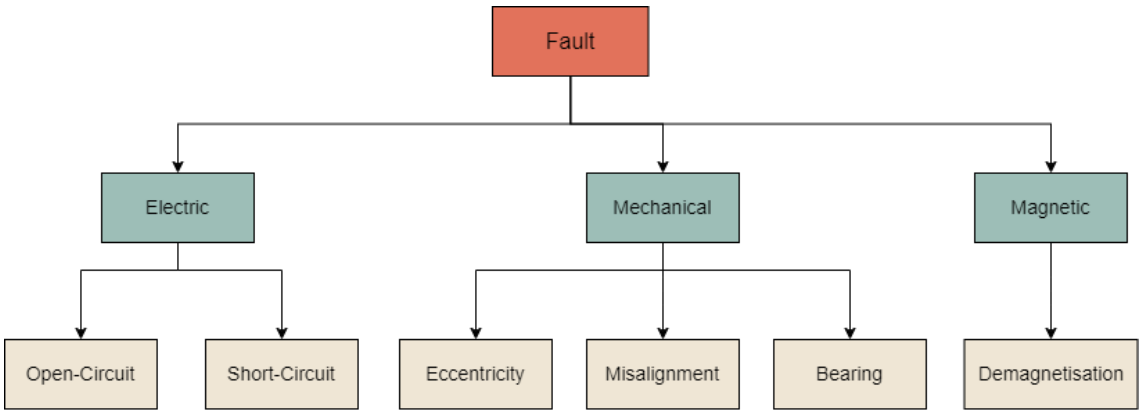

Figure 2.1: Categorisation of PMSM's faults by nature and type.

2.1.1 Mechanical Faults

In terms of mechanical faults, two faults stand out: bearing and eccentricity faults.

Even in normal working conditions, and with a balanced load, the bearing can suffer the so-called fatigue failure, which expresses itself through tiny fissures in the bearing. Over time these fissures spread, eventually causing the breakage of part of the bearing, known as flaking/spalling [29]. There are nonetheless a series of external factors that are responsible for the acceleration of this event such as: contamination, corrosion, improper lubrication and improper installation. The latter can also cause brinelling (indentations in the raceways of the bearings) [30].

The eccentricity defect can be categorised as static eccentricity, dynamic eccentricity and mixed eccentricity [31]. This fault is defined by the asymmetry of the air gap and

[1] Henceforward, when mentioning electric machines the author is referring to rotating electric machines, thus discarding transformers from this work.

is mostly connected to other types of faults (such as bearing faults). This defect can be caused by a bad positioning of the bearing during assembly, by degraded bearings, a curved rotor shaft, or operation at critical speeds. If this fault is not caused by a bearing fault it can certainly cause one, since the eccentricity creates an unbalanced magnetic pull (UMP) that leads to radial forces in the bearings. This excessive stress can cause the deterioration of the bearing and expose the stator windings to unnecessary vibrations [32].

There are other mechanical faults, although less common, which are mostly manufacturing/assembly defects, such as shaft defects and, for the case of induction motors with a squirrel cage, broken bars.

2.1.2 Electric Faults

A fault of electric nature can be described as either a short-circuit in the stator windings (within or in-between) or an open-phase (open-circuit). An open-circuit occurs when a phase winding breaks or when a power electronic device fails [33]. As for the short-circuit fault, it is simply the creation of an extra path, of lower impedance, which will lead to a high circulating current. This current will generate more heat and subsequently the further deterioration of the adjacent insulation. This type of short-circuit is called an interturn short-circuit (ITSC), and it is believed to be the origin of other, more severe, types of short-circuits like the phase-ground short-circuit or the phase-phase short-circuit [34]–[36]. In Fig. 2.2 different types of short-circuits are showcased.

The occurrence of an ITSC is due to the degradation of the windings insulation which can be originated by one or more of the following:

a) Electrical stress: this type of straining is related to a diverse number of factors such as overcurrents, overload and mainly voltage transients [37], [38]. This transients can originate from the switching operations of the power electronic converters or from the changing operating conditions of the motor/generator which causes overvoltages at the machine terminals and uneven voltage distributions within the machine windings. In turn, these lead to increased thermal and electrical stress on the insulation and further its deterioration. The length of the machine power cables can also increase the electric stress since the inverters produce voltages with very short rise times which get reflected at the motor terminals. In the worse case, the voltage at the motor terminals can be twice the DC bus voltage. In addition, since the windings are a complex inductive/capacitive network, the turns closest to the terminals will experience a higher electrical straining. The voltage transients can also cause a localised electrical discharge (partial discharges) within the insulation. This discharge can cause localised heating, chemical reactions, and the formation of gases, which may lead to the progressive deterioration of the insulation material.

b) Thermal stress: thermal stresses are deeply correlated with electrical stresses since the latter causes the former. Nonetheless, other causes for thermal stresses are the high ambient temperature and the obstruction or the outright malfunctioning of the ventilation/heat dissipation system.

c) Mechanical stress: the electrical machine is always subject to vibrations which further contribute to the insulation deterioration in the form of delamination or cracks, and shortens the machine lifespan. The PMSM is not invulnerable to rotor permanent magnets breakage which can cause pieces of the magnet to damage the stator windings.

d) Environment: the environment where the motor/generator is set and its surroundings can also have a say in the lifespan of its different parts including the windings

insulation. Such environmental agents can be corrosive products, humidity, as well as dust and dirt, to name a few.

e) Ageing: not a single component of a PMSM is invulnerable to ageing and therefore a natural degradation of every part happens with the passage of time. In addition, every extra stress (thermal, electrical...) inflicted to it will shorten its lifespan making the whole electrical machine more susceptible to one of the aforementioned natures of stress.

(a) (b) (c)

Figure 2.2: Different short-circuits in the machine stator [39]: (a) inter-turn short-circuit. (b) phase-to-phase short-circuit. (c) phase-to-ground short-circuit, in the middle of the slot.

2.1.3 Magnetic Faults

In PMSMs the rotor is usually made of rare-earth magnets. These magnets are generally composed of neodymium iron boron (NdFeB) or samarium cobalt (SmCo) [40]. The usage of permanent magnets brings advantages, like the reduction of the copper losses, since we no longer have copper windings in the rotor, greater power density and an easier and simpler structure to maintain [41]. There are, of course, disadvantages: the cost of these materials, the means in which they are explored, the sensitivity to temperature and the possibility of the magnet's demagnetisation, to name a few [41]. The different permanent magnet materials are described by a demagnetisation curve, which is the second quadrant of the hysteresis curve. Fig. 2.3 illustrates the demagnetisation curve of the NdFeB magnets used in the 6-PMSM discussed in this dissertation. This curve can be described by a linear part, and a sharp drop part. When the operating point is pushed below the knee of the curve, into the sharp drop part, the demagnetisation of the magnet occurs and some magnetic flux density is permanently lost.

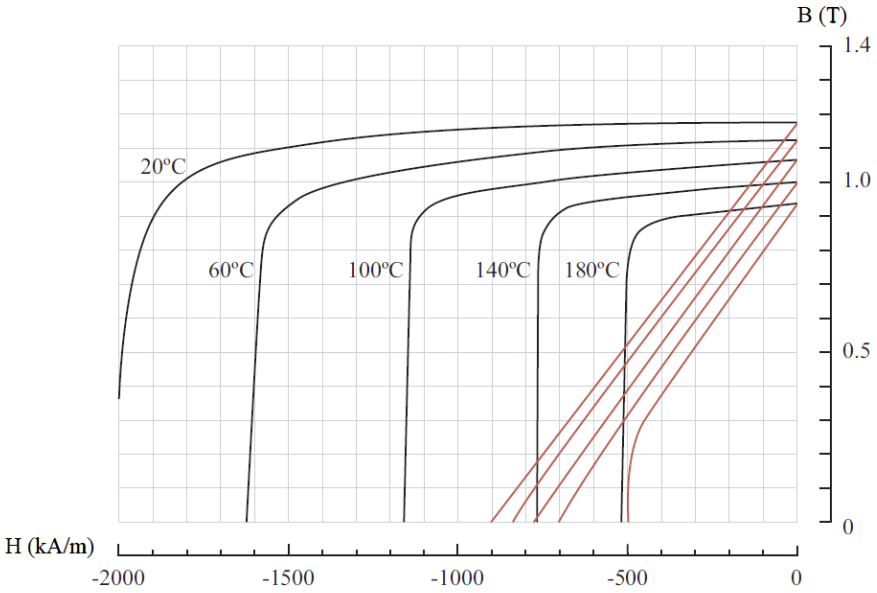

Figure 2.3: Demagnetisation (2nd quadrant of the hysteresis curve) of the neodymium permanent magnets used in the 6-PMSM under study at different operating temperatures [42].

There are two types of demagnetisation: uniform, where all existing PMs in the rotor are demagnetised with the same level and pattern, and partial (local), where it is localised [43].

The demagnetisation disturbs the air gap flux distribution. This disturbance can cause UMP and current harmonics and consequently generate vibration and noise. Additionally, UMP can erode the bearings and even bend the rotor. If part of the magnet breaks, the pieces can also damage the stator windings. The demagnetisation can be caused due to a high starting torque, stator short-circuits and open phases. The temperature of operation facilitates the occurrence of demagnetisation since it will shift the demagnetisation curve, as seen in Fig. 2.3. Stator copper losses, Foucault current losses in the magnet surface and faults in the cooling system are factors which lead to the rise of the operating temperature. The demagnetisation of the magnets leads to a torque drop, which in turn will be compensated by a higher stator current, leading to more copper losses and, as such, a rise in temperature, forming a vicious circle. If the demagnetisation is partial (local), current harmonics are introduced, leading to higher torque ripple which reduces the effectiveness of the control strategy. There are other problems that affect the magnets and can reduce the magnetic flux generated by them, as the oxidation and corrosion of the magnet, the ageing of the magnets, and damages during fabric, which, in high speed, can lead to the disintegration of the magnets [41].

2.2 Fault Effects on Machine Parameter Values

When a short-circuit occurs, a high magnitude current is induced in this newly created path. In such conditions, the magnetomotive force (MMF) created will be uneven. This non-uniform distribution will lead to torque ripple which will affect the machine's performance and cause vibrations, acoustic noise and reduced efficiency. In [4] a thorough investigation of the ITSC effects on a 3-PMSM was made and a summary of the fault features associated with this type of fault was detailed. The principal changes in the machine's characteristics (in an open-loop system) are as follows:

a) Local decrease in the flux density;

b) Local temperature rise due to the high circulating current in the short-circuited path(s);

c) Decrease in both the fundamental and third-harmonic content of the back-electromotive force (Back-EMF);

d) Emergence of a third-harmonic in the stator currents due to an unbalance in the system;

e) Emergence of the fundamental and fifth-harmonic in the potential difference between the source and motor neutral points;

f) Unbalance and increase in the amplitudes of the phase currents.

In regard to the unbalance and increase in the amplitudes of the phase currents, when in a closed-loop system, the control strategy will try and suppress/compensate this unbalance in the phase current, giving rise to the second-harmonic in the dq voltages. There will also be a significant second-harmonic content in the generated torque.

With this investigation, a more thoughtful consideration can be made regarding the choice of signal to be analysed (Fig. 2.4). Electric signals such as currents and voltages are the easiest to analyse as they are already accessible (since the controller needs those signals). Signals like the flux and electromagnetic torque require observers leading to an increased complexity of the system. Other signals, like the temperature or vibrations, require extra equipment which in turn lessens the reliability of the system and heightens its cost.

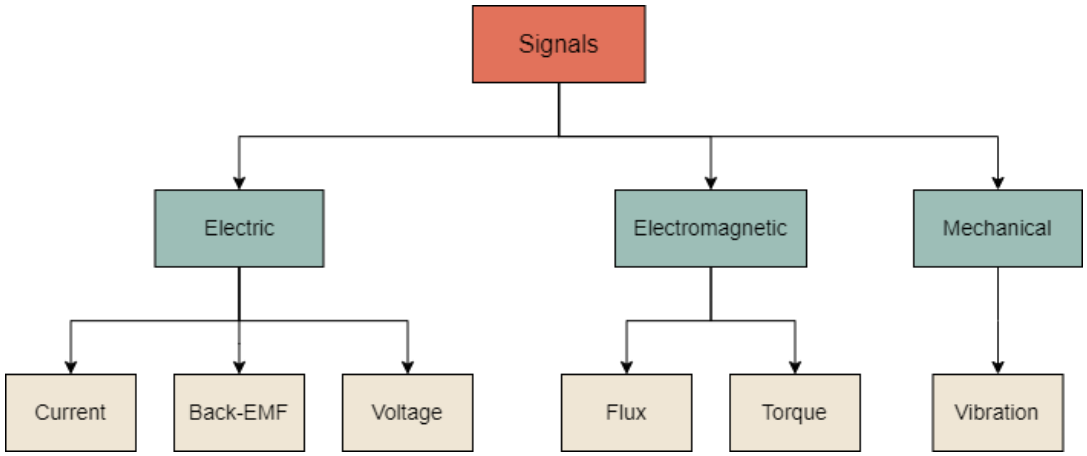

Figure 2.4: Categorisation, by signal nature, of the signals most sensitive to interturn short-circuits.

2.3 Fault Detection Methods

Over the years, a great deal of research has been made to develop methods that detect and diagnose the ITSC [3], [4], [44]. These methods can be generally categorised into three groups: Signal-based techniques, Model-based techniques and Knowledge-based techniques. A categorisation of these groups is presented in Fig. 2.5

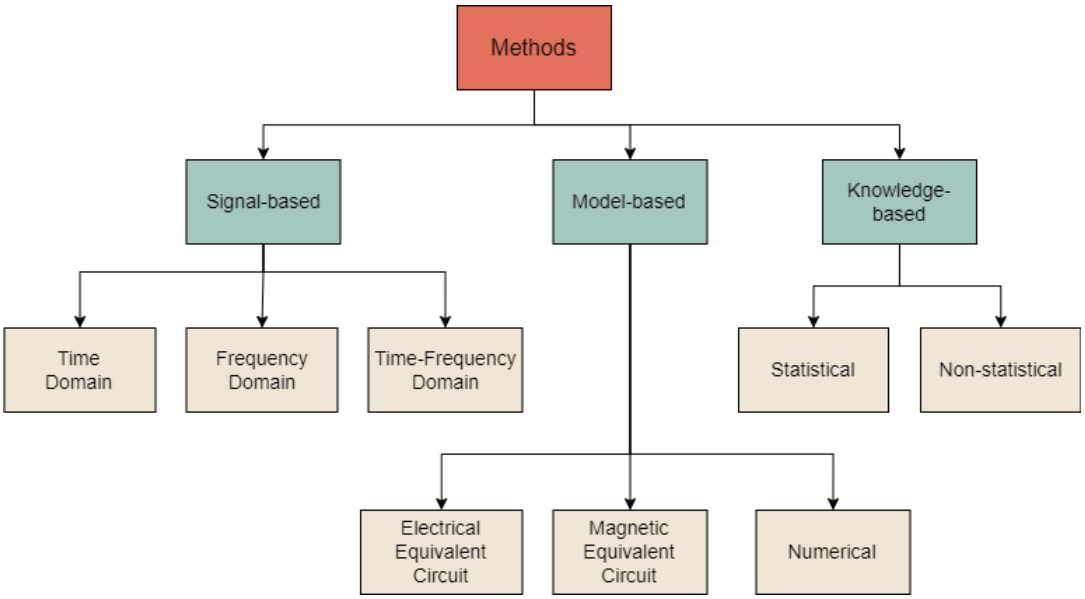

Figure 2.5: Categorisation of fault detection methods.

2.3.1 Signal-Based Methods

Signal-based diagnostic methods consist in the *a priori* knowledge of certain fault characteristic signatures (features) in the system. After measuring (or estimating) the desired signal, and with the help of signal processing techniques, it is possible to extract fault features. By comparing these features with the expected values a decision can be made on whether the machine is running at a normal or abnormal (faulty) condition. The decision making can be made by an expert in the field or by artificial intelligence (AI) tools that are previously trained to recognise these fault feature value discrepancies. Fig. 2.6 shows the fault diagnosis process of signal-based techniques.

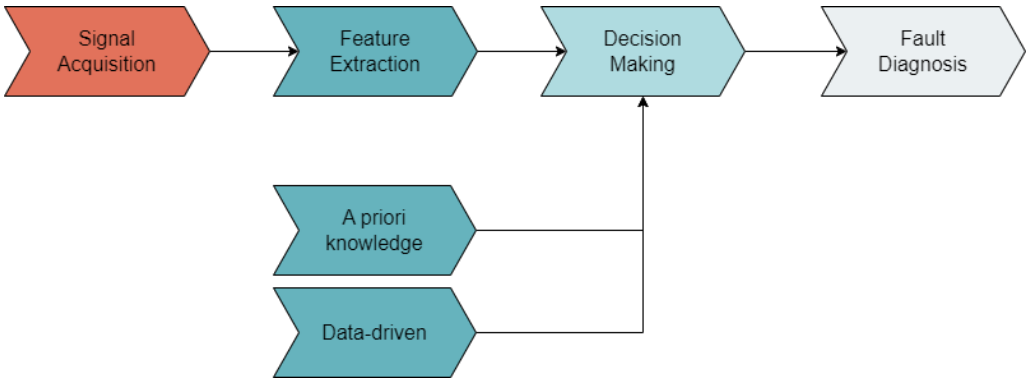

Figure 2.6: Schematic of a typical signal-based fault diagnosis.

Several signal-based diagnostic methods have been proposed in the last decade for application in 3-PMSMs. The most common of these would be the MCSA, which is popular

due to its simplicity and low cost (since the currents are already being measured for the control strategy). The application of this approach consists of monitoring the amplitudes of the characteristic frequency components of the ITSCs.

Following [12], [45]:

$$f_{ss} = f_s\left(1 \pm 6v\right) \tag{2.1}$$

where f_{ss} is the stator slot harmonics, f_s is the supply frequency and v is a consecutive positive integer, along with

$$f_t = f_s\left(1 \pm v\frac{N_{ss}}{p}\right) \tag{2.2}$$

where f_t is the stator teeth harmonics, N_{ss} is the number of stator slots and p is the number of pole pairs, and also,

$$f_{sh} = f_s\left(v_o \pm \frac{n}{p}\right) \tag{2.3}$$

where f_{sh} is the space harmonics, $n = 1, 2..., (2p-1)$ and $v_o = 1, 3$, it is possible to find the harmonics which are increased by the ITSC.

Nonetheless, and as stated before, these frequency components (in close-loop drives) are mainly the third-harmonic in the stator currents and the second-harmonic in the *dq*-axis currents. The impact of ITSCs on the amplitude of the $3f_s$ component in a wide range of 3-PMSMs modes of operation has already been investigated in the literature. However, the 3rd harmonic also increases in the presence of rotor eccentricity. In [46] a way to discern the ITSC from the rotor eccentricity when analysing this fault component was developed, by monitoring the 17th and 19th harmonious values, as well as sideband frequencies.

To improve the effectiveness of the ITSC fault detection compared to the classical spectral analysis of the stator phase current the calculation of the stator current Park's vector was envisioned. Under normal conditions, the current Park's vector will have a circular representation and the modulus will be constant. However, under abnormal conditions, the modulus will contain a dominant dc level and an ac level, whose existence is directly related to the asymmetries either in the motor or in the voltage supply system. In order to discriminate the information contained in the modulus of the current Park's Vector the spectral analysis of the ac component of this modulus is made. The ITSC manifests itself by the presence of a spectral component at twice the fundamental supply frequency ($2f_s$). This method is known as extended Park's vector approach (EPVA), and its effectiveness in the ITSC detection has been confirmed in [47] and [48] for a PMSM.

It is well known that symmetrical components are used to study machines under unbalanced conditions. This unbalanced conditions can be caused by phase imbalances, asymmetrical loads or faults. By decomposing the unbalanced system into positive sequence, negative sequence, and zero sequence the analysis becomes simpler. In [49] the negative sequence $3f_s$ component and f_s component of the stator currents were used to detect the ITSC. In [50] the negative sequence component of the fundamental frequency is used to detect the ITSC in a 3-PMSM where load fluctuations might occur.

The 3-PMSM stator currents can be transformed into the direct-quadrature axis and then the space vector, $\underline{i}_s = i_d + ji_q$, can be obtained where the FFT will allow for the retrieval of the negative and positive sequence components.

Negative sequence components of the stator currents were also used in [28] to detect the ITSC in a 6-PMSM.

Unfortunately all of the methods above require non-stationary operating conditions. Time-frequency representations have been used as a means to detect the ITSC when the machine works under dynamic conditions such as variable speed or variable load torque.

A common time-frequency tool is the wavelet transform (WT). In [51] the continuous wavelet transform (CWT) is applied to the stator currents and the residual signal is used as the fault index. Wavelet packets have also been used to detect the ITSC in transient conditions where the stator current signal was decomposed and then the signal energy of each frequency band (regarded as eigenvectors) were used to build a normalised energy eigenvector as the fault index [52]. In [7] both discrete wavelet transform (DWT) and CWT were used in the stator currents, were it was proven that the lower details are sensitive to the ITSC, making their variation a possible fault feature. In [53] the Hilbert-Huang transform (HHT) is used, which is based on the empirical mode decomposition (EMD) and the Hilbert transform (HT), to detect the ITSC by analysing the third-harmonic component. In [45] the HHT is used to analyse the energy variation of the current signal. In [54] the LSPMSM current signals are analysed with a Gabor-Order Tracking technique as a way to only analyse fault-related harmonic component of the signal instead of analysing a whole spectrum band. To detect the severity of the fault the signal is decomposed with the ensemble empirical mode decomposition (EEMD).

Nevertheless, due to the control strategy efforts to suppress/compensate unbalances in the stator currents, the amplitude of the characteristic frequency components in this signal will be diminished. In fact, in the predictive current control strategy, which is used in this work, this effect is even more pronounced due to a larger bandwith when compared to other control strategies like the field oriented control (FOC) and direct torque control (DTC).

Considering that the control strategy also requires the stator voltages, and that the usage of the voltage signal as a fault index allows for the fault analysis under no-load conditions, this signal immediately becomes a prime choice for the ITSC fault detection.

As stated in the fault effects section, one of the consequences the ITSC provokes is the emergence of the fundamental and fifth-frequency components in the potential difference between the source and motor neutral points, making it so that the zero-sequence voltage components (ZSVC) can also be used in the short-circuit diagnosis [8], [55], [56]. An approximate expression of the ZSVC of a 3-PMSM is,

$$u^0 = \frac{1}{3}\mu R_s i_f + \frac{1}{3}\mu(L+2M)\frac{di_f}{dt} - \frac{d\Psi^0_{PM}}{dt} \tag{2.4}$$

where μ is the ratio between the number of short-circuited turns and the total number of turns in a certain phase. R_s is the resistance of the stator phase winding, L and M are the self-inductance and mutual-inductance in one phase, respectively, and $\Psi_{PM,0}$ is the zero sequence no-load flux linkage.

In a healthy PMSM, the fault current i_f, is null, making u^0 only dependent on the time derivative of Ψ^0_{PM}. Only the 3rd and its odd multiples exist in the zero-sequence flux and so the ZSVC will have the same harmonics. In a faulty PMSM however, u^0 will depend on the fault current, i_f which has the fundamental and odd harmonics. Therefore, the new added components (fundamental, fifth and seventh) might be used for the detection of the ITSC.

In [28] the ZSVC was used for the interturn short-circuit fault detection in a six-phase PMSM, in steady-state conditions, making use of the neutral points from the first and second set of windings.

Evidently, the application of the ZSVC as a fault diagnosis method implies that the neutral point of the machine is available. Consequently, the PMSM must be wye-connected and an additional voltage sensor is required for the measurement of the voltage between the source and the neutral point.

Boileau et al. [57] decompose the 2nd harmonic component of the control voltages into its positive and negative sequences. It was concluded that the positive sequence depends primarily on the fault and the negative sequence is mainly related to the back-EMF 3rd

harmonic. The positive sequence is then extracted from the control voltages, in the dq-frame, through a rotation matrix as well as two low-pass filters (LPF). The fault indicator is then compared to a prerecorded threshold which corresponds to its value for the healthy machine. Likewise, in [58], the amplitude of the 2nd harmonic component of the stator voltages is also used as a fault index for the ITSC severity.

Meinguet et al. [59] propose a diagnostic method derived from the positive and negative sequences of the voltage references. These symmetrical components are extracted with adaptive filters and the ratio between the magnitudes of the negative and positive sequence voltages is used as a fault index. Although in theory the index should be equal to zero in healthy operation, it is never zero due to a residual (asymmetry) value that depends on the operating conditions and as such must be taken into account. The use of the adaptive filters instead of the FFT allows for the detection under non-stationary operating conditions. Nonetheless, the authors point out that due to the filter dynamics the fault detection should be inhibited below a minimum speed.

The back-EMF can also be analysed to extract ITSC fault features. In [60] the back-EMF is estimated through an extended state observer (ESO). To get the 3rd harmonic component of the back-EMF from the observed e_d and e_q the inverse park transform is applied, resulting in the negative sequence component $e^{-}_{\alpha\beta}$. To extract this component a second-order generalised integrator is used which behaves essentially like a notch filter. After the positive sequence has been separated from the negative sequence, the square of the amplitudes of the negative sequence components is used as the fault index. The usage of disturbance observers such as the ESO, although fairly simpler than the mathematical models needed for a residual approach, are still very complex when compared to a simple estimator.

2.3.2 Model-Based Methods

The principle of model-based methods is no different from the signal-based ones: comparing a real value with a reference value. In this case, the reference value is not known *a priori*. Instead, a reference mathematical model of the machine, in healthy conditions, is created, leading to a comparison between the actual output and the expected output, and consequently the evaluation of the normal or abnormal condition state. The difference between these values (actual/real vs expected/reference) is called a residual. Afterwards, a simple threshold can be made to define the condition state of the machine, removing the need for the knowledge of the expert to evaluate the fault feature magnitude. Fig. 2.7 shows the overall fault diagnosis process of model-based techniques.

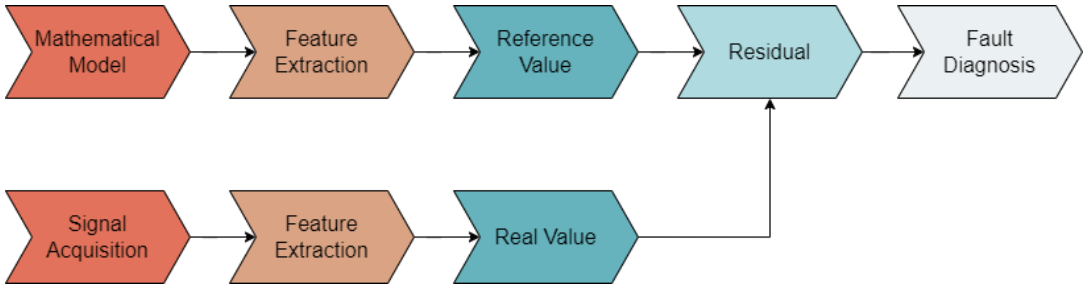

Figure 2.7: Schematic of a typical model-based fault diagnosis.

An important aspect of model-based methods is that they require the knowledge of machine parameters. Model uncertainties, parameter variations, or manufacturing imprecision of the PMSM are the main disadvantages that should be considered when analysing the robustness and reliability of model-based methods. These methods also require knowing the back-EMF for the online application [14].

Most model-based techniques use residual analysis as a fault detection. In some cases, a comparison is made between the reference back-EMF and the back-EMF estimated by state observers. In [13] the back-EMF signal is chosen as the signal for the ITSC fault detection with the decision-making technique being a threshold-based one. The fault index is the average differences between the real time estimated back-EMF and the reference back-EMF. The reference back-EMF is estimated from the healthy machine, bypassing uncertainties that are not accounted for in the design of an estimator. The reference back-EMF is collected in lookup tables which are controlled by speed and rotor position. The real-time back-EMF estimation is made through a model based on finite elements and includes the thermal behaviour of the machine. According to the authors, the switching frequency of the inverter, the dead-time of the upper and lower semiconductor switches in the inverter, the semiconductor switches voltage drops, the offset of the current transducer, the calibration of the thermal sensor and encoder are of the factors that affects the estimated back-EMF. It can be concluded that this back-emf estimation heavily relies on mathematical modelling, including the thermal modelling of the machine, making it a very complex fault detection method, which highly depends on accurate parameters.

Other methods detect the stator fault by comparing the measured currents with the estimated ones. Mazzoletti et al. [14] perform the ITSC fault detection with a residual current vector generated by the difference between the stator currents measurement and the stator currents estimated by using a state observer. However, the resulting residual current vector signal could be produced by other disturbances such as model parameter uncertainties, asymmetric currents, measurement noise, among others. Therefore the effects of undesired perturbations are decoupled through the sequence decomposition of the residual current vector by employing the reference-frame theory. The resulting residual current vector signal in the stationary reference frame is referred to the positive sequence synchronously rotating reference frame. In this new reference frame, the positive sequence component must be a constant signal and the negative sequence component will be an alternating signal. The same process is performed to obtain the negative sequence component by referring the residual current vector signal to the negative sequence synchronously rotating reference frame. Afterwards the resulting signals are filtered through a LPF for separating each of the sequence components.

It is concluded that the negative sequence of the residual current vector can be used to detect an ITSC. In order to locate the stator winding fault the difference between the relative positions of the sequence reference frames is calculated.

2.3.3 Knowledge-Based Methods

Knowledge-based methods, also known as data-driven methods, are different from signal-based and model-based approaches, as they can only start from where a large volume of historic data is available. The consistency between the real-time system and the knowledge base is then checked, leading to a fault diagnosis decision with the aid of a classifier. A schematic of a typical knowledge-based fault diagnosis is illustrated in Fig. 2.8.

The extraction process of the knowledge base can be either qualitative or quantitative in nature [61]. With regard to fault detection methods, the vast majority of knowledge-based techniques fall under the quantitative nature.

A quantitative knowledge-based method formulates the diagnostic problem solving as a pattern recognition problem. Quantitative information (or features) can be extracted by using either statistical or non-statistical methods [61]. Under a statistical framework, the quantitative knowledge-based fault diagnosis methods are mainly composed of principal component analysis, partial least squares, independent component analysis, statistical pattern classifiers, and support vector machine [62]. Owing to its powerful ability in non-linear

approximation and adaptive learning, neural networks have been the most well-established non-statistical-based data-driven fault diagnosis tool. Another approach is the Fuzzy logic which partitions a feature space into fuzzy sets and utilises fuzzy rules for reasoning, which essentially provide approximate human reasoning [50].

The usage of the above-mentioned methods can minimise human participation in fault diagnosis and help in automating the decision-making process.

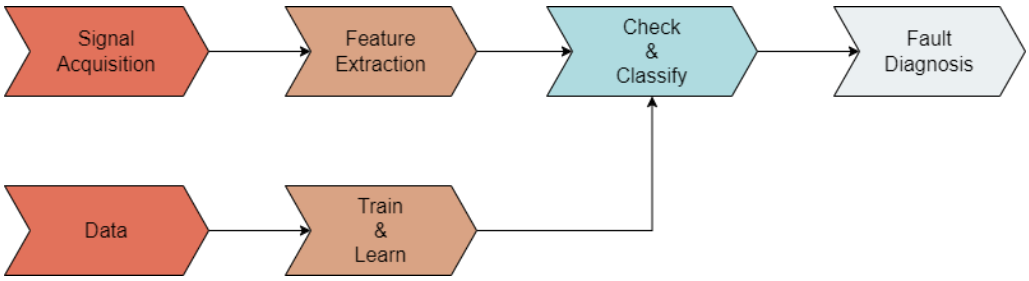

Figure 2.8: Schematic of a typical knowledge-based fault diagnosis process.

2.4 Fault Feature Extraction

As stated earlier, the most commonly used tool for spectral analysis in the fault diagnosis of electric machines is the FFT. The FFT is an algorithm that computes the Discrete Fourier Transform (DFT), which in turn is a transform that allows to see the spectral content of a given signal, therefore giving access to the frequency domain representation of that signal. The DFT is given by

$$X_k = \sum_{n=0}^{N-1} x_n e^{-\frac{j2\pi}{N}kn}, \tag{2.5}$$

while its inverse – the Inverse Discrete Fourier Transform – is:

$$x_n = \frac{1}{N} \sum_{n=0}^{N-1} X_k e^{\frac{j2\pi}{N}kn}. \tag{2.6}$$

In 1965, James Cooley and John Turkey publish "*An Algorithm for the Machine Calculation of Complex Fourier Series*", introducing the FFT as an algorithm that requires only $N \log N$ operations, while the computation of the DFT required N^2 operations [63]. This algorithm was revolutionary given that it considerably reduced computational time (specially in big time series) and, to this day, is massively used in various applications.

Although this algorithm is extensively used in signal processing, it is inadequate for fault detection in most 6-PMSM applications, as these involve variations in speed (which implies frequency variation) over time. Since the FFT is a technique bounded to the frequency domain, the simple usage of the FFT will fail when it comes to the analysis of non-stationary signals. Hence, to extract fault related features in non-stationary conditions, the FFT can no longer be used, giving place to time-frequency analyses techniques.

2.4.1 Time-Frequency Representations: Linear

Short-Time Fourier Transform

Dennis Gabor, interested in representing a signal in the time-frequency domain, was the first to modify the Fourier Transform by introducing a window function capable of providing a location in time, creating the Gabor transform, in 1946, defined as [64]:

$$Gabor(t, f) = \int_{-\infty}^{\infty} x(t)e^{-\pi(t-\tau)^2}e^{-2\pi ft}d\tau \ . \tag{2.7}$$

The Gabor transform is nothing more than a Short-Time Fourier Transform (STFT) with a gaussian window. Generalising the Gabor transform for any window function one obtains the STFT:

$$STFT(t, f) = \int_{-\infty}^{\infty} x(t)h(t-\tau)e^{-2\pi ft}d\tau \ , \tag{2.8}$$

where $x(t)$ is the signal to be analysed and $h(t-\tau)$ is the time window function.

The STFT determines the frequency components in parts of the signal, while it varies in time, dividing it in small windows of equal size and then applying the Fourier transform separately to each part. However, the STFT is not flexible since the window function must be chosen prior to the analysis and can not be changed after being selected. The window to be chosen is not something known a priori and fixing it implies that it is only possible to deal with a very limited speed/load variation. As a matter of fact, since the windows are all of the same size, the resolution will be the same for every window, which may imply not capturing an event of very short duration or distinct durations.

Ideally, a good resolution in both time and frequency is desired, but, as stated by Heisenberg's principle of uncertainty, time resolution can not be increased at the same time as frequency resolution, and vice-versa, so a trade-off must be targeted.

Wavelet Transform

Contrary to the STFT, the Wavelet Transform (WT) provides a frequency resolution that varies over time, allowing a better time resolution at higher frequencies and better frequency resolution at lower frequencies. In Fig. 2.9 a comparison between the type of windowing done by the STFT and the WT is made.

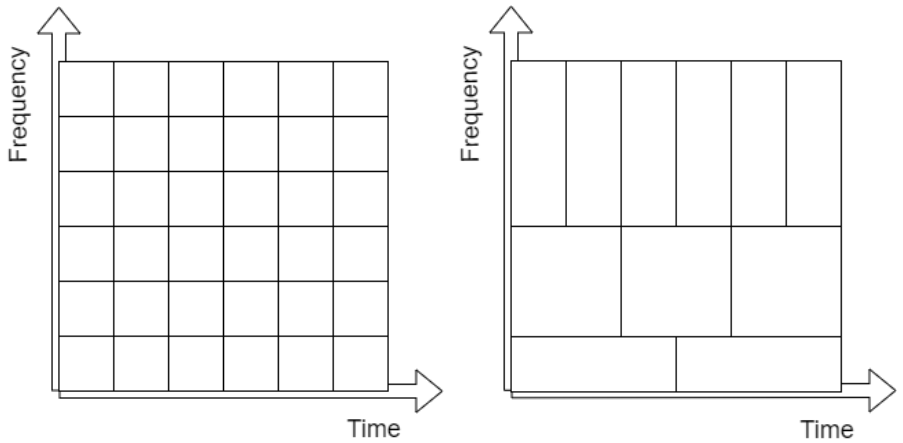

(a) (b)

Figure 2.9: Comparison of the different window fragmentations done by the: a) STFT; b) WT

Although this method is commonly referred as a time-frequency domain method, in reality, it is a time-scale (or space-scale) domain method, which can be used for the analysis of non-stationary signals. Wavelets were envisioned in the late 70's by Jean Morlet. Morlet had the idea of using different size windows to analyse different frequency bands, something that was not possible at the time with the use of the STFT. Due to its small nature and

oscillatory windows, Morlet named them "wavelets of constant shape". A wavelet is a function scaled and translated from the basis function —the mother wavelet—,

$$\psi_{(a,b)}(t) = \frac{1}{\sqrt{a}}\psi\left(\frac{t-b}{a}\right) , \tag{2.9}$$

where $\psi_{(a,b)}$ is a family of wavelets, ψ is a wavelet mother and a and b are the scaling and translation factors, respectively.

Later the continuous wavelet transform (CWT) was formalised [65]:

$$CWT(a,b) = \frac{1}{\sqrt{a}}\int x(t)\overline{\psi}\left(\frac{t-b}{a}\right)dt . \tag{2.10}$$

One disadvantage with the CWT is the amount of data it generates, which, depending on the application, might be greatly redundant. Thus, creating the need for an orthogonal decomposition.

Based on the idea of the iterative application of low-pass and high-pass filters to a signal, followed by a down sampling by two, the discrete wavelet transform (DWT) was devised, being defined as

$$DWT(l,k) = s_0^{-\frac{l}{2}}\int_{-\infty}^{\infty} x(t)\psi\left(s_0^{-\frac{l}{2}}t - k\tau_0\right)dt , \tag{2.11}$$

where τ_0 and s_0 are positive constants usually taken to be 1 and 2 respectively. The integer l describes the different levels of resolution and k covers the number of locations in time at each level.

The DWT is more efficient computationally wise than the CWT, since the DWT does not use the signal itself, but only its parameters, and does not generate a huge amount of data. Although, depending on the application, the use of the CWT might mean a more precise analysis when compared to the DWT. The use of the wavelet transforms altogether (be it CWT or DWT) implies some practical problems such as the selection of the mother wavelet, the tuning of the parameters and the lack of phase information.

Hilbert-Huang Transform

Norden E. Huang *et al.* [66] proposed in 1998 an algorithm called Empirical Mode Decomposition (EMD) together with the use of the Hilbert Transform (HT) to analyse non-linear and non-stationary signals. Later this analysis was baptised as the Hilbert-Huang Transform (HHT). The EMD algorithm decomposes the signal in various Intrinsic Mode Functions (IMFs), where each IMF is a mono-component function. The HT is then applied to each IMF. The HT of a given signal, x(t), was created by David Hilbert, and is defined as:

$$H[x(t)] = \frac{1}{\pi}\int\frac{x(\tau)}{t-\tau}d\tau = x(t) * \frac{1}{\pi\tau} , \tag{2.12}$$

where * denotes convolution.

2.4.2 Time-Frequency Representations: Bi-linear (Quadratic)

Wigner-Ville Distribution

The Wigner-Ville distribution (WV) was firstly introduced by Eugene Wigner in 1932, simply as the Wigner Distribution, being reinvented in 1947 by Jean Ville, when he derived it in search for the energy spectrum of a signal in the time-frequency domain. Given a signal in time, $x(t)$, the WV is defined by

$$WV(t,f) = \frac{1}{2\pi}\int_{\infty}^{\infty} x\left(t+\frac{\tau}{2}\right)\overline{x}\left(t-\frac{\tau}{2}\right)e^{-j2\pi f\tau}d\tau\ , \tag{2.13}$$

where $\overline{x}(t)$ is the complex conjugate of $x(t)$.

The Wigner-Ville distribution belongs to Cohen's Class Distributions. The general form of this quadratic (bi-linear) distributions in the time-frequency domain can be defined by:

$$Cohen(t,f;\Phi) = \frac{1}{4\pi^2}\iiint e^{j(\gamma s-\tau 2\pi f-\gamma t)}\Phi(\gamma,\tau)x\left(s+\frac{\tau}{2}\right)\overline{x}\left(s-\frac{\tau}{2}\right)ds\tau\gamma\ , \tag{2.14}$$

where $\Phi(\gamma,\tau)$ is the arbitrary function named kernel while γ and τ are the running frequency and the time variable of the integration, respectively.

Giving different values to the kernel, one can obtain different distributions. The Wigner-Ville Distribution is obtained by $\Phi(\gamma,\tau) = 1$, which offers high time-frequency resolution. The disadvantage of the WV is that if the signal to be analysed has more than one frequency component, this is, if the signal is multi-component, due to is quadratic nature, there will appear cross-terms [2]. These cross-terms consist in the superposition of certain signal amplitudes, resulting in higher difficulty to interpret the results, as it becomes hard to distinguish between cross-terms and important fault signatures. One solution to remove cross-terms (with loss of resolution) is through the windowed version of the WV, named Pseudo-Wigner-Ville Distribution (PWV):

$$PWV(t,f) = \frac{1}{2\pi}\int_{\infty}^{\infty} h(\tau)x\left(t+\frac{\tau}{2}\right)\overline{x}\left(t-\frac{\tau}{2}\right)e^{-j2\pi f\tau}d\tau\ , \tag{2.15}$$

where h(t), the time smoothing window, is a real and symmetrical function.

The time window effect is to reduce the cross-terms present in the original WVD, reducing the resolution, but still giving a better performance comparatively to linear distributions such as the STFT. The smoothing of both time and frequency came afterwards, with the Smoothed Pseudo-Wigner-Ville Distribution (SPWV):

$$SPWV(t,f) = \frac{1}{2\pi}\int_{\infty}^{\infty} h(\tau)\int_{\infty}^{\infty} g(s-t)x\left(s+\frac{\tau}{2}\right)\overline{x}\left(s-\frac{\tau}{2}\right)e^{-j2\pi f\tau}d\tau\ . \tag{2.16}$$

Choi-Williams Distribution

With the purpose of eliminating the interference of cross-terms, Hyung-Ill Choi e William J. Williams introduced, in 1989, the exponential kernel,

$$\Phi(\gamma,\tau) = e^{-\frac{-\gamma^2\tau^2}{\sigma}}\ . \tag{2.17}$$

Thus creating the Exponential Distribution [67], also part of Cohen's Class of Distributions. Indeed, the number of interferences and their magnitude are directly related to the kernel function. This distribution was later baptised as the Choi-Williams Distribution, being defined as:

$$CW(t,f) = \frac{1}{4\pi^{\frac{3}{2}}}\iint\sqrt{\frac{\sigma}{\tau^2}}e^{-\frac{\sigma(\mu-t)^2}{4\tau^2}-j2\pi f\tau}x\left(\mu+\frac{\tau}{2}\right)\overline{x}\left(\mu-\frac{\tau}{2}\right)d\mu d\tau\ , \tag{2.18}$$

where the parameter σ controls the cross terms suppression and the frequency resolution.

When σ is small, the Choi-Williams resembles the Wigner-Ville. Increasing σ the interferences are attenuated, but the resolution diminishes.

[2] Also known as artifacts

Zhao-Atlas-Marks Distribution

Yunxin Zhao, Les Atlas and Robert Marks proposed in 1990 a kernel function with a cone shape, introducing a finite time support and reducing the cross-terms, resulting in the Zhao-Atlas-Marks Distribution (ZAM). The kernel expression is,

$$\Phi(\gamma,\tau) = \frac{sin\left(\frac{\gamma|\tau|}{a}\right)}{\frac{\gamma}{2}} , \tag{2.19}$$

$$\Phi(\gamma,\tau) = h(\tau)|\tau|\frac{sin(a\gamma\tau)}{a\gamma\tau} , \tag{2.20}$$

where a is a parameter bigger than or equal to two.

The ZAM distribution is defined as [68]:

$$ZAM(t,f) = \frac{1}{4\pi a}\int h(\tau)e^{-j2\pi f\tau}\int_{t-a\tau}^{t+a\tau} x\left(s+\frac{\tau}{2}\right)\overline{x}\left(s-\frac{\tau}{2}\right)dsd\tau . \tag{2.21}$$

Chapter 3

Interturn Short-Circuit Fault Detection

3.1 Six-Phase PMSM Mathematical Model

The dynamic model of the 6-PMSM under analysis in the natural frame (phase coordinates) is given by [42]:

$$u_s^{abc} = R_s i_s^{abc} + L_s^{abc} \frac{di_s^{abc}}{dt} + e_s^{abc} \ , \tag{3.1}$$

$$e_s^{abc} = \frac{d\Psi_{s,PM}^{abc}}{dt} \ , \tag{3.2}$$

$$\Psi_s^{abc} = Ls^{abc} i_s^{abc} + \Psi_{s,PM}^{abc} \ , \tag{3.3}$$

where the index s denotes a quantity relative to the stator. R_s is the stator resistance, L_s^{abc} is the inductance matrix and u_s^{abc}, i_s^{abc}, Ψ_s^{abc}, Ψ_{PM}^{abc}, e_s^{abc} are the vectors of the stator voltages, stator currents, flux linkage, no-load flux linkage and back-EMF respectively.

The inductance matrix L_s^{abc} is given by [69]:

$$L_s^{abc} = \begin{bmatrix} L_s & M_s & M_s & M_1 & -M_1 & 0 \\ M_s & L_s & M_s & 0 & M_1 & -M_1 \\ M_s & M_s & L_s & -M_1 & 0 & M_1 \\ M_1 & 0 & -M_1 & L_s & M_s & M_s \\ -M_1 & M_1 & 0 & M_s & L_s & M_s \\ 0 & -M_1 & M_1 & M_s & M_s & L_s \end{bmatrix} \tag{3.4}$$

where M_s is the mutual inductance between phases within the same set of three-phase windings (3.5), and $M_1, -M_1, 0$ are the mutual inductance between the phases belonging to different sets of three-phase windings (3.6).

$$\begin{aligned} M_s = M_{a1b1} = M_{a1c1} = M_{b1a1} = M_{b1c1} = M_{c1a1} = M_{c1b1} \\ = M_{a2b2} = M_{a2c2} = M_{b2a2} = M_{b2c2} = M_{c2a2} = M_{c2b2} \end{aligned} \tag{3.5}$$

$$\begin{aligned} M_1 &= M_{a1a2} = M_{b1b2} = M_{c1c2} = M_{a2a1} = M_{b2b1} = M_{c2c1} \ , \\ M_2 &= M_{a1b2} = M_{b1c2} = M_{c1a2} = M_{b2a1} = M_{c2b1} = M_{a2c1} = -M_1 \ , \\ M_3 &= M_{a1c2} = M_{b1a2} = M_{c1b2} = M_{c2a1} = M_{a2b1} = M_{b2c1} = 0 \end{aligned} \tag{3.6}$$

A vector space decomposition (VSD) transformation was proposed in [70] enabling the possibility of modelling a six-phase machine into three orthogonal subspaces: $\alpha\beta$, xy and $z1z2$. The VSD for six-phase asymmetrical machines is given by [69]:

$$T_{vsd} = \frac{1}{3}\begin{bmatrix} 1 & -\frac{1}{2} & -\frac{1}{2} & \frac{\sqrt{3}}{2} & -\frac{\sqrt{3}}{2} & 0 \\ 0 & \frac{\sqrt{3}}{2} & -\frac{\sqrt{3}}{2} & \frac{1}{2} & \frac{1}{2} & -1 \\ 1 & -\frac{1}{2} & -\frac{1}{2} & -\frac{\sqrt{3}}{2} & \frac{\sqrt{3}}{2} & 0 \\ 0 & -\frac{\sqrt{3}}{2} & \frac{\sqrt{3}}{2} & \frac{1}{2} & \frac{1}{2} & -1 \\ 1 & 1 & 1 & 0 & 0 & 0 \\ 0 & 0 & 0 & 1 & 1 & 1 \end{bmatrix} \tag{3.7}$$

In order to to transform the variables from the stationary reference frame into the rotor reference frame a rotation matrix is adopted [42]:

$$R = \begin{bmatrix} cos(\theta) & sin(\theta) & 0 & 0 & 0 & 0 \\ -sin(\theta) & cos(\theta) & 0 & 0 & 0 & 0 \\ 0 & 0 & cos(\theta) & -sin(\theta) & 0 & 0 \\ 0 & 0 & sin(\theta) & cos(\theta) & 0 & 0 \\ 0 & 0 & 0 & 0 & 1 & 0 \\ 0 & 0 & 0 & 0 & 0 & 1 \end{bmatrix} \tag{3.8}$$

The mathematical model of an asymmetrical 6-PMSM, obtained by the application of the VSD transformation along with the rotation matrix to the PMSM model in the natural frame is [42]:

$$u_s = R_s i_s + L_s \frac{di_s}{dt} + \omega_r J L_s i_s + e_s \ , \tag{3.9}$$

$$e_s = \omega_r J \Psi_{s,PM} + \frac{d\Psi_{s,PM}}{dt} \ , \tag{3.10}$$

$$\Psi_s = L_s i_s + \Psi_{s,PM} \ , \tag{3.11}$$

The stator inductance matrix L_s is then given by:

$$L_s = (R\,T_{vsd}) L_s^{abc} (R\,T_{vsd})^{-}1 \begin{bmatrix} L_s & M_s & M_s & M_1 & -M_1 & 0 \\ M_s & L_s & M_s & 0 & M_1 & -M_1 \\ M_s & M_s & L_s & -M_1 & 0 & M_1 \\ M_1 & 0 & -M_1 & L_s & M_s & M_s \\ -M_1 & M_1 & 0 & M_s & L_s & M_s \\ 0 & -M_1 & M_1 & M_s & M_s & L_s \end{bmatrix} \tag{3.12}$$

The matrix J is given by:

$$J = \frac{1}{\omega_r}(R\,T_{vsd})\frac{d(R\,T_{vsd})^{-}1}{dt} = \begin{bmatrix} 0 & -1 & 0 & 0 & 0 & 0 \\ 1 & 0 & 0 & 0 & 0 & 0 \\ 0 & 0 & 0 & 1 & 0 & 0 \\ 0 & 0 & -1 & 0 & 0 & 0 \\ 0 & 0 & 0 & 0 & 0 & 0 \\ 0 & 0 & 0 & 0 & 0 & 0 \end{bmatrix} \tag{3.13}$$

3.2 Signal Analysis

The choice of signal is of great importance in order to achieve a reliable and sensitive fault detection method. As previously mentioned, there are a couple of signals which are readily available due to the existence of the controller: the stator current and the stator voltage. The use of these signals does not increase drive costs, or system complexity, but, as explained in the ITSC fault effects on the machine parameter values, and in the

summary of fault detection methods, the stator current fault features are lessened in a closed-loop operation due to the compensations made by the control strategy. This leaves the stator voltage as the best overall signal to analyse. There is, however, an interest in determining how sensitive the back-EMF signal is to the ITSC and whether this signal is more independent of the operating conditions of the machine when compared to the stator voltages.

For that, the back-EMF needs to be estimated. As to not considerably increase the complexity of the system, a simplification is made in the stationary reference frame to 3.9 as follows:

$$u_s^{\alpha\beta} = R_s i_s^{\alpha\beta} + L_s \frac{di_s^{\alpha\beta}}{dt} + e_s^{\alpha\beta} \tag{3.14}$$

By rewriting this equation (3.14), the back-EMF can be estimated as:

$$e_s^{\alpha\beta} = u_s^{\alpha\beta} - R_s i_s^{\alpha\beta} - L_s \frac{di_s^{\alpha\beta}}{dt} \tag{3.15}$$

Having measured the stator voltages and estimated the back-EMF, a fault feature extraction technique can be applied to each signal in order to obtain their symmetrical components. As mentioned in Chapter 2 the amplitude of the 2nd harmonic component of $\underline{u}_{\alpha\beta}$ (and $\underline{e}_{\alpha\beta}$) can be used as an ITSC fault severity indicator. The decomposition of these vectors into their positive and negative sequences makes the negative sequence fundamental frequency component the most sensitive to the ITSC. To improve on this fault index, similarly to the Meinguet et al. method, the fault severity will be defined as:

$$FS = \frac{|\underline{x}^-_{\alpha\beta,f} - \underline{x}^-_{\alpha\beta,h}|}{|x^+_{\alpha\beta,f}|} \tag{3.16}$$

where x represents the desired signal ($u_{\alpha\beta}$ or $e_{\alpha\beta}$), and index f denotes the faulty condition while index h is for the healthy condition. From 3.16 it can be noticed the inclusion of a second term in the numerator. This is to make the fault severity more reliable since even in healthy conditions the negative sequence component at the fundamental frequency will be present, to a greater or lesser extent. This can be due to an unbalance in the voltage system that feeds the machine, the presence of a residual asymmetry or even a difference in the resistance of the windings due to varying temperatures. Evidently, the addition of this second term implies a recording of the negative sequence values in healthy operation (ideally at the drive commissioning and in real operating conditions).

Thereafter, the magnitude of the vector subtraction $|\underline{x}^-_{\alpha\beta,f} - \underline{x}^-_{\alpha\beta,h}|$, should increase with the ITSC severity increase, as it is now independent of other abnormalities (like residual asymmetry), and the phase angle $\angle\underline{x}^-_{\alpha\beta,f} - \angle\underline{x}^-_{\alpha\beta,h}$ should allow for the localisation of the faulty phase.

3.3 Fault Feature Extraction

In this section, in order to accurately detect and diagnose the ITSC in non-stationary conditions, two methods were developed that are capable of extracting the fault index previously provided. The first method relies on the use of a time-frequency representation of $\underline{u}_{\alpha\beta}$ and of the estimated $\underline{e}_{\alpha\beta}$ to decompose these vectors into their positive and negative sequences. To further improve on this method, an algorithm was devised that will ease the desired frequency extraction by converting the signal into a spatial-domain stationary signal, making the order-tracking as simple as selecting the desired harmonic order. The second method relies on the multiple reference frames theory to decompose the phasors

at study, where LPFs are applied to separate the positive sequence component from the negative sequence component.

3.3.1 Time-Frequency Representation

Due to its simplicity and popular use, the STFT will be selected as the time-frequency signal-processing tool to be employed throughout this work.

Although the STFT has some disadvantages, like the a priori choice of a window function, and the time-frequency resolution, which makes it so that a high frequency resolution leads to a low time resolution (and vice-versa), this representation was found to be highly accurate for the desired application, consequently, the alternative pick, a quadratic representation, although supposedly having a better time-frequency resolution, was not used since it would bring more complexity to the system and increased computational burden.

The STFT requires three main parameters:

a) Window: a function that will be multiplied to each segment of the signal. The simplest function is a rectangular window, which is a constant value of 1. Most other window functions have a sinusoidal shape. The reason for this sinusoidal shape is because of a phenomenon called spectral leakage. This phenomenon is, simply put, a "leak" from the energy of the signal in a certain frequency into its neighbouring frequencies. When a segment is "cut off" from the signal, the edges have to be tapered (hence the sinusoidal shapes) to prevent discontinuities.

b) Window length: the length of each segment that will be "partitioned" from the signal. The window length increase leads to higher frequency resolution, but the total number of windows (segments) will decrease, resulting in a poorer time resolution.

c) Overlap length: This is the amount of overlap between windows. If set to zero, the windows do not overlap. As previously explained, the edges of the window function have to be smoothed out (tapered) to prevent discontinuities, which will lead to the inevitable loss of information. Therefore it is good practice to introduce an overlap big enough to counteract this loss. By default the overlap value is usually set to 75%.

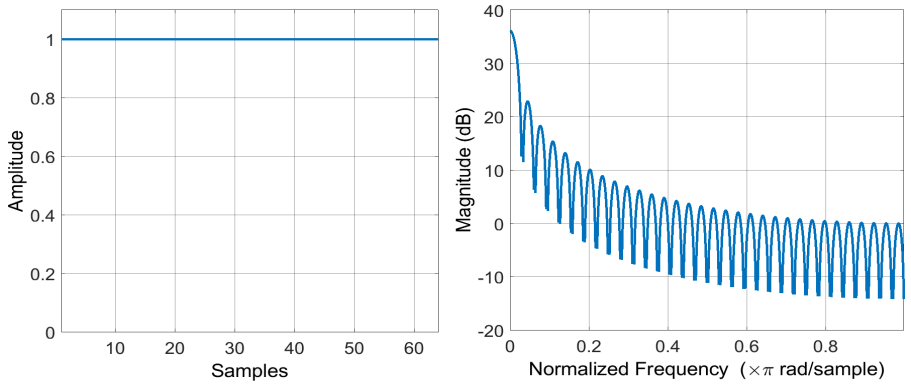

(a)

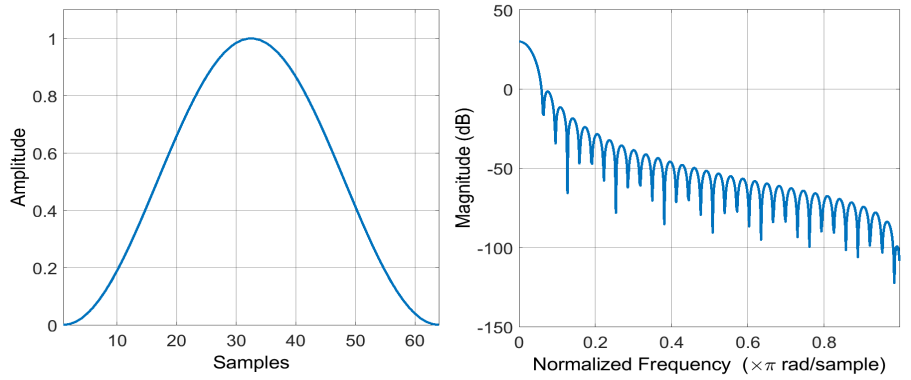

(b)

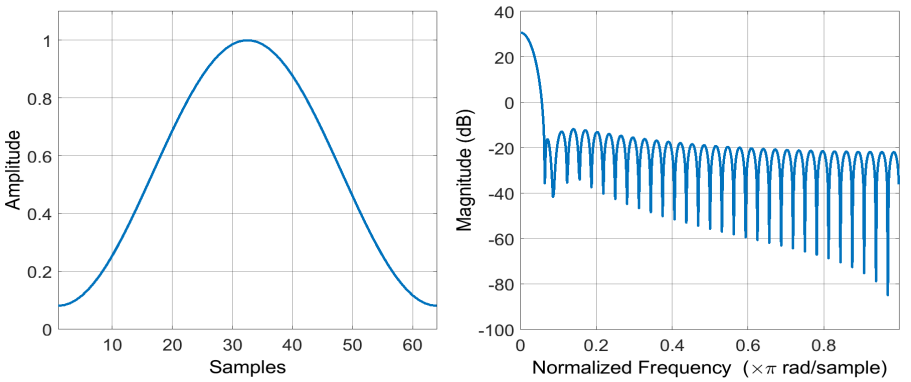

(c)

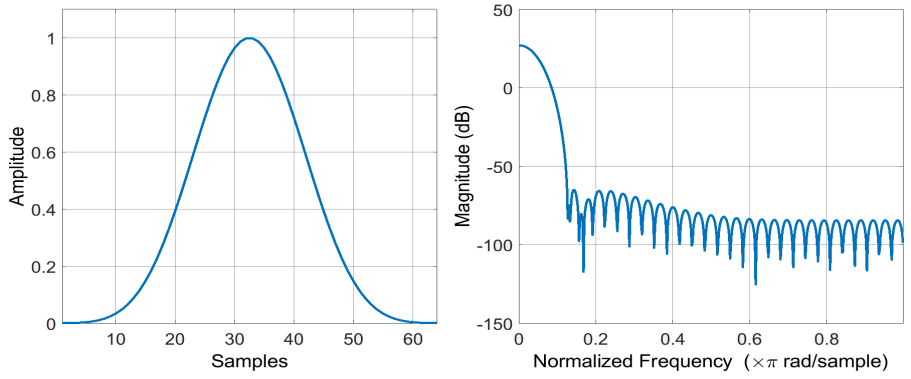

(d)

Figure 3.1: Window functions: (a) Rectangular; (b) Hann; (c) Hamming; (d) Blackman-Harris.

In Fig. 3.1 a comparison is made between four windows (in time domain and frequency domain): Rectangular (the simplest window), Hann, Hamming (both very popular in the literature), and a Blackman-Harris window, which for the purpose of this work was found as the one with the best trade-off between main lobe width, side lobe attenuation, and frequency resolution.

To identify the Blackman-Harris as the best window (for this application) a test signal was analysed. The signal is a faulty (ITSC) stationary stator voltage signal. Phase A1 of the machine was selected. This signal was acquired during 500ms and has 4001 samples. A window length of 2048 samples was selected (for a better computation, the window length should be a power of 2). The reason for this window length is the desire for a high frequency resolution without losing too much time resolution. The overlap length will be the default value of 75%. With this overlap the signal will be divided into four segments (if the overlap length was selected as 0%, the result would have been one segment, and therefore one single point to be analysed).

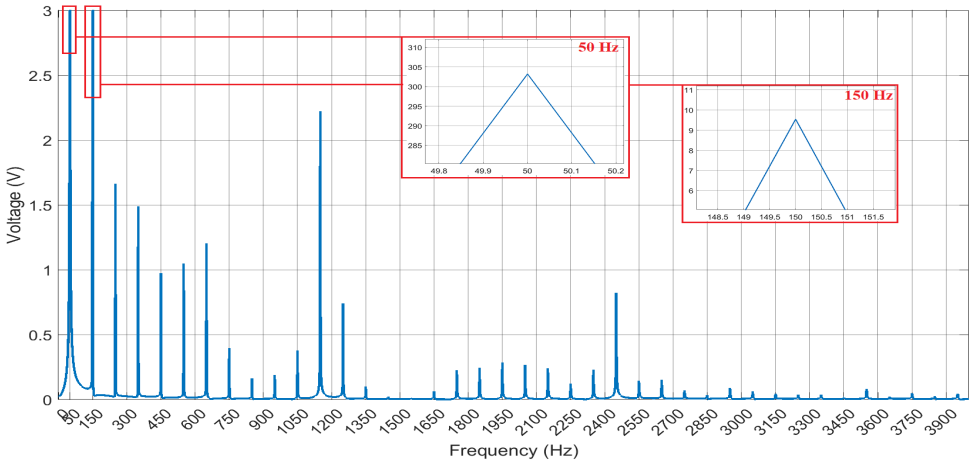

Figure 3.2: FFT of a phase voltage under an ITSC

Fig. 3.2 illustrates the harmonic content of the test signal. Since the fundamental frequency has the biggest magnitude it was selected as one of the harmonics to analyse, as it will certainly have a lot of side lobe frequencies. The 3rd harmonic is the closest to the fundamental frequency, and so, is prone to a bigger distortion due to spectral leakage. Finally, a high frequency harmonic was chosen. The 23rd harmonic was selected since it has the biggest magnitude among the high-frequencies. In Table 3.1, the amplitudes of the aforementioned harmonics when the STFT is applied to the voltage signal with four different window functions have been registered and compared to the amplitude obtained by a standard FFT, with a Hann window.

Table 3.1: Amplitude values of different spectral components obtained by four different window functions compared to the FFT.

	Fundamental	3rd Harmonic	23rd Harmonic
FFT (Hann)	303.209	9.543	2.219
STFT (Rectangular)	284.080 ± 1.821	7.978 ± 2.333	1.775 ± 0.313
STFT (Hamming)	294.234 ± 0.668	8.463 ± 0.34	2.452 ± 0,47
STFT (Hann)	295.531 ± 0.003	8.559 ± 0.003	2.074
STFT (Blackman-Harris)	298.709	8.936	2.166

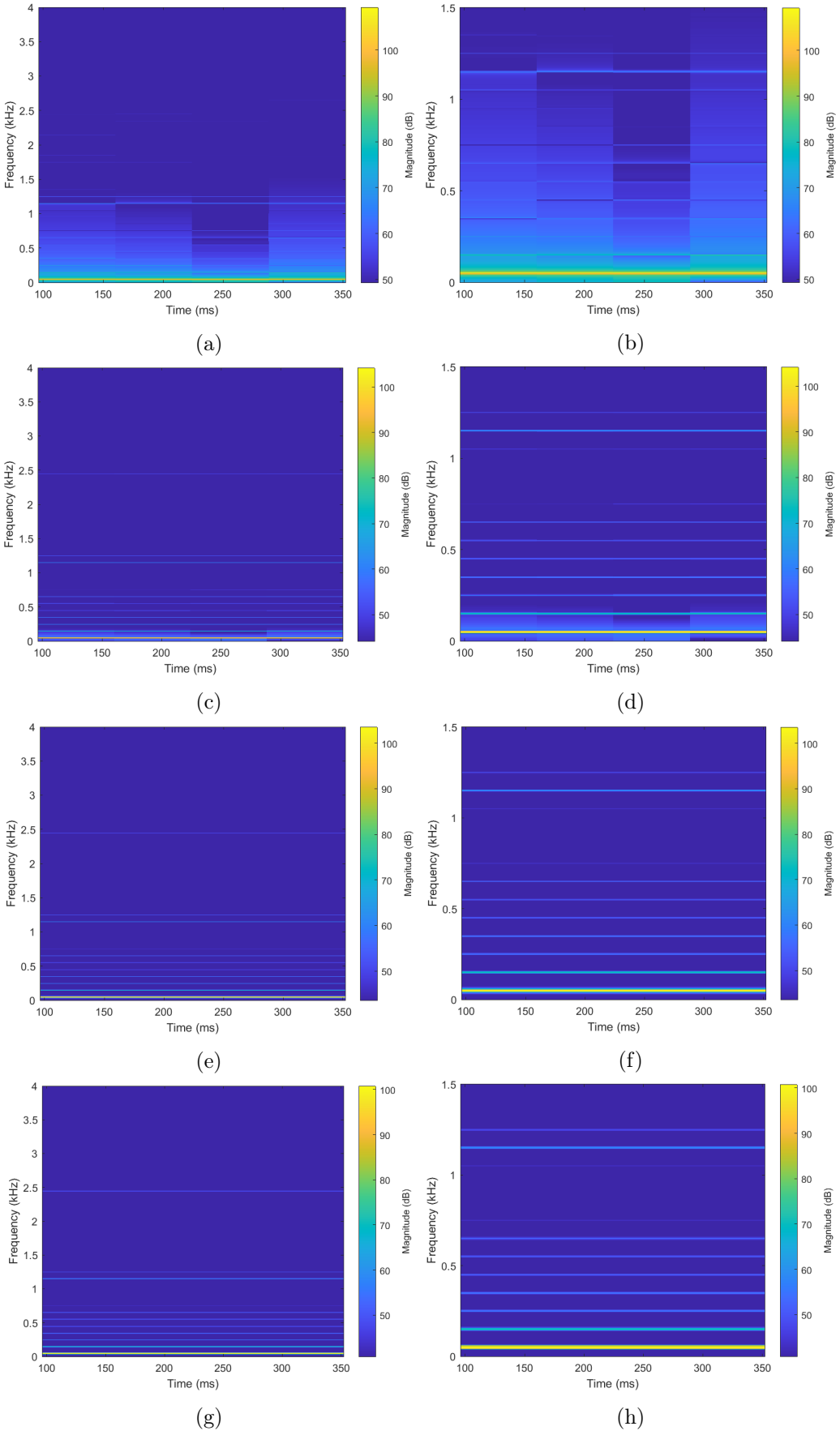

Figure 3.3: STFT of the test signal with four different windows: (a) Rectangular (Full); (b) Rectangular (Zoom in); (c) Hamming (Full); (d) Hamming (Zoom in); (e) Hann (Full); (f) Hann (Zoom in); (g) Blackman-Harris (Full); (h) Blackman-Harris (Zoom in).

Let us analyse Table 3.1. As mentioned, the choice of parameters for the STFT leads to the segmentation of the test signal into four portions. To make the analysis simpler, the four values were averaged and a deviation was calculated.

The rectangular window is easily recognisable as the less accurate. The values obtained with this window are the ones who are the furthest from the FFT values, and, except for the high-frequency component, its deviations are also the highest from the four windows. As was expected, the 3rd Harmonic is the one with the highest deviation since in the rectangular window there is no consideration for the spectral leakage. In the 23rd Harmonic, since it is the one with the highest magnitude among high-frequencies, it is expected to have a low spectral leakage, and so this deviation is also the lowest.

The Hamming window is more accurate than the rectangular window, and since it does take into consideration the spectral leakage (sinusoidal shape) the 3rd harmonic deviation is not as high as the rectangular window.

The Hann window has an higher accuracy than the Hamming window, and also shows a better side lobe attenuation of the fundamental frequency, proven by the very small deviation.

Finally, the Blackman-Harris proves to be the best window as its accuracy is higher than the Hann window, which is in and of itself an excellent window. The calculated deviation was rounded to the thousandths, and so this window appears to have no deviation, when in fact it has a very small deviation.

The graphical depiction of these values can be seen in Fig. 3.3, which shows, in a colour map, the STFT representation of the test signal with the four different windows. The low resolution of the rectangular window stands out, along with the boundaries between each one of the four segments.

3.3.2 Spatial-Domain Transform

In non-stationary conditions, the spectral components of a signal vary with time. This variation makes it harder to track the amplitude and phase of a desired frequency as it will be constantly changing with the variation of speed. To simplify this frequency tracking challenge, an algorithm was developed where the time-domain non-stationary signal is transformed into a spatial-domain stationary signal. This algorithm is hereby designated as the spatial-somain Transform (SDT).

The SDT is based on order-tracking [71] and synchronous averaging [72], [73] techniques, where the signal is resampled as a function of the rotor position instead of time, making the spectral components independent of speed. Theoretically, one could then use a frequency analysis tool such as the FFT to extract the fault features. In the case of this work, not only the speed variation will be studied but also a load torque variation, and so a time-frequency analysis is still required.

The SDT requires a time-domain signal, x, a position signal, p, that can either be estimated or measured, and lastly the width of the position interval to be sampled, W, in degrees. The basis of the SDT is to get the average of the time-domain signal in the interval W. The average value of every interval will be the output vector, y, which will be in order of the new position vector, n, which is the number of position intervals sampled. This vector can be converted to degrees by simply multiplying each n value with W.

In order to correctly write the SDT algorithm, some scenarios must be taken into account involving the choice of the position sampling width (W). Consider a stationary signal with a position step of one degree:

a) $W >= 1°$: When the position sampling width (W) is bigger than the position sample step, all intervals will certainly have samples, and so, all intervals can be averaged (Fig. 3.4(a)). For greater accuracy, interpolations are made at each

position upper limit, and a weighted average is calculated. Of course, the bigger the width (W) the bigger the loss of information (see Fig. 3.5).

b) $W < 1°$: When the position sampling width (W) is smaller than the sampled step there will be a certain number of intervals, depending on how small W is, where no sample exists (Fig. 3.4(b) and Fig. 3.4(c)). In these cases the only value will be an artificial one, created by the interpolation at the upper limit to allow the calculation of the interval average (weighted mean value). This interpolation can either be made to a single interval creating a single artificial point between sampled points, or multiple consecutive intervals generating multiple artificial points.

A flowchart of the spatial-domain transform algorithm is illustrated in Fig. 3.6.

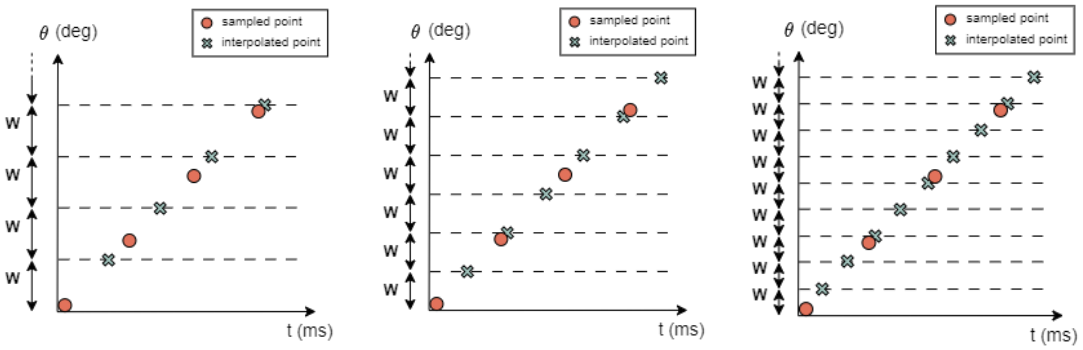

Figure 3.4: Different scenarios for the choice of the position sampling width (W): (a) All samples inside the intervals; (b) Sporadic single interval without a sample; (c) Consecutive intervals without samples.

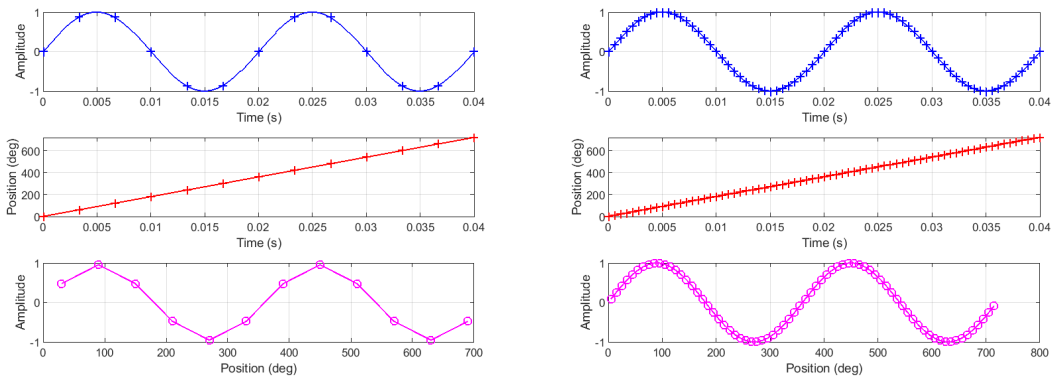

Figure 3.5: Time-domain signal, position signal and the resultant spatial-domain signal when W is set to: a) 60°; b) 10°.

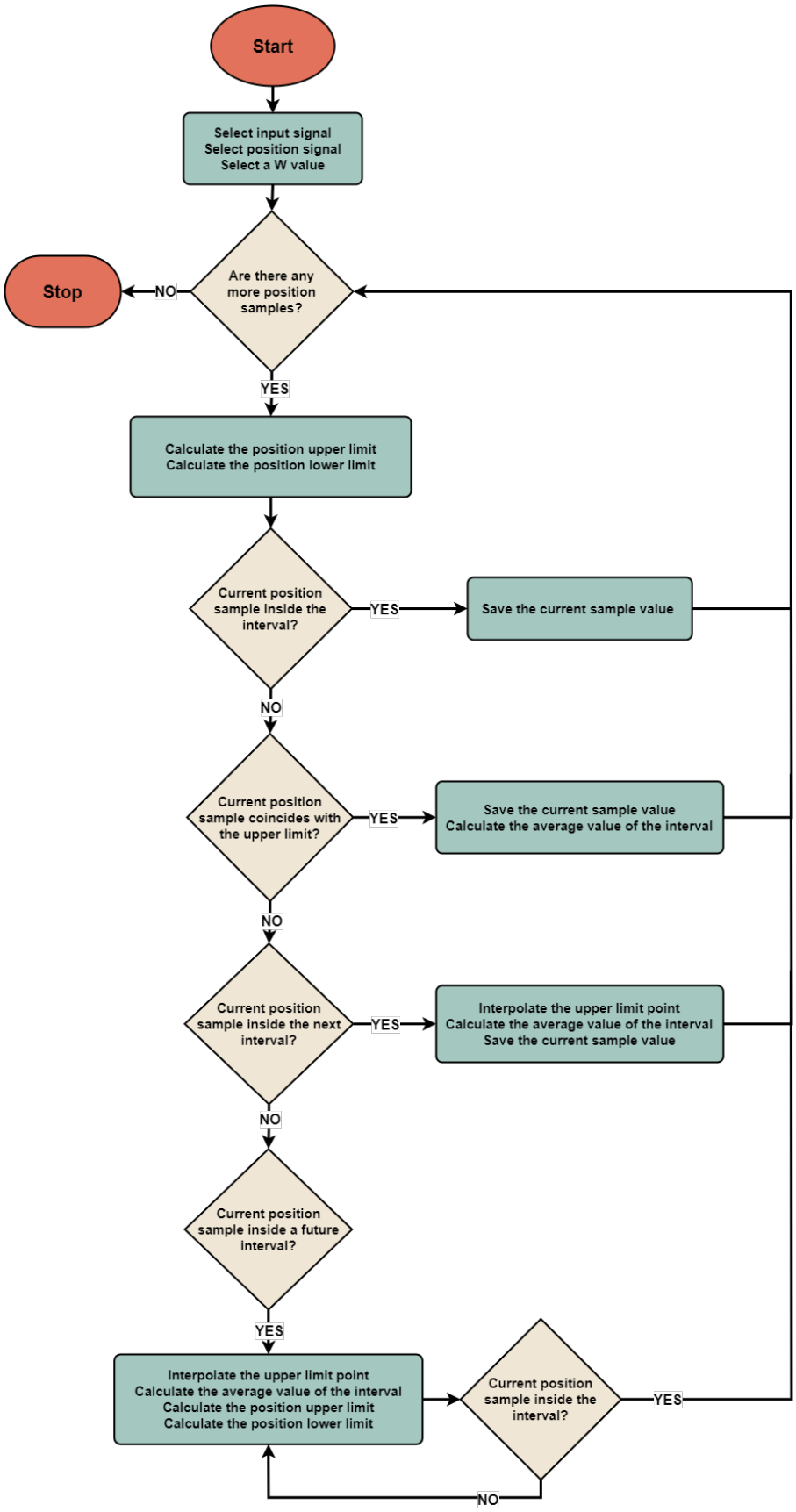

Figure 3.6: Flowchart of the spatial-domain transform algorithm.

An example of the operation of the SDT is presented in Fig. 3.5, where the first plot (top) represents the time-domain signal, the second plot (middle) the position signal and the last plot (bottom) the spatial-domain signal with a synthetic non-stationary signal. It is clear that the bigger the W interval is, the bigger the wave distortion will be, which directly translates into loss of information. In Fig. 3.7 the SDT was applied to a non-stationary synthetic signal.

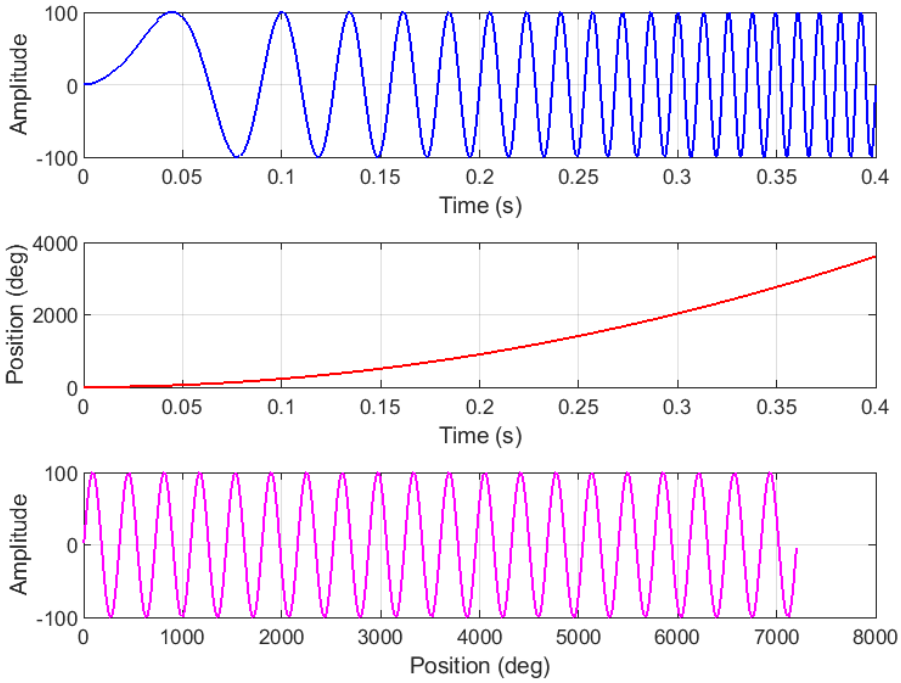

Figure 3.7: SDT applied to a non-stationary (with varying frequency) signal.

It now becomes necessary to test the SDT accuracy to prove that it can convert the signal while preserving most of its original information. The same analysis used to test the STFT will be made (in terms of chosen harmonics). The original position sample step of the tested signal is 1.125°. Different position sampling intervals (W) are chosen to study the relation between the value of W and the accuracy of the SDT. The data was collected and is presented in Table 3.2.

Table 3.2: Amplitude values of different spectral components obtained with five different SDT position sampling widths (W).

	W	Fundamental	3rd Harmonic	23rd Harmonic
FFT before SDT	-	303,209	9,543	2,219
FFT after SDT	0.1	303,228	9,489	2,149
FFT after SDT	1	303,212	9,484	2,092
FFT after SDT	1.125	303,208	9,483	2,071
FFT after SDT	2	303,166	9,470	1,910
FFT after SDT	10	301,689	9,037	-

The SDT main loss of information is centred around high frequencies, although the low frequency component, 150 Hz (3rd Harmonic), sees a decrease of 0.6 V. An appeal

to ridicule is made by choosing a width of 10 degrees. In this case, all the information after the 450 Hz component (9th harmonic) is lost, but still, the low frequencies show a fairly small loss in such an extreme width choice. In comparison, the small width of 0.1° introduces very small errors in the amplitudes of the frequency components of the signal, meaning that the selection of the position interval width should be preferably done with small values in hopes of getting below the position sample step value and avoid a bigger loss of information.

3.3.3 Multiple Reference Frames Theory

Unfortunately, the usage of a time-frequency representation, even with the reduced complexity brought by the SDT, still has a major drawback — its online capability. Given the nature of the ITSC, it is desired for the diagnostic to be as fast as possible, enough so that a fault tolerant control can intervene in guaranteeing a safe operation of the motor until a repair is scheduled.

In this work, the online technique proposed is based on the Multiple Reference Frames (MRF) theory.

The usage of the MRF theory in the analysis of electrical machines is not new. In fact, the first recorded mention to this method dates back to 1968, where it was applied to the analysis of the steady-state modes of symmetrical induction machinery [74]. Since then, the MRF theory has been used in the diagnostic of open-phase faults in six-phase asymmetrical PMSMs [16] and in the diagnostic of interturn short-circuits in induction motors [75].

To measure the fault signatures, one important property of the MRF theory will be explored. This property states that there is always a reference frame in which a certain component from a given variable appears as constant, that is, can be transformed into a dc component.

Knowing this, by applying equation 3.8, to the $\underline{x}_{\alpha\beta}$ signal, the positive sequence component will be transformed into a dc component, while the negative sequence component will have a sinusoidal representation and the synchronous reference frame will rotate in the anti-clockwise direction. On the other hand, by applying the inverse of equation 3.8, written as,

$$R' = \begin{bmatrix} cos(\theta) & -sin(\theta) & 0 & 0 & 0 & 0 \\ sin(\theta) & cos(\theta) & 0 & 0 & 0 & 0 \\ 0 & 0 & cos(\theta) & sin(\theta) & 0 & 0 \\ 0 & 0 & -sin(\theta) & cos(\theta) & 0 & 0 \\ 0 & 0 & 0 & 0 & 1 & 0 \\ 0 & 0 & 0 & 0 & 0 & 1 \end{bmatrix}, \tag{3.17}$$

to the $x_{\alpha\beta}$ signal, the synchronous reference frame will rotate in clockwise and the negative sequence component will now appear as the dc component while the positive sequence component will have a sinusoidal representation. This way, by applying two different rotations to the $x_{\alpha\beta}$ signal, the positive and negative sequences can be easily measured. Lastly, since the negative sequence is much smaller than the positive sequence, after (3.17) is applied to the $x_{\alpha\beta}$ signal and the negative sequence component is turned into a dc component, a low-pass filter must be used to remove the positive sequence from the signal. Fig. 3.8 shows a schematic representation of the MRF implementation in the control platform.

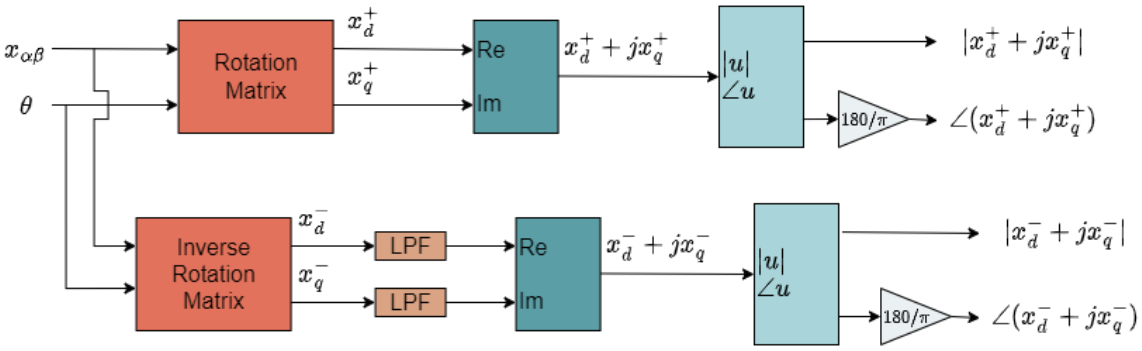

Figure 3.8: MRF implementation diagram.

Chapter 4

Simulation Results

To validate the two methods proposed in Chapter 3, a co-simulation of the 6-PMSM was used with a 2-D FEA model of the 6-PMSM [69], in ANSYS/Simplorer environment, together with the control strategy used, Predictive Current Control, already implemented in MATLAB/Simulink [76]. The simulation parameters are displayed in Appendix A, as well as an overview of the different simulation environments.

Three different studies were carried out: a speed variation study, a load torque variation study, and a final study with a combined speed and load torque variation. The total number of turns per winding, N_t, in this custom-made 6-PMSM is 208 (26 turns per coil). To analyse the sensitivity of both methods to different fault degrees, the following numbers for shorted turns, N_f, were chosen: seven short-circuited turns, three short-circuited turns and one short-circuited turn. With the corresponding ratios, μ, (shorted turns to total number of turns) being 3.4%, 1.4% and 0.5%, respectively. Additionally, to test the sensitivity of the proposed methods to different fault resistance values, R_f, a resistor was added in the shorted path. For a good and easy recognition of the fault, the fault resistance value was set to 1 $m\Omega$, in an attempt to simulate a dead short-circuit. For the incipient fault scenario, the resistance value was set arbitrarily to 1 Ω.

4.1 Offline Method

A normalisation to the SDT's new position vector p' (built from the n values), in the form of $p'_{norm} = p' \frac{180p}{W}$ is made, so that for any W value the frequency components appear at the same frequency. As such, instead of having a frequency vector (in Hz) we will have an harmonic order vector. Being that the machine in study has two pole-pairs, $p = 2$, the fundamental frequency will be present at second order, making a single harmonic order equivalent to 25 Hz. Since the desired frequency is known, and is made constant, it is now simple to extract all the information needed from the STFT by just sifting through the new frequency vector in search of the desired harmonic order index, and then using that index to locate the corresponding row in the said matrix.

Because of this normalisation, the x-axis from the spatial-domain signal will come in number of revolutions. Using this knowledge, the window length of the STFT will be selected as a multiple of 360 (since a revolution is 360°). Since we are in the simulation phase and the results are expected to be clear and noise free, the selected window length was 720 (chosen empirically), which is a very low value given that the simulations were made with a time period of 2 seconds [1]. Getting a larger window would lead to time information loss, which in this case is not worth it since the increase in frequency resolution will not improve

[1] Considering the example of a PMSM running at 1500rpm during a time period of 2 seconds, the number of complete rotations made by the rotor of the machine would be 50, in other words, 18000°.

noticeably. Additionally, given the greater time-resolution, a better understanding of this method at lower speeds will be achieved. This will not be possible in the experimental stage as the signals are expected to be noisier and so a better frequency resolution will more relevant.

Finally, and as explained in Chapter 3, the choice of window for this dissertation is the Blackman-Harris and the overlap lenght will be 75%.

4.1.1 Speed Variation

To show the effects of varying speeds in the proposed fault index, these simulations were done with the speed ramping from 0 to 1500 rpm in just 2 seconds. The current references were set to $i^*_{qs} = 4.8$ A and $i^*_{ds} = i^*_{xs'} = i^*_{ys'} = 0$ A for maximum torque per ampere conditions. The rotor speed, rotor position, fault currents and electromagnetic torque results from this study are illustrated in Fig. 4.1.

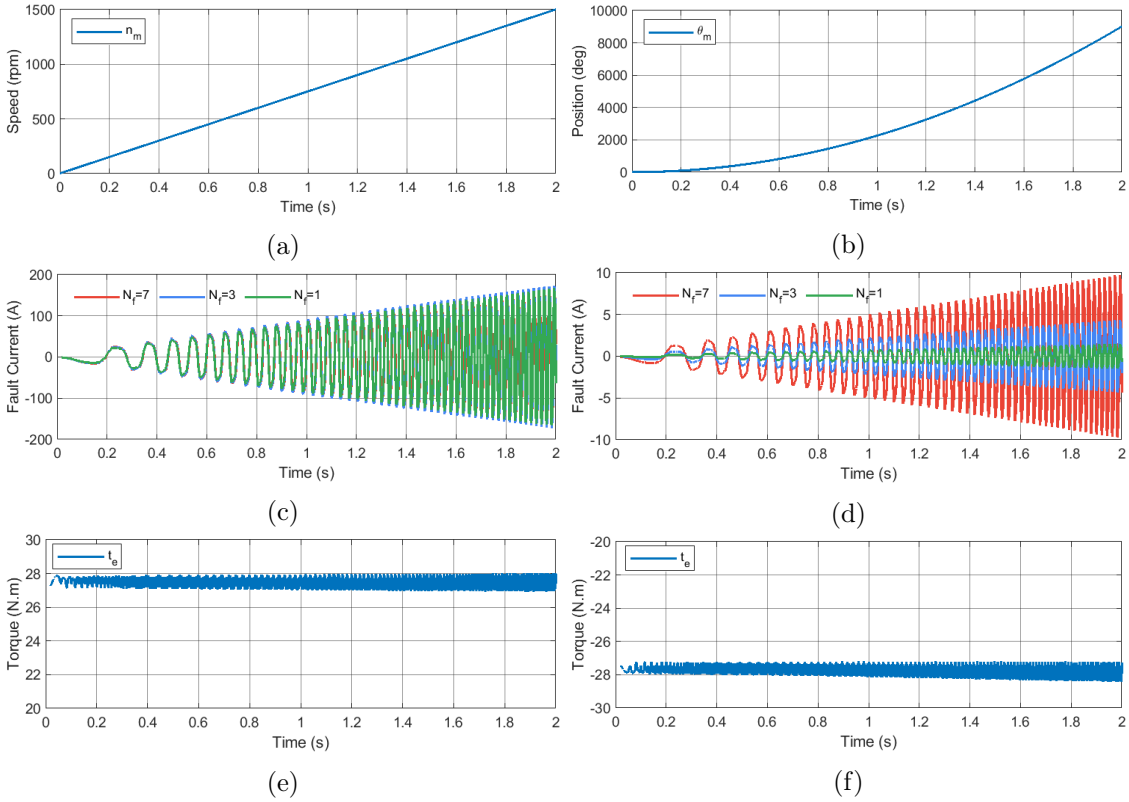

Figure 4.1: Computational results for speed varying conditions with 100% of the rated load: (a) Rotor Speed; (b) Rotor Position; (c) Fault Currents ($R_f = 1\ mOhm$); (d) Fault Currents ($R_f = 1\ Ohm$); (e) Electromagnetic Torque (Motor); (f) Electromagnetic Torque (Generator)

Amplitudes

According to the findings depicted in Fig. 4.2 and Fig. 4.3, a conclusion can be drawn regarding the correlation between the speed and the fault feature amplitudes ($|\underline{u}^-_{\alpha\beta}|$ and $|\underline{e}^-_{\alpha\beta}|$). This findings suggest a clear relationship between the rotational speed of the motor and the amplitude of the fault indicators: as the speed increases, both fault indicator's amplitudes become larger.

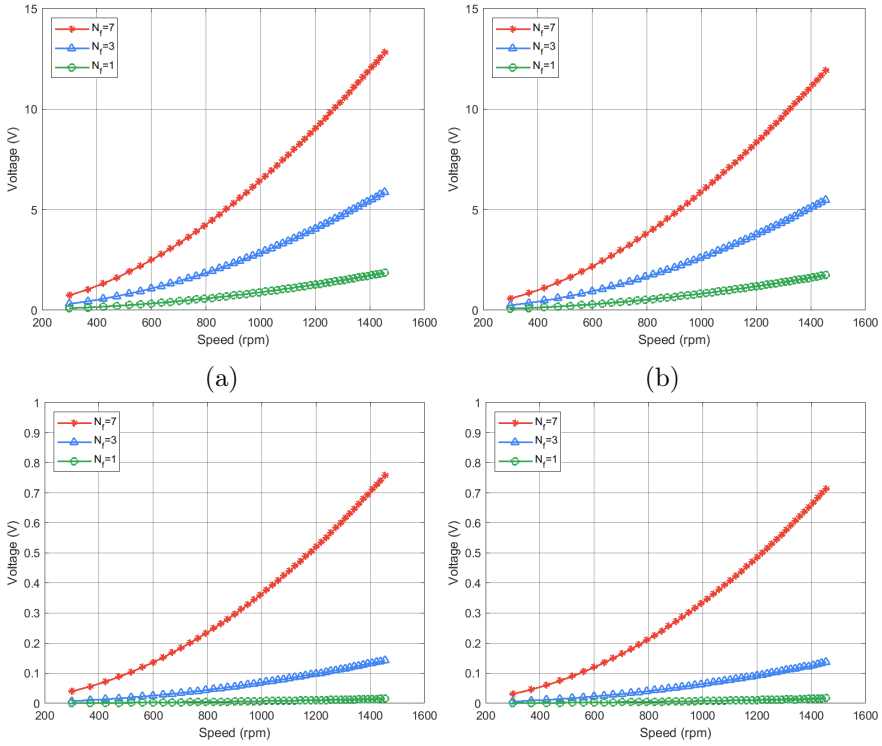

Figure 4.2: Amplitude variation of $|\underline{u}^{-}_{\alpha\beta}|$ in speed varying conditions with 100% of the rated load: (a) Motor with $R_f = 1\ m\Omega$; (b) Generator with $R_f = 1\ m\Omega$; (c) Motor with $R_f = 1\ \Omega$; (d) Generator with $R_f = 1\ \Omega$;

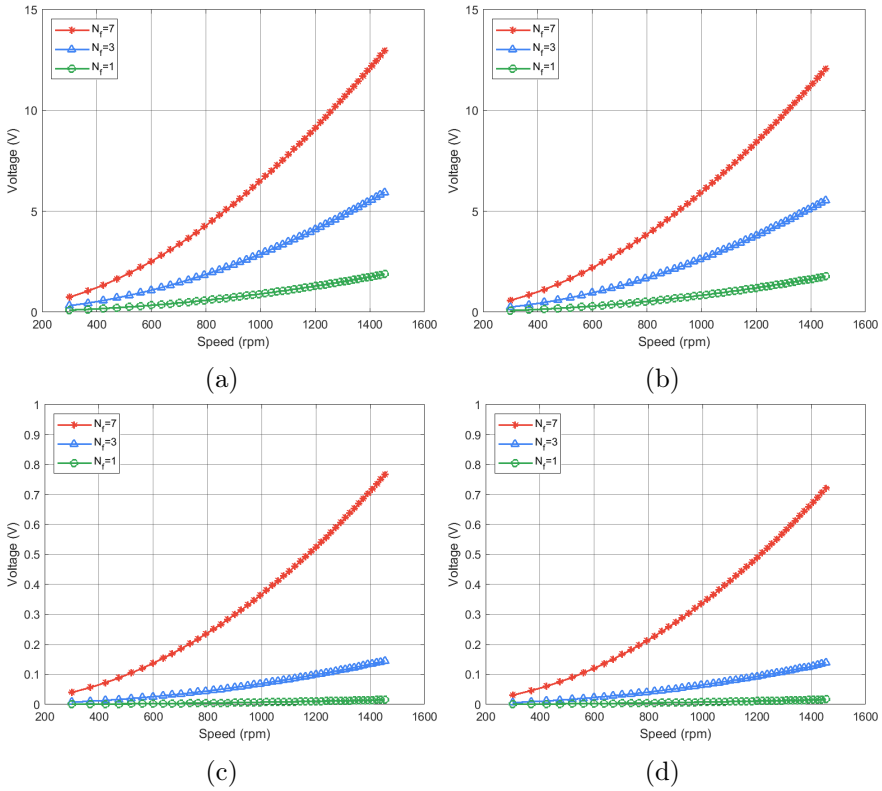

Figure 4.3: Amplitude variation of $|\underline{e}^{-}_{\alpha\beta}|$ in speed varying conditions with 100% of the rated load: (a) Motor with $R_f = 1\ m\Omega$; (b) Generator with $R_f = 1\ m\Omega$; (c) Motor with $R_f = 1\ \Omega$; (d) Generator with $R_f = 1\ \Omega$;

Phases

As for the phase variation, shown in Fig. 4.4 and Fig. 4.5, a lot of information can be retrieved.

Firstly, the increase in speed causes the phase angle to decrease. However, in the dead short-circuit scenario, the seven short-circuited turns, and the third short-circuited turns (to a lesser extent), show a saturation effect, where the phase decrease reaches a limit and starts increasing. In both Fig. 4.4(a) and Fig. 4.4(b) for $\underline{u}^{-}_{\alpha\beta}$ and Fig. 4.5(a) and Fig. 4.5(b) for $\underline{e}^{-}_{\alpha\beta}$, it can be observed that this saturation effect causes the phase variation of the seven short-circuited turns fault (and the three short-circuited turns fault) to be smaller. Disregarding the saturation effect, and taking into account the overall phase variation, for every number of shorted turns, and for both the dead short-circuit and incipient short-circuit, is $\approx 25°$. This phase decrease is small enough to enable a mapping for the fault localisation. In fact, since there are six phases, the biggest interval to locate the fault would have to be a 60° interval, thus dividing the 4-quadrant reference into six equal parts. Although in the case of a dead short-circuit ($R_f = 1\ m\Omega$) the angle curves get further apart from each other with the increase in speed (due to the saturation effect), the overall phase variation (considering the highest and lowest angles amongst all fault scenarios) is still small enough to pinpoint the location of the fault to a certain phase ($25° < 60°$).

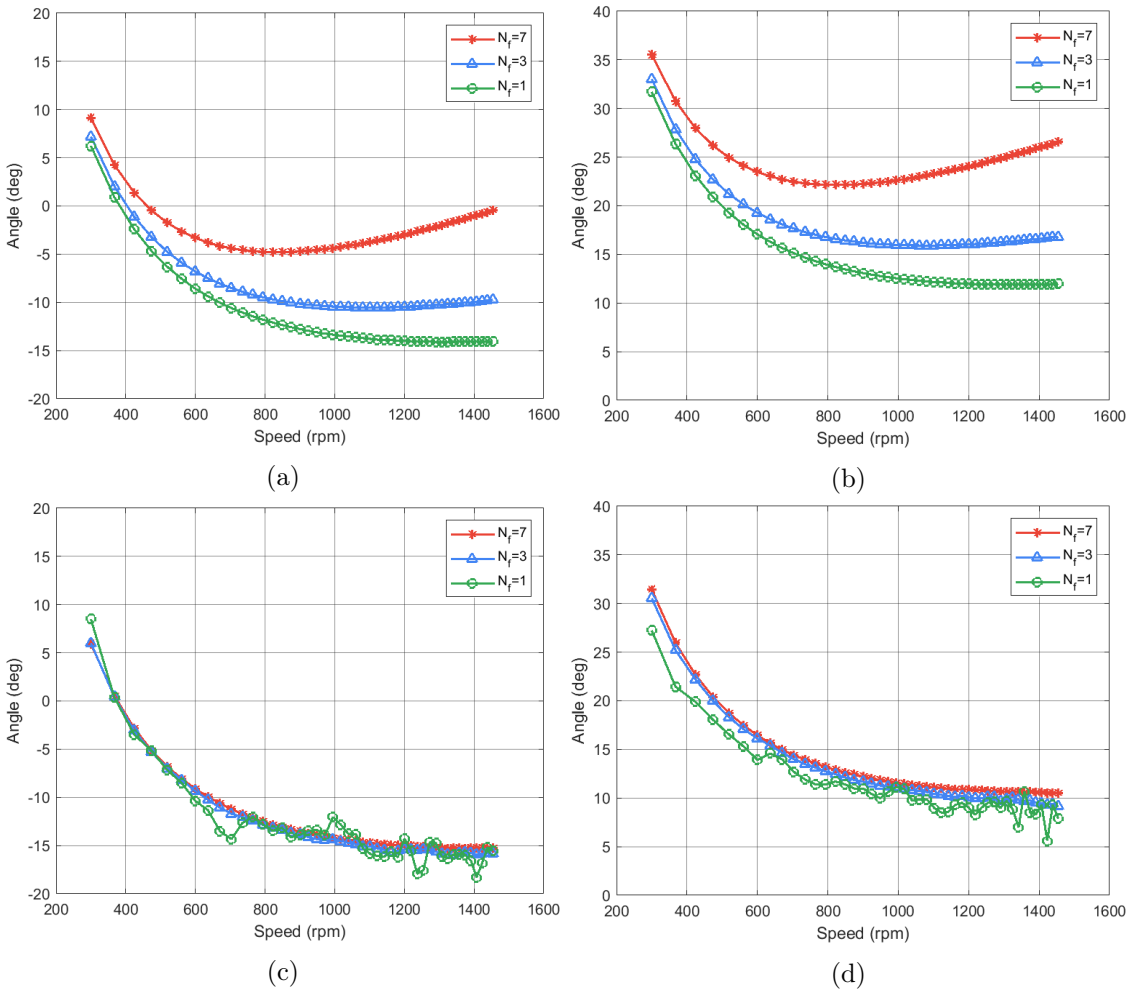

Figure 4.4: Phase variation of $\underline{u}^{-}_{\alpha\beta}$ in speed varying conditions with 100% of the rated load: (a) Motor with $R_f = 1\ m\Omega$; (b) Generator with $R_f = 1\ m\Omega$; (c) Motor with $R_f = 1\ \Omega$; (d) Generator with $R_f = 1\ \Omega$;

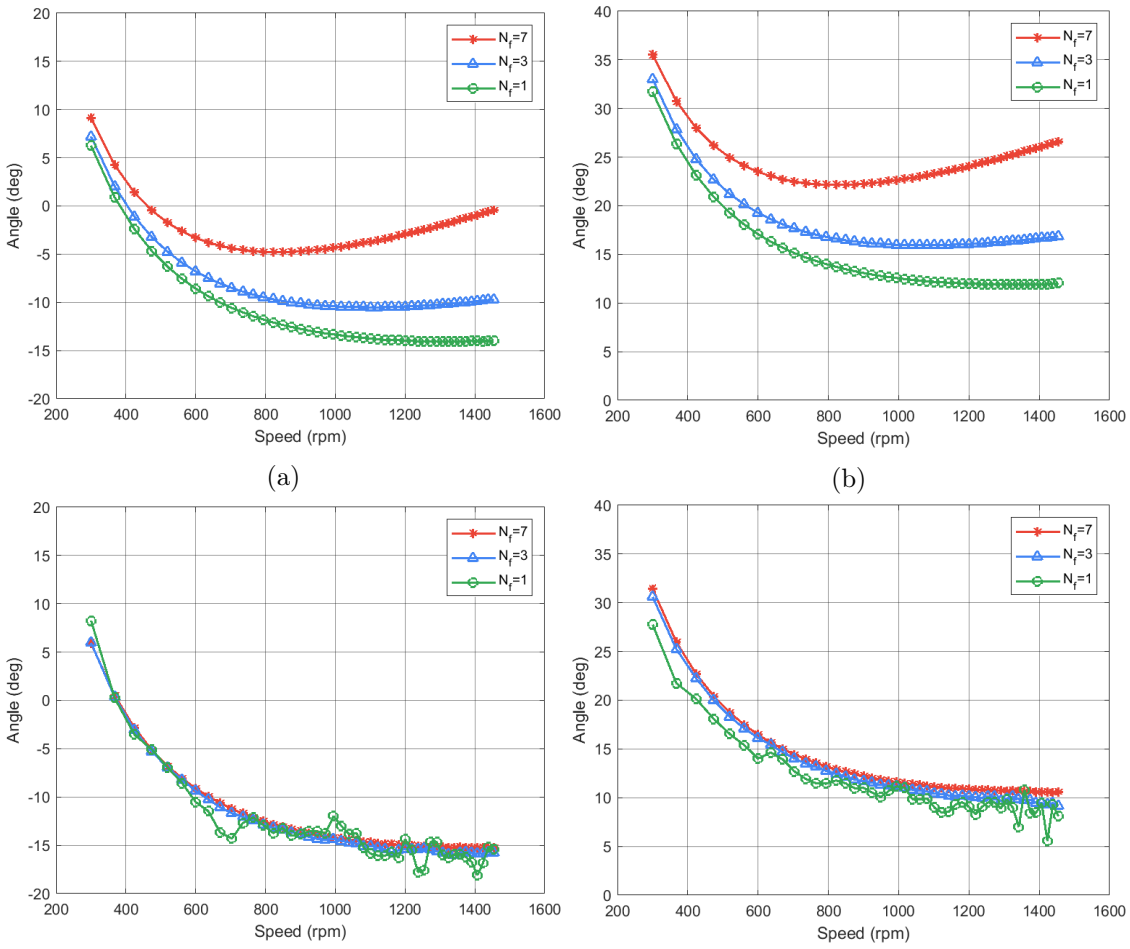

Figure 4.5: Phase variation of $\underline{e}^{-}_{\alpha\beta}$ in speed varying conditions with 100% of the rated load: (a) Motor with $R_f = 1\ m\Omega$; (b) Generator with $R_f = 1\ m\Omega$; (c) Motor with $R_f = 1\ \Omega$; (d) Generator with $R_f = 1\ \Omega$;

Lastly, the incipient fault ($R_f = 1\ \Omega$) with one short-circuited turn shows a very different behaviour compared to all other curves, illustrated in Fig. 4.4(c) and Fig. 4.4(d) and Fig. 4.5(c) and Fig. 4.5(d). This oscillation behaviour could be caused by two things: the fault is so small that it is hard to get the phase information, or, the time-frequency signal processing tool, although found to be accurate, is not accurate enough in the retrieval of the phase information.

Fault Severity

The fault severity (3.16) greatly depends on the amplitude of the negative sequence. As such, an assumption can be made regarding the correlation between the variation of this index and the amplitude variation displayed earlier in Fig. 4.2 and Fig. 4.3. By examining Fig. 4.6 and Fig. 4.7, which represent the effect of speed variation in the fault severity index, it becomes evident that this assumption is correct since the fault severity of both $\underline{u}^{-}_{\alpha\beta}$ and $\underline{e}^{-}_{\alpha\beta}$ also increase with speed. It was previously stated that the incipient fault with only one short-circuited turn was very difficult to detect. It is now possible to infer just how slight this fault is since its fault severity is lower than 0.01% for both voltage and back-EMF fault features. Lastly from the comparison of the fault severity index of $\underline{u}^{-}_{\alpha\beta}$ and of $\underline{e}^{-}_{\alpha\beta}$ it can be seen, specially in the seven short-circuited turns fault, that the estimated back-EMF has a slightly higher sensitivity than the stator voltages.

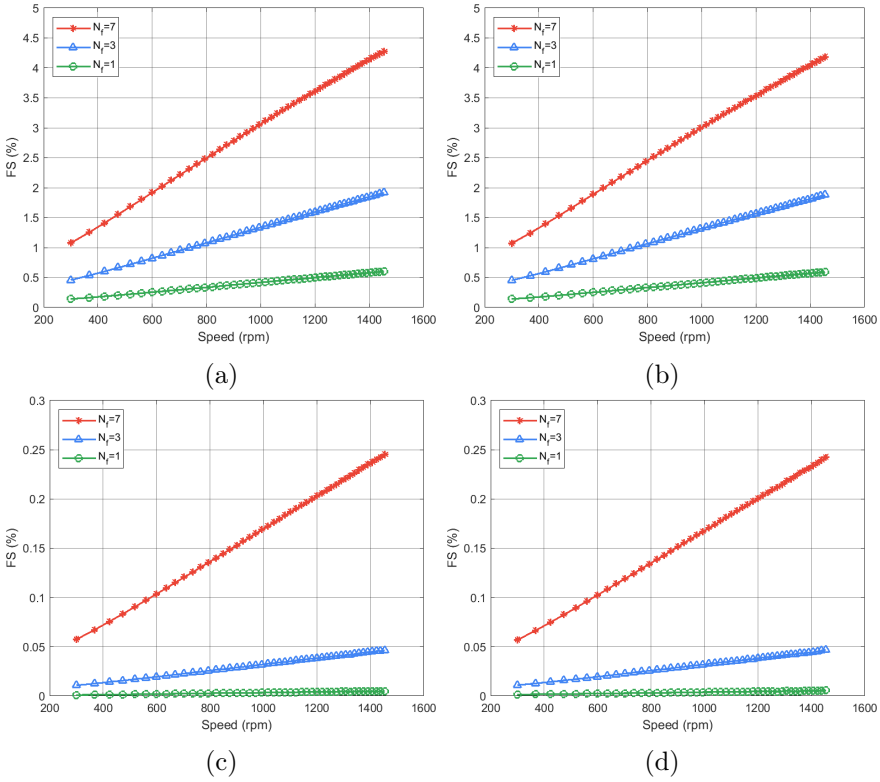

Figure 4.6: Fault severity variation of $\underline{u}^{-}_{\alpha\beta}$ in speed varying conditions: (a) Motor with $R_f = 1\ m\Omega$; (b) Generator with $R_f = 1\ m\Omega$; (c) Motor with $R_f = 1\ \Omega$; (d) Generator with $R_f = 1\ \Omega$;

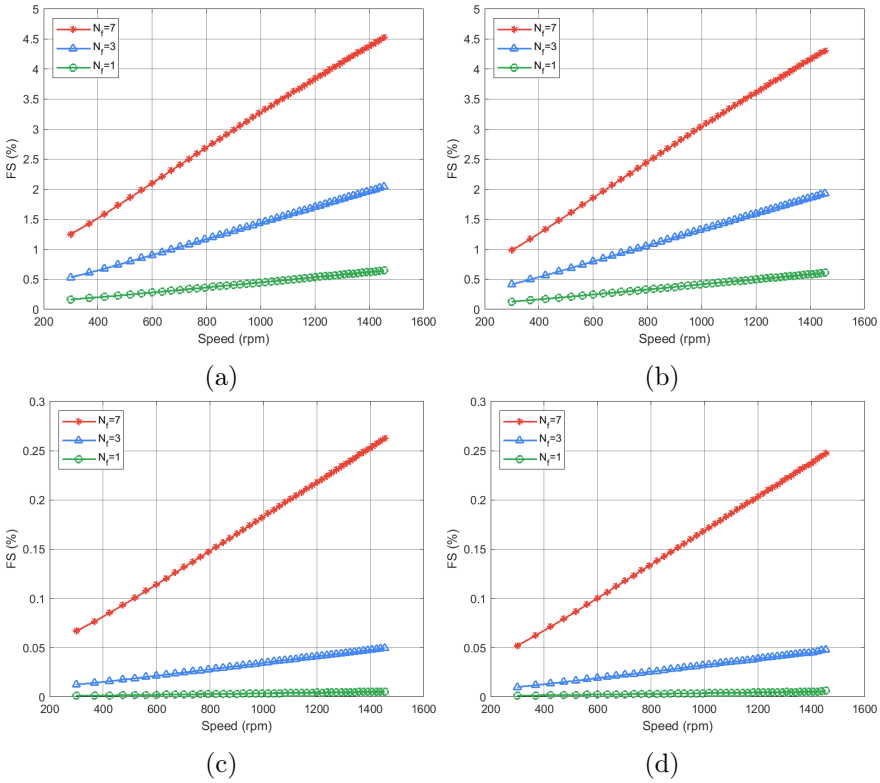

Figure 4.7: Fault severity variation of $\underline{e}^{-}_{\alpha\beta}$ in speed varying conditions: (a) Motor with $R_f = 1\ m\Omega$; (b) Generator with $R_f = 1\ m\Omega$; (c) Motor with $R_f = 1\ \Omega$; (d) Generator with $R_f = 1\ \Omega$;

Normalised Fault Severity

It was shown that the fault severity of the ITSC increases with the increase in speed, which was to be expected since the amplitudes of the fault features also increase. However, it is hard to recognise what the exact meaning of the fault severity values are and what they represent. As explained in Chapter 3, the fault severity should increase linearly with the increase of the number of short-circuited turns as well as with the magnitude of the fault current that passes through the shorted path. In that sense, if the fault severity were to be divided by the fault current, an estimation of the number of short-circuited turns should be achieved. Although it is not reasonable to ask for the measurement of i_f in real-world applications, in this test setup, the measurement of the fault current is possible and desirable, as to evaluate if the proposed fault severity index (without a normalisation) performs well.

To do this, the fault severity index was normalised by doing,

$$FS_{norm} = \frac{FS}{|i_f|} \tag{4.1}$$

The results of this normalisation are presented in Fig. 4.8 and Fig. 4.9 for both $\underline{u}^{-}_{\alpha\beta}$ and $\underline{e}^{-}_{\alpha\beta}$ respectively.

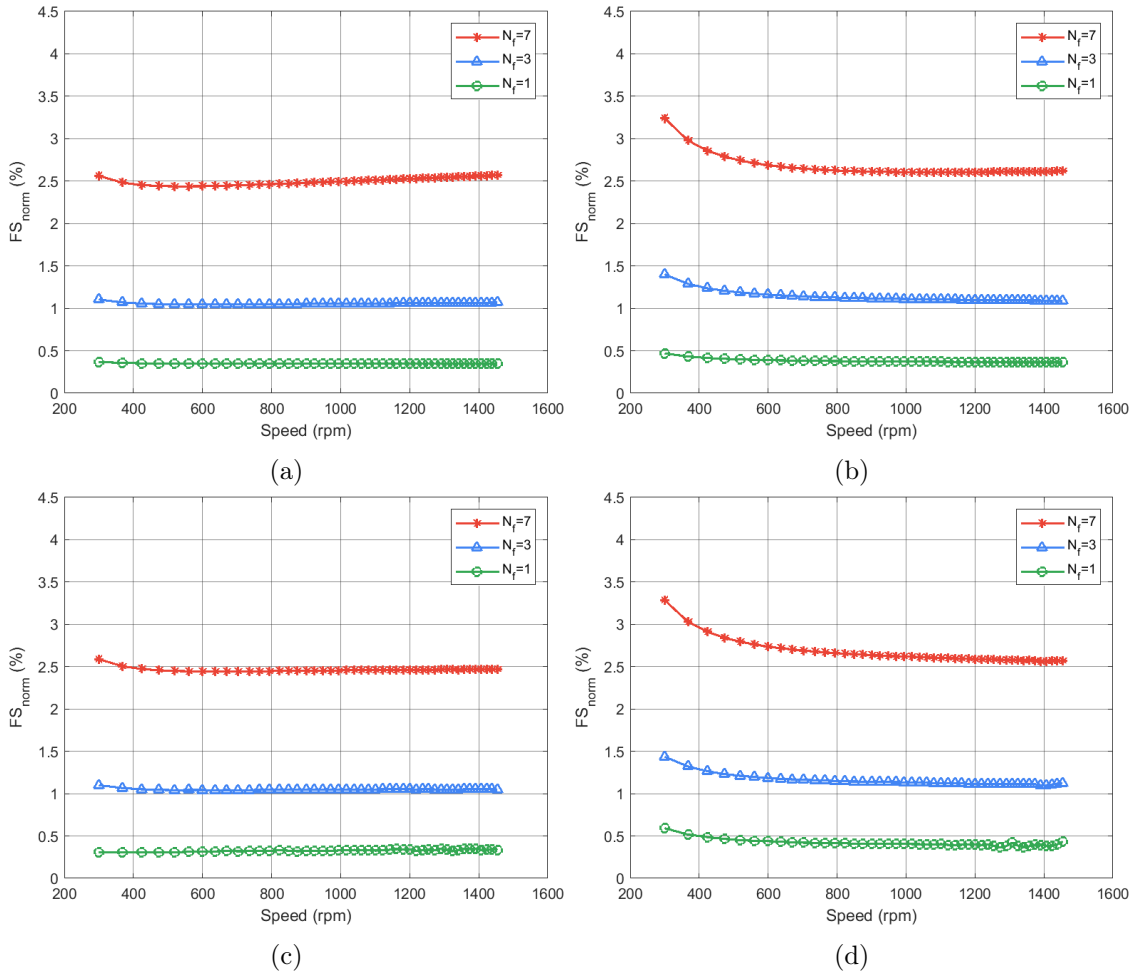

Figure 4.8: Normalised fault severity of $\underline{u}^{-}_{\alpha\beta}$ in speed varying conditions: (a) Motor with $Rf = 1\ m\Omega$; (b) Generator with $Rf = 1\ m\Omega$; (c) Motor with $Rf = 1\ \Omega$; (d) Generator with $Rf = 1\ \Omega$;

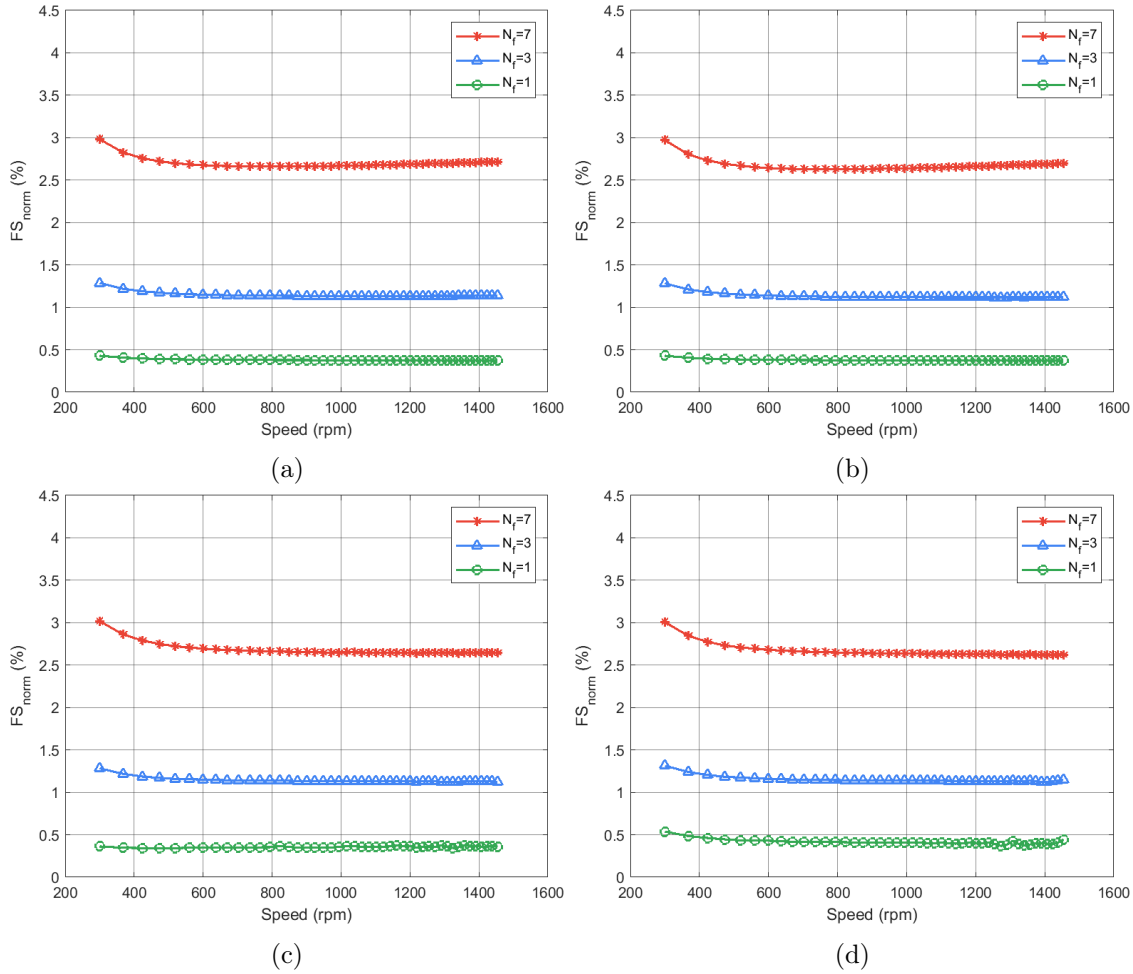

Figure 4.9: Normalised fault severity of $\underline{e}^{-}_{\alpha\beta}$ in speed varying conditions: (a) Motor with $Rf = 1\ m\Omega$; (b) Generator with $Rf = 1\ m\Omega$; (c) Motor with $Rf = 1\ \Omega$; (d) Generator with $Rf = 1\ \Omega$;

From the analysis of these figures and by comparing the obtained values with the short-circuited turn ratios, μ, provided in the beginning of this Chapter, it is possible to evaluate the effectiveness of this index in determining the number of short-circuited turns, N_f. A comparison between these values is summarised in Table 4.1

Table 4.1: Comparison between the ratio of short-circuited turns to total turns in a winding vs normalised fault severity values.

N_f	μ (%)	$FS^{e}_{norm}(\%)$	$FS^{u}_{norm}(\%)$
7	3.4	2.7	2.5
3	1.4	1.2	1.1
1	0.5	0.3	0.3

Although the normalised fault severity values are below the real ratios of short-circuited turns, and thus are not exactly accurate, they represent a close estimation of μ. The values presented in Fig. 4.8 and Fig. 4.9 are overall constant, which is also in line with the expected, since the normalised fault severity should now be independent of the fault current, and for that reason, should not vary with the varying frequency or with changes in the fault resistance values. Lastly, the estimated back-EMF is slightly more accurate

than the stator voltage, since it is also slightly more sensitive to the ITSC.

4.1.2 Load Torque Variation

The load variation analysis was made with a stationary speed of 1500 rpm and with i_{qs}^{*} ramping from 0 to 4.8 A in 2 seconds.

Since the speed is now stationary, it would not make sense to show the signal varying with speed, as was previously shown, and so the rotor position received by the SDT (in number of revolutions) is now used as the x-axis. The rotor speed, rotor position, fault currents and electromagnetic torque results from this study are illustrated in Fig. 4.10.

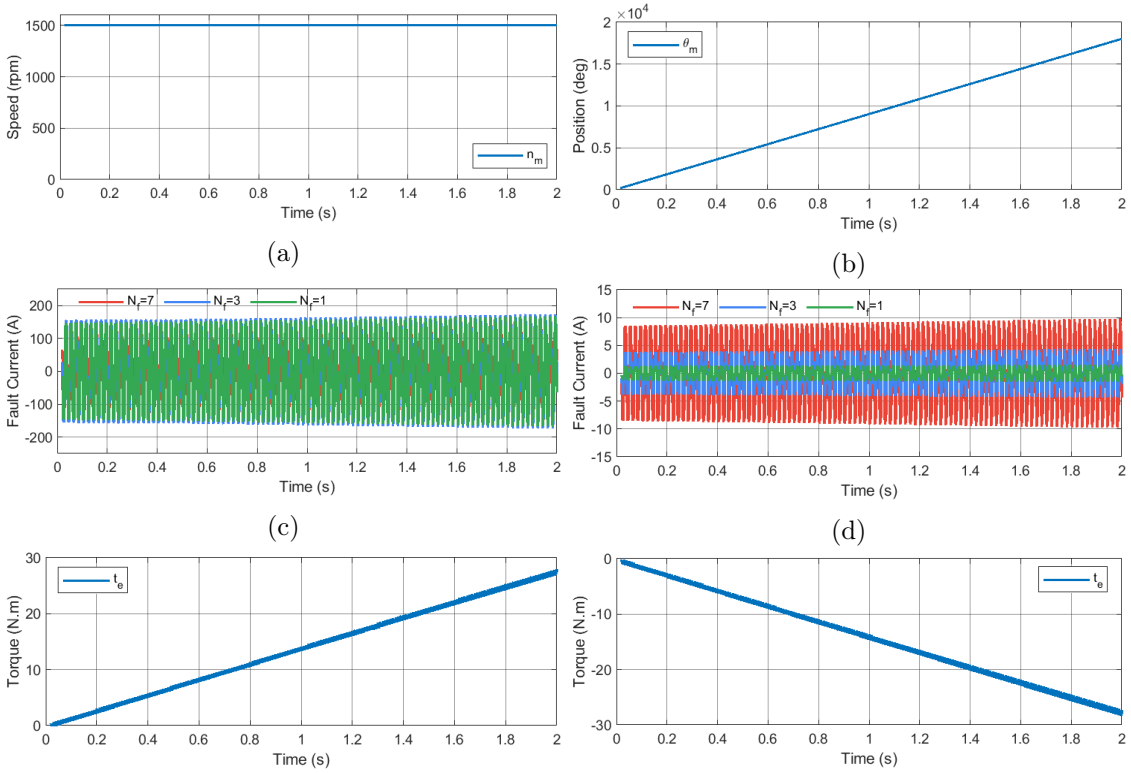

Figure 4.10: Computational results for load torque varying conditions with 100% of the rated speed (1500 rpm): (a) Rotor Speed; (b) Rotor Position; (c) Fault Currents (R_f = 1 $mOhm$); (d) Fault Currents (R_f = 1 Ohm); (e) Electromagnetic Torque (Motor); (f) Electromagnetic Torque (Generator)

Amplitudes

The plotted data in Fig. 4.11 and Fig. 4.12, suggests that the amplitudes of the fault indicators remain relatively stable despite changes in the load torque. This indicates that the fault indicators are robust to load variations, making them reliable indicators for fault detection in the presence of load torque changes and emphasises the importance of distinguishing fault-related effects from external load variations.

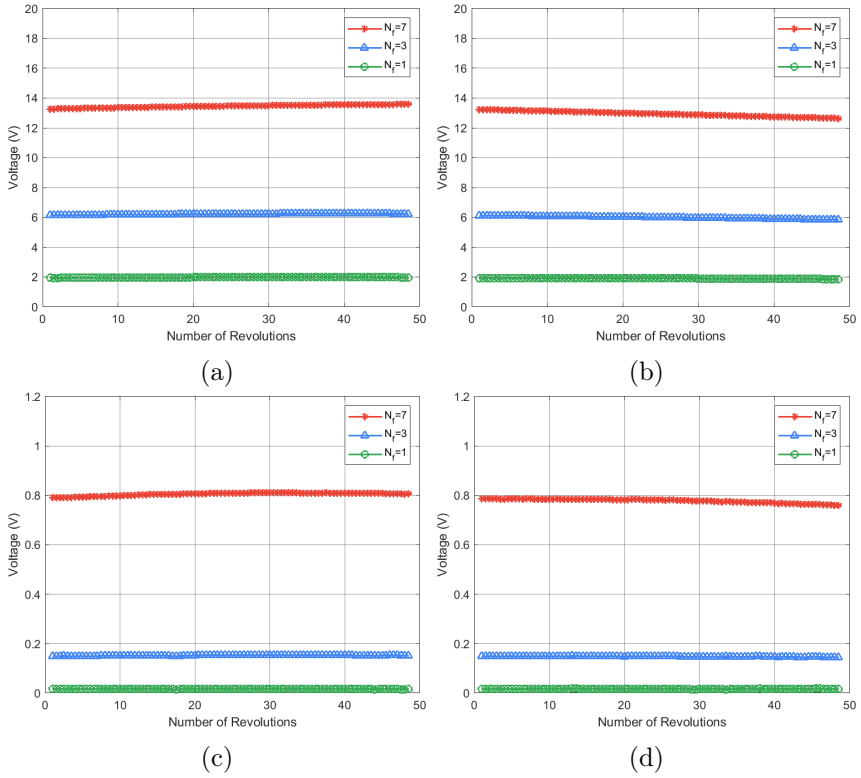

Figure 4.11: Amplitude variation of $\underline{u}^{-}_{\alpha\beta}$ in load torque varying conditions with 100% of the rated speed: (a) Motor with $R_f = 1\ m\Omega$; (b) Generator with $R_f = 1\ m\Omega$; (c) Motor with $R_f = 1\ \Omega$; (d) Generator with $R_f = 1\ \Omega$;

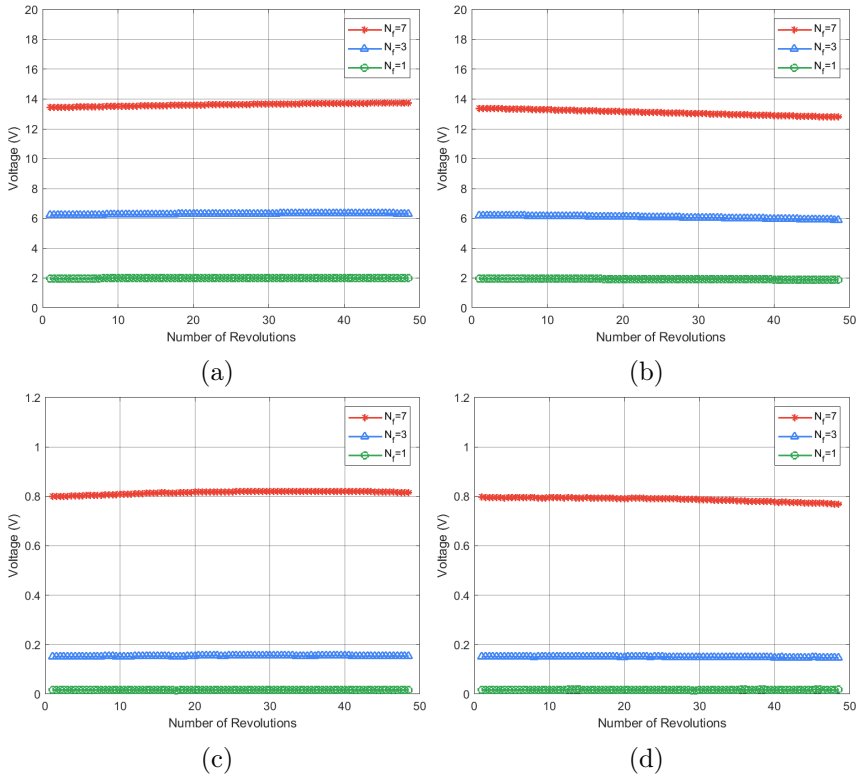

Figure 4.12: Amplitude variation of $\underline{e}^{-}_{\alpha\beta}$ for load torque varying conditions with 100% of the rated speed: (a) Motor with $R_f = 1\ m\Omega$; (b) Generator with $R_f = 1\ m\Omega$; (c) Motor with $R_f = 1\ \Omega$; (d) Generator with $R_f = 1\ \Omega$;

Phases

By examining Fig. 4.13 and Fig. 4.14, it becomes evident that the load torque variation has a big impact on the phase of the fault indicators $\underline{u}^{-}_{\alpha\beta}$ and $\underline{e}^{-}_{\alpha\beta}$. Evaluating the phase variation in the incipient fault scenario and comparing this variation with the dead short-circuit scenario, it can be inferred that the same saturation effect is present in load torque varying conditions. Was it not for this effect and the phase variations would overlap, independently of the number of short-circuited turns, as it happens for the incipient fault scenario. Even with the saturation effect in mind and the vertical shift of the phases caused by it, the overall phase variation in the dead short-circuit scenario is $\approx 30°$, which is still inside the set limit of 60°. When it comes to the incipient fault scenario, and since the saturation is still non-existent, the phase variation is half of the dead short-circuit scenario: $\approx 15°$ for both motor and generator modes of operation. Again the one short-circuited turn with $R_f = 1\ \Omega$ is so slight that its information cannot be accurately picked up. Since the load torque variation has a big effect on the phase information the oscillations become more noticeable.

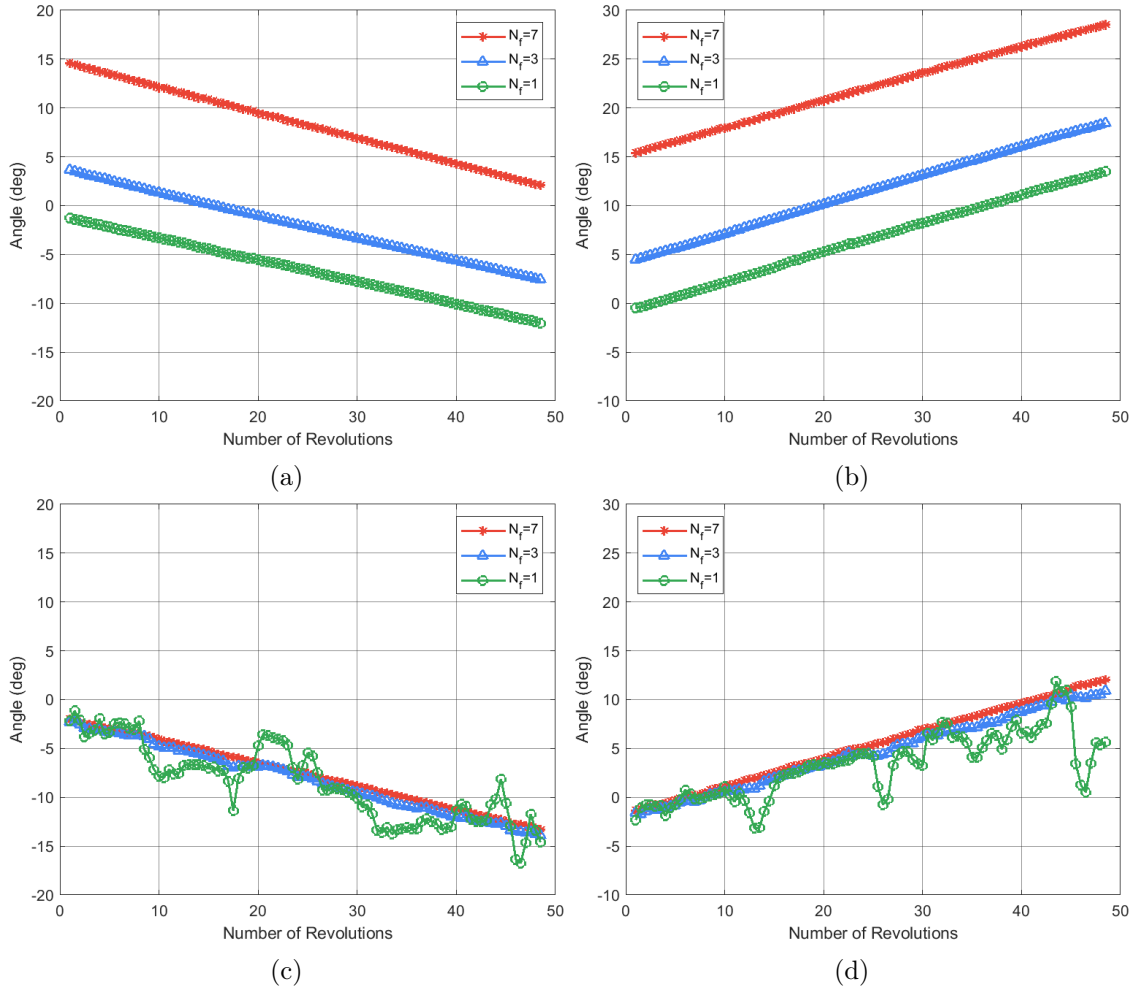

Figure 4.13: Phase variation of $\underline{u}^{-}_{\alpha\beta}$ for load torque varying conditions with 100% of the rated speed: (a) Motor with $R_f = 1\ m\Omega$; (b) Generator with $R_f = 1\ m\Omega$; (c) Motor with $R_f = 1\ \Omega$; (d) Generator with $R_f = 1\ \Omega$;

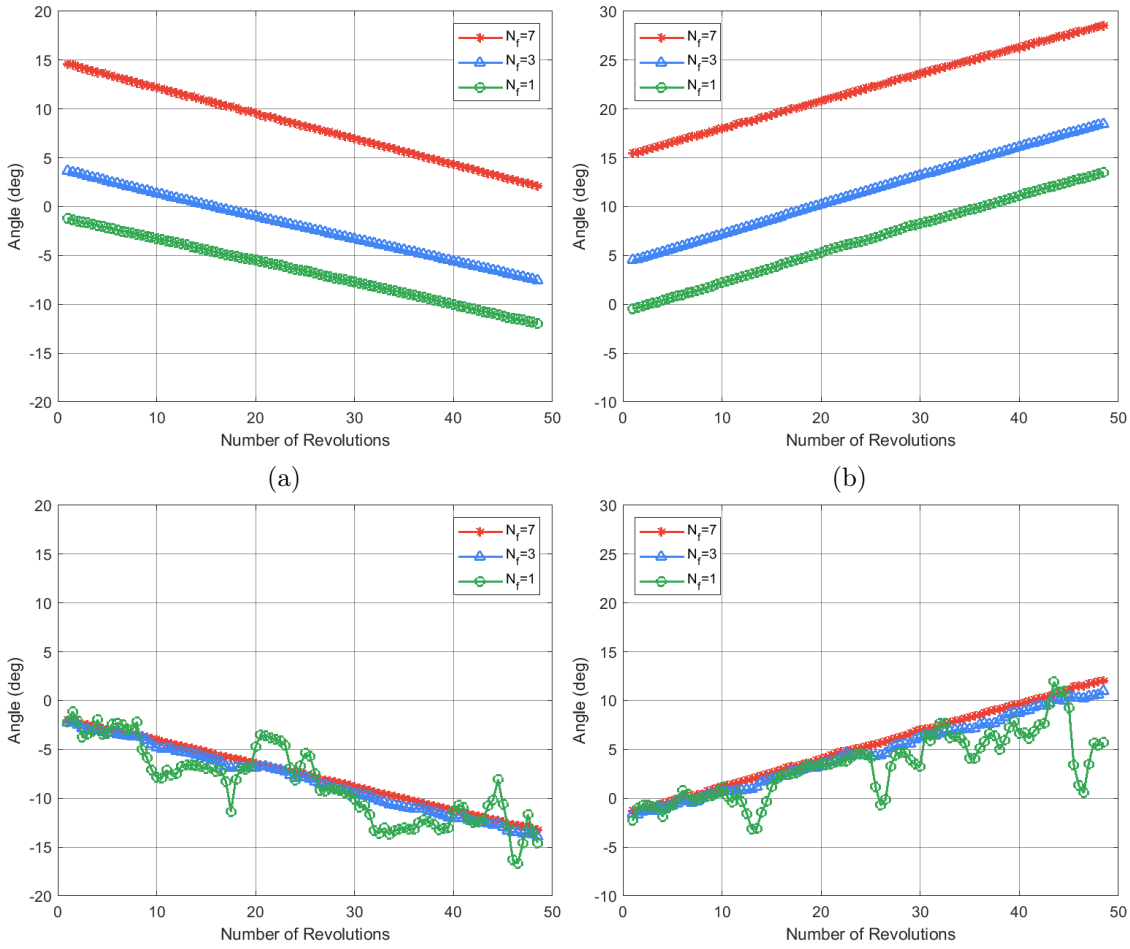

Figure 4.14: Phase variation of $\underline{e}^{-}_{\alpha\beta}$ for load torque varying conditions with 100% of the rated speed: (a) Motor with $R_f = 1\ m\Omega$; (b) Generator with $R_f = 1\ m\Omega$; (c) Motor with $R_f = 1\ \Omega$; (d) Generator with $R_f = 1\ \Omega$;

Fault Severity

The fault severity illustrated in Fig. 4.15 and Fig. 4.16, aligns with the observations made in the speed variation study, that is, the fault severity, which is quantified by the fault severity index, closely relates to the amplitude variation of the fault indicators.

The fault severity index provides a measure of the severity of the ITSC fault in the stator, and as the fault indicators amplitudes increase, indicating the presence of a more significant fault, the fault severity index reflects this heightened severity. In this load torque variation study, where the frequency does not change, the amplitude variation of the fault indicators remained negligible, and consequently, the fault severity index exhibited a similar behaviour, showing a minimal variation. This validates the assessment of the ITSC severity when load torque variations occur without substantial frequency changes.

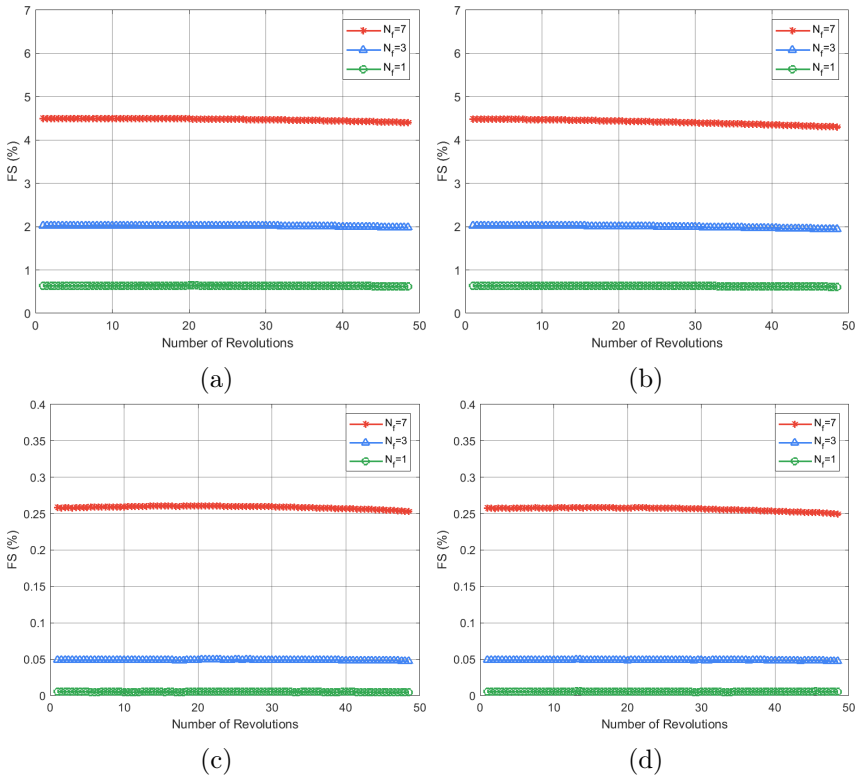

Figure 4.15: Fault severity variation of $\underline{u}^{-}_{\alpha\beta}$ for load torque varying conditions with 100% of the rated speed: (a) Motor with $R_f = 1\ m\Omega$; (b) Generator with $R_f = 1\ m\Omega$; (c) Motor with $R_f = 1\ \Omega$; (d) Generator with $R_f = 1\ \Omega$;

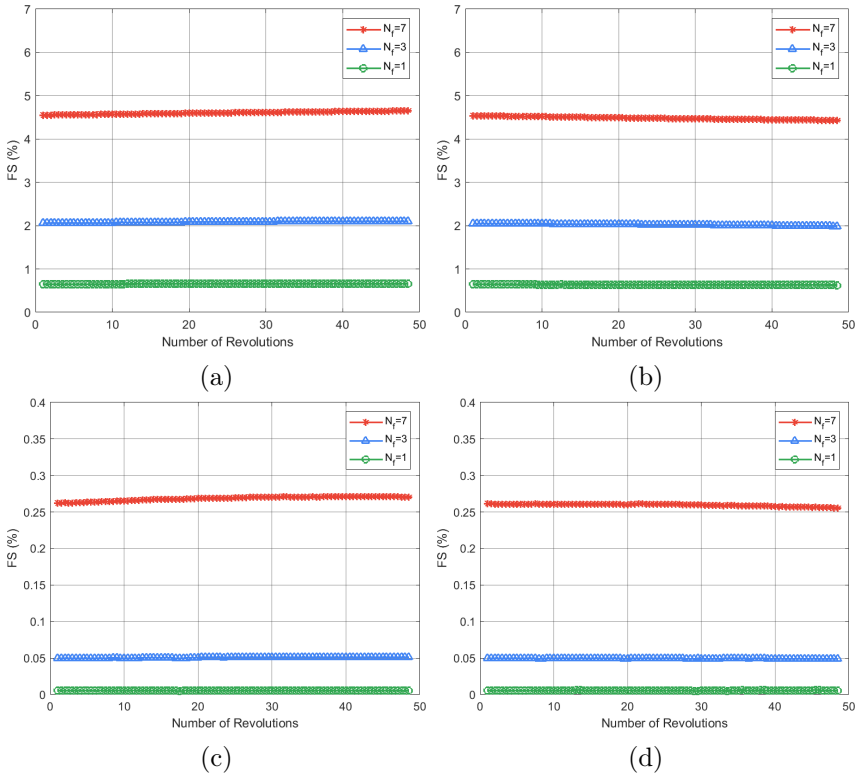

Figure 4.16: Fault severity variation of $\underline{e}^{-}_{\alpha\beta}$ for load torque varying conditions with 100% of the rated speed: (a) Motor with $R_f = 1\ m\Omega$; (b) Generator with $R_f = 1\ m\Omega$; (c) Motor with $R_f = 1\ \Omega$; (d) Generator with $R_f = 1\ \Omega$;

Normalised Fault Severity

It is also important to evaluate the effect of the load torque variation on the normalised fault severity index, as it should theoretically be independent of the load level. From Fig. 4.17 and Fig. 4.18 it can be established that the normalised fault severity is in fact independent of the load level.

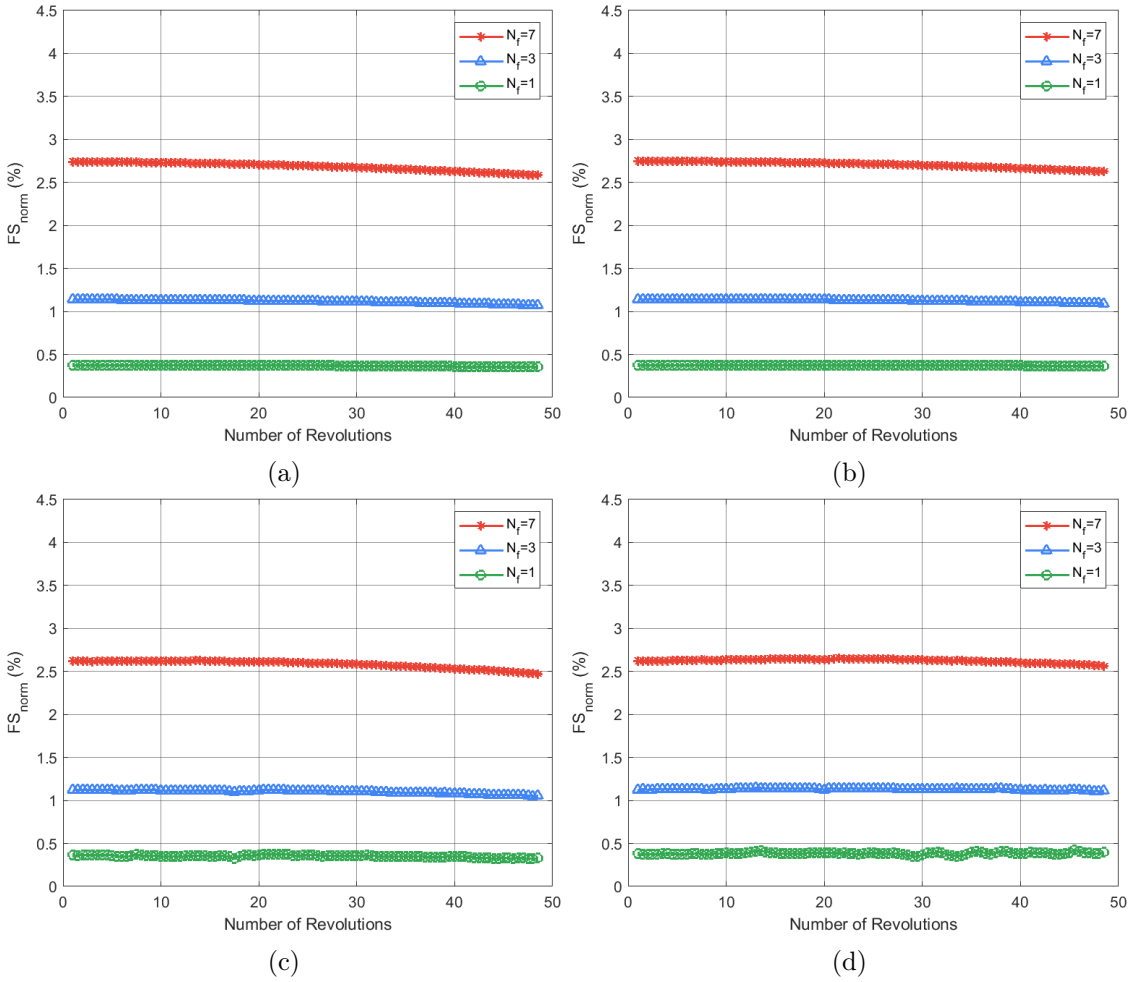

Figure 4.17: Normalised fault severity of $\underline{u}^{-}_{\alpha\beta}$ for load torque varying conditions: (a) Motor with $R_f = 1\ m\Omega$; (b) Generator with $R_f = 1\ m\Omega$; (c) Motor with $R_f = 1\ \Omega$; (d) Generator with $R_f = 1\ \Omega$;

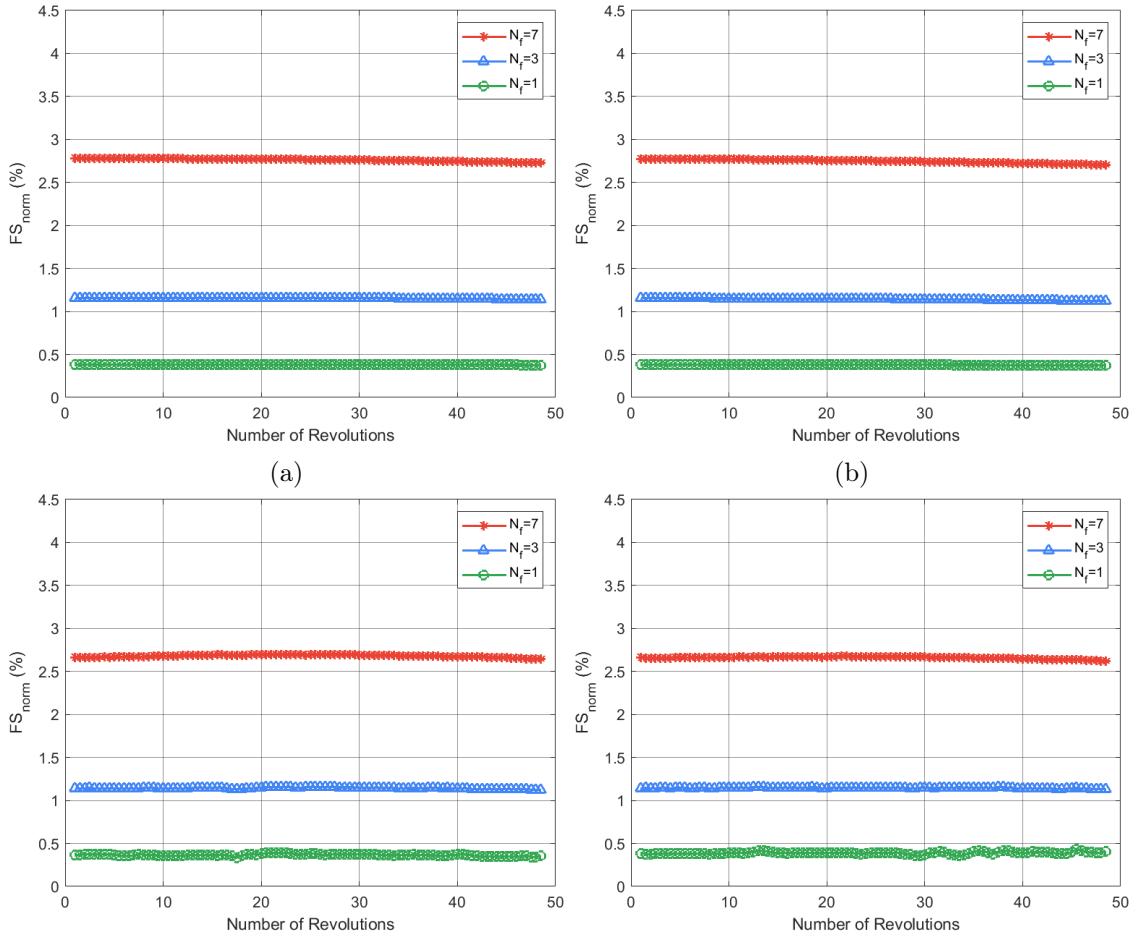

Figure 4.18: Normalised fault severity of $\underline{u}^{-}_{\alpha\beta}$ for load torque varying conditions: (a) Motor with $R_f = 1\ m\Omega$; (b) Generator with $R_f = 1\ m\Omega$; (c) Motor with $R_f = 1\ \Omega$; (d) Generator with $R_f = 1\ \Omega$;

4.1.3 Combined Speed and Load Torque Variation

In this section both speed and load are varied over time. The speed variation chosen was an acceleration from 0 to 1500 rpm and then a deceleration back to 0 rpm, all in the same 2 second time period. Meanwhile i^*_{qs} is varying from no-load to 100% rated load at a frequency higher than the speed variation, allowing to clearly see the effects of a repetitive load variation while the machine is accelerating and again while it is decelerating.

The rotor speed, rotor position, fault currents and electromagnetic torque results from this combined speed and load variation study are illustrated in Fig. 4.19.

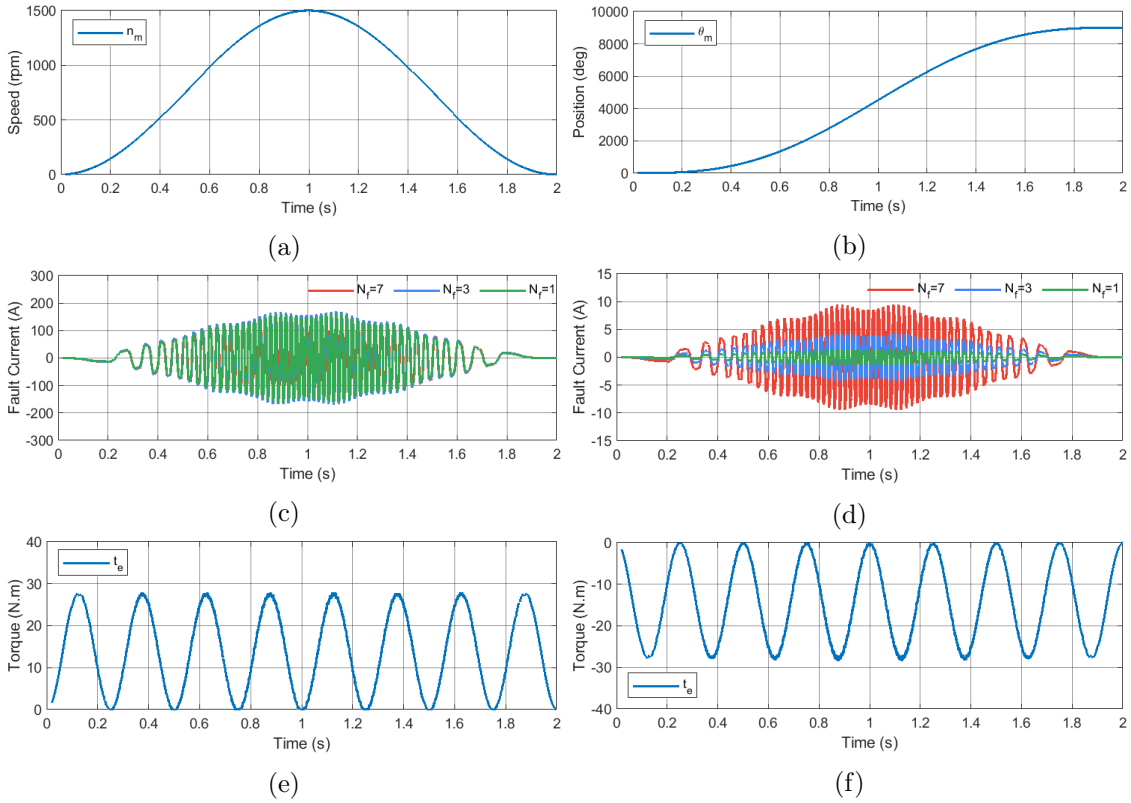

Figure 4.19: Computational results for the combined speed and load torque varying conditions: (a) Rotor Speed; (b) Rotor Position; (c) Fault Currents ($R_f = 1\ mOhm$); (d) Fault Currents ($R_f = 1\ Ohm$); (e) Electromagnetic Torque (Motor); (f) Electromagnetic Torque (Generator)

Amplitudes

Fig. 4.20 and 4.21 corroborate the conclusions presented in the speed varying and in the load torque varying sections of this work, with regard to amplitudes, where the speed variation primarily affected the amplitude of the fault indicator $\underline{u}^{-}_{\alpha\beta}$ and $\underline{e}^{-}_{\alpha\beta}$, while the load variation did not make much of an impact. As such, the behaviour of the machine can clearly be seen through the variation of the amplitude: an acceleration in the first second and a deceleration in the last second.

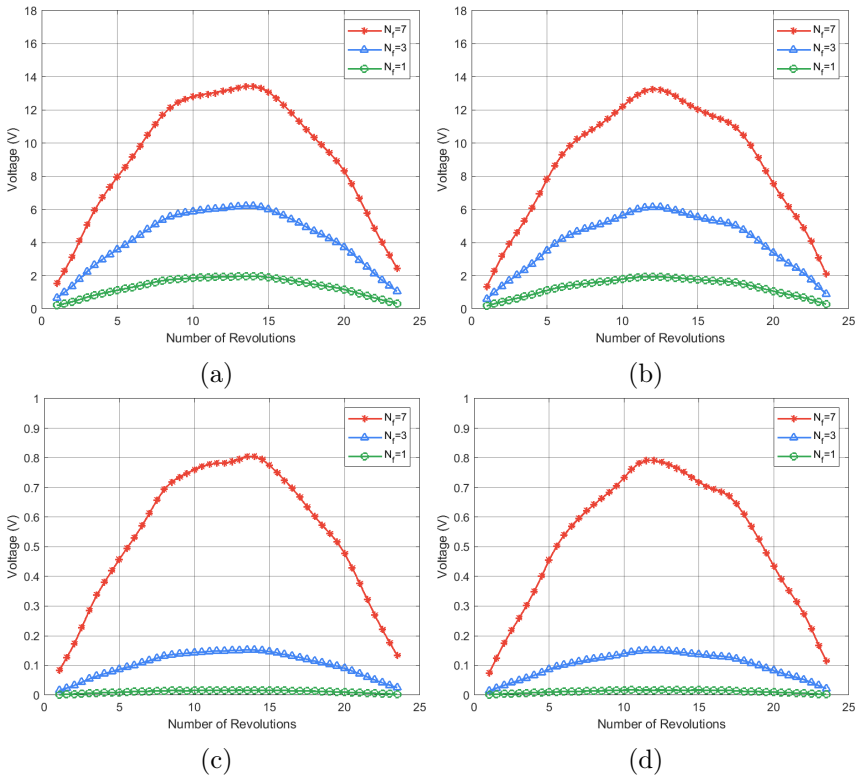

Figure 4.20: Amplitude variation of $\underline{u}^{-}_{\alpha\beta}$ for varying speed and load conditions: (a) Motor with $R_f = 1\ m\Omega$; (b) Generator with $R_f = 1\ m\Omega$; (c) Motor with $R_f = 1\ \Omega$; (d) Generator with $R_f = 1\ \Omega$;

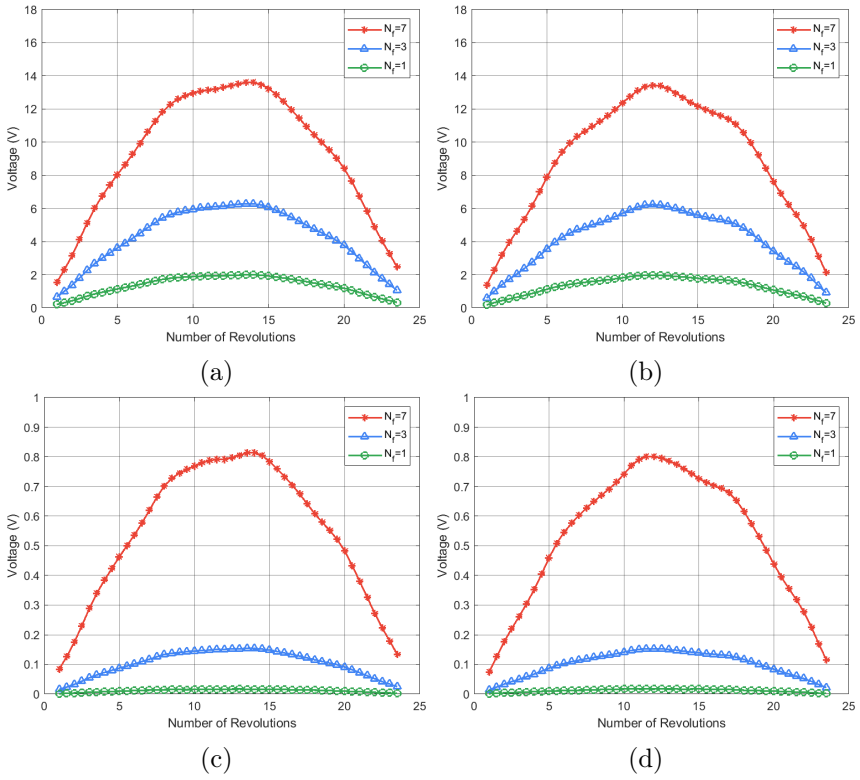

Figure 4.21: Amplitude variation of $\underline{e}^{-}_{\alpha\beta}$ for combined speed and load torque varying conditions: (a) Motor with $R_f = 1\ m\Omega$; (b) Generator with $R_f = 1\ m\Omega$; (c) Motor with $R_f = 1\ \Omega$; (d) Generator with $R_f = 1\ \Omega$;

Phases

Unlike the amplitudes, both the speed variation and load variation had effects on the phase variation of the fault component. The combined speed and load torque variation effect on the phases of $\underline{u}^{-}_{\alpha\beta}$ and $\underline{e}^{-}_{\alpha\beta}$ are shown. These results are consistent with the expected behaviour, being that the load variation has a much bigger impact on the phases of the fault indexes than the amplitude variation. In this case, the load-varying behaviour of the machine can clearly be seen through the phase-variation. Again, the saturation effect is visible for the dead short-circuit scenario, where the higher the number of short-circuited turns is, the higher their vertical shift will be in the phase variation curves.

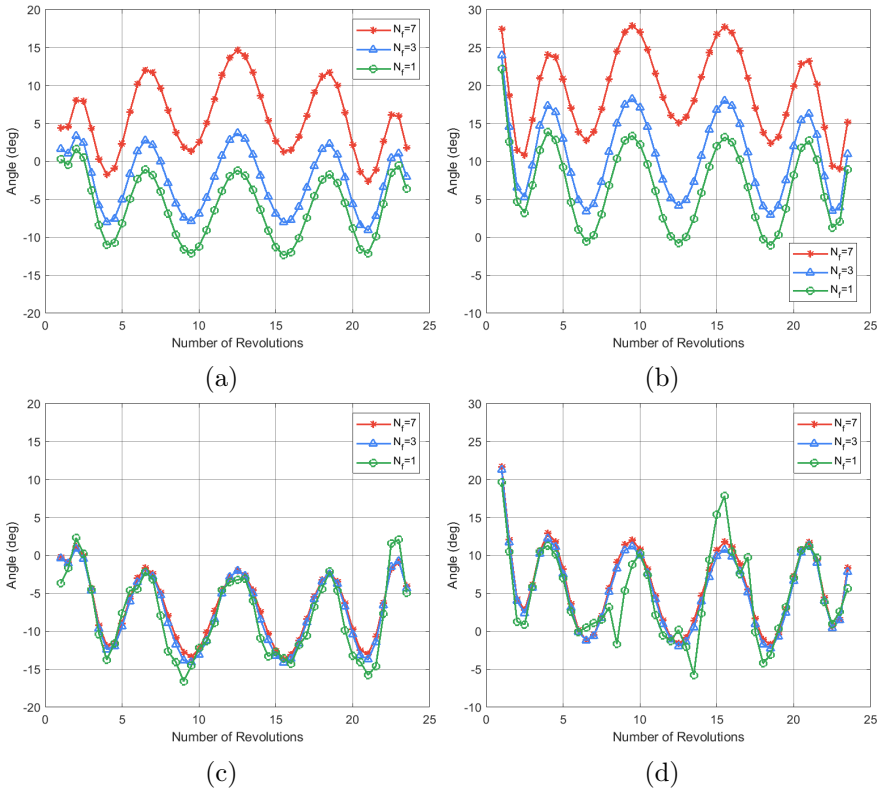

Figure 4.22: Load variation of $\underline{u}^{-}_{\alpha\beta}$ for varying speed and load conditions: (a) Motor with $R_f = 1\ m\Omega$; (b) Generator with $R_f = 1\ m\Omega$; (c) Motor with $R_f = 1\ \Omega$; (d) Generator with $R_f = 1\ \Omega$;

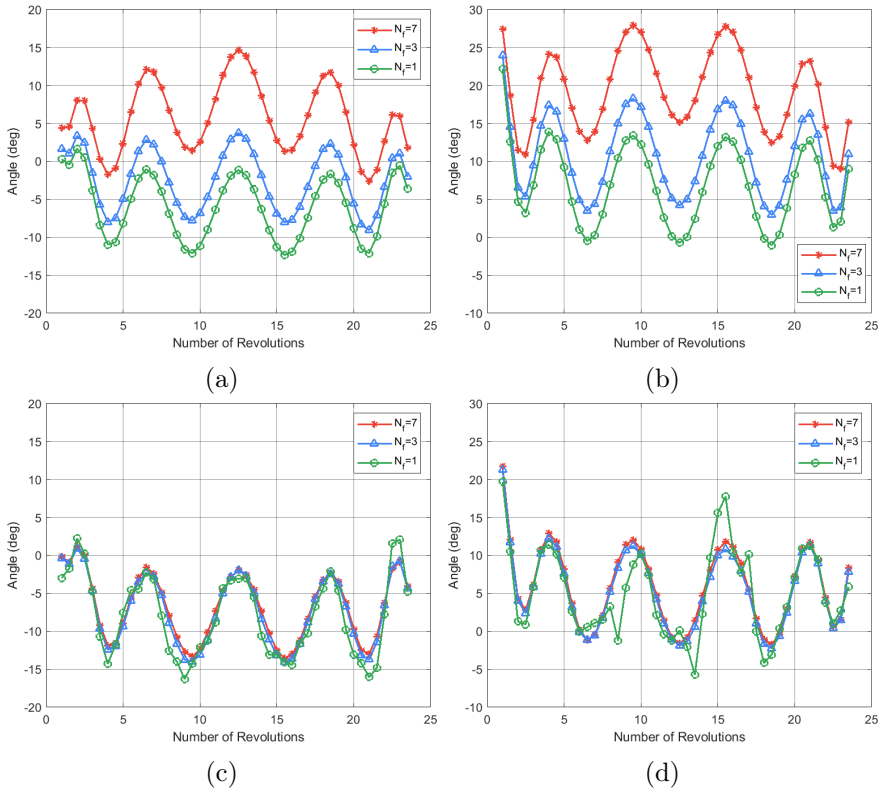

Figure 4.23: Phase variation of $\underline{e}^{-}_{\alpha\beta}$ in combined speed and load torque varying conditions: (a) Motor with $R_f = 1\ m\Omega$; (b) Generator with $R_f = 1\ m\Omega$; (c) Motor with $R_f = 1\ \Omega$; (d) Generator with $R_f = 1\ \Omega$;

Fault Severity

The fault severity variation for the speed and load variations is illustrated in Fig. 4.24 and Fig. 4.25 for both $\underline{u}^{-}_{\alpha\beta}$ and $\underline{e}^{-}_{\alpha\beta}$. The fault severity is dependent of the amplitude variation, and since there is a speed variation (frequency variation) the fault severity curves behaviour will follow the frequency variation behaviour as well.

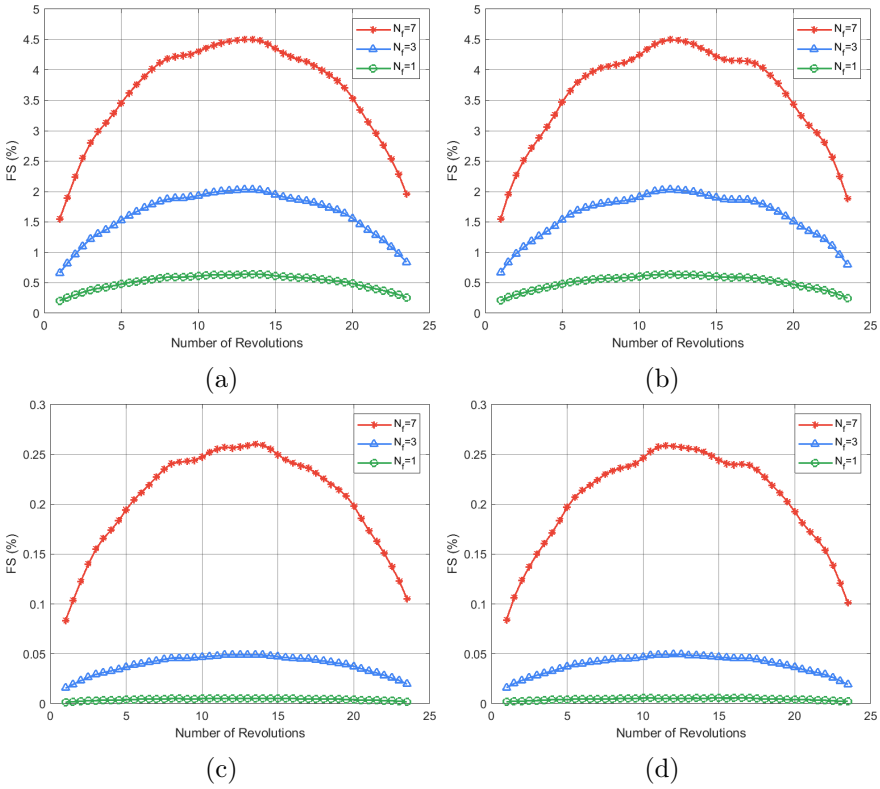

Figure 4.24: Fault severity variation of $\underline{u}^{-}_{\alpha\beta}$ in varying speed and load conditions: (a) Motor with $R_f = 1\ m\Omega$; (b) Generator with $R_f = 1\ m\Omega$; (c) Motor with $R_f = 1\ \Omega$; (d) Generator with $R_f = 1\ \Omega$;

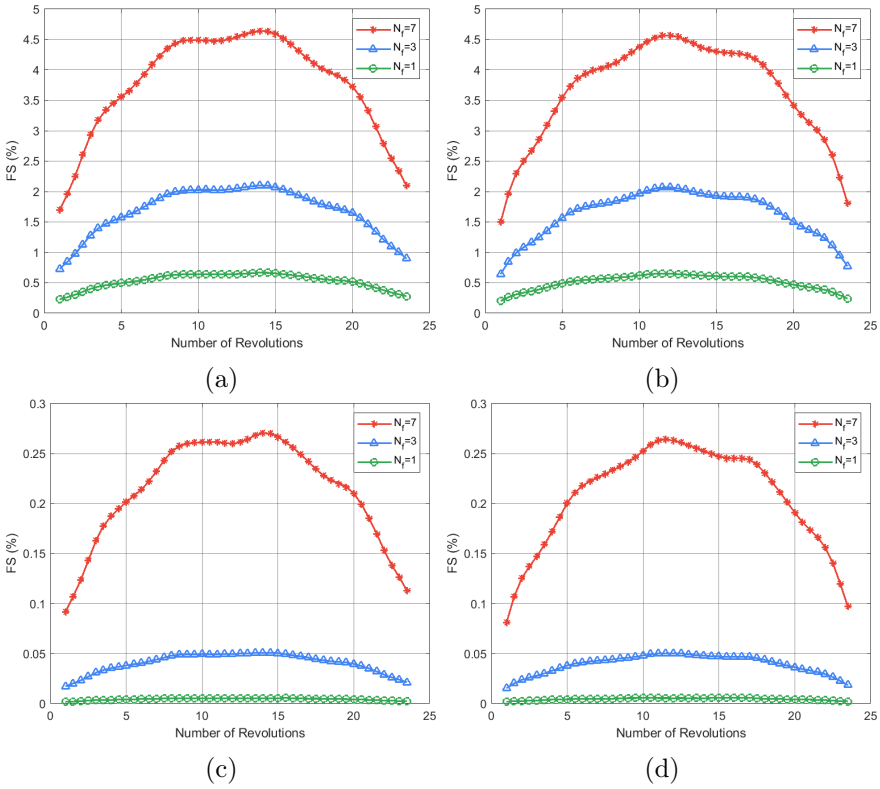

Figure 4.25: Fault severity variation of $\underline{e}^{-}_{\alpha\beta}$ in combined speed and load torque varying conditions: (a) Motor with $R_f = 1\ m\Omega$; (b) Generator with $R_f = 1\ m\Omega$; (c) Motor with $R_f = 1\ \Omega$; (d) Generator with $R_f = 1\ \Omega$;

Normalised Fault Severity

In the load torque variation section, the effects of the load variation in the normalised fault severity index were as expected, that is, that the index is independent of the load level. However, in this combined speed and vector variation, where the load variation is much more repetitive in a single acceleration/deceleration, it is noticeable, in Fig. 4.26 and Fig. 4.27, an oscillation of this index, that runs at the same frequency of the load torque variations. This shows that this fault severity index is not so independent from sharp load variations. Lastly, it can be seen from the plotted data that the $\underline{e}^{-}_{\alpha\beta}$ seems more independent of load variations since its oscillations are smaller when compared with the ones present in $\underline{u}^{-}_{\alpha\beta}$.

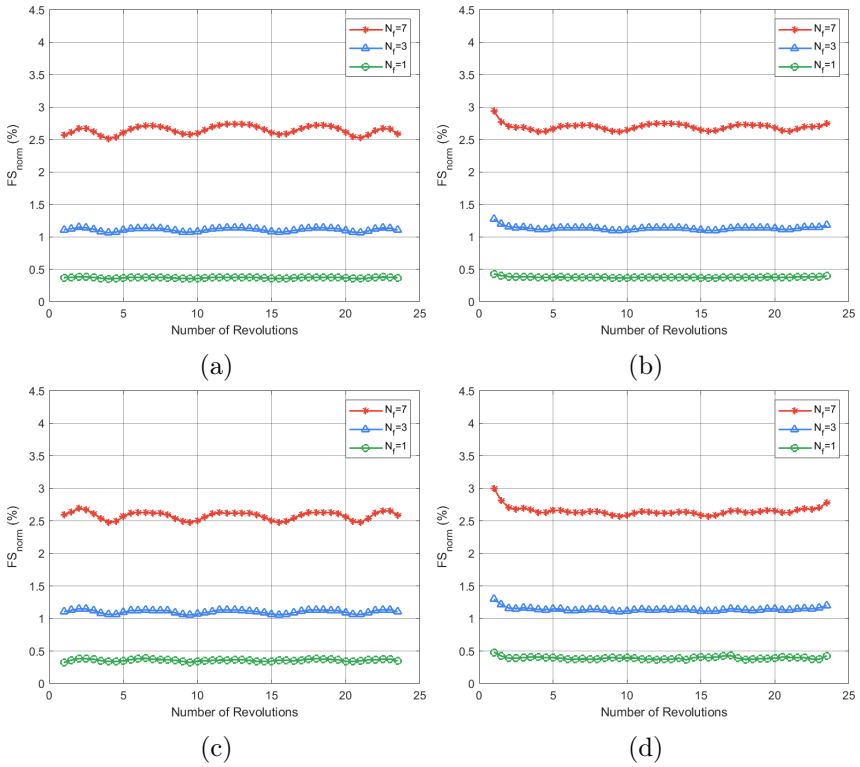

Figure 4.26: Normalised fault severity of $\underline{u}^{-}_{\alpha\beta}$ in speed varying conditions in three different fault situations and two modes of operation: (a) Motor with $R_f = 1\ m\Omega$; (b) Generator with $R_f = 1\ m\Omega$; (c) Motor with $R_f = 1\ \Omega$; (d) Generator with $R_f = 1\ \Omega$;

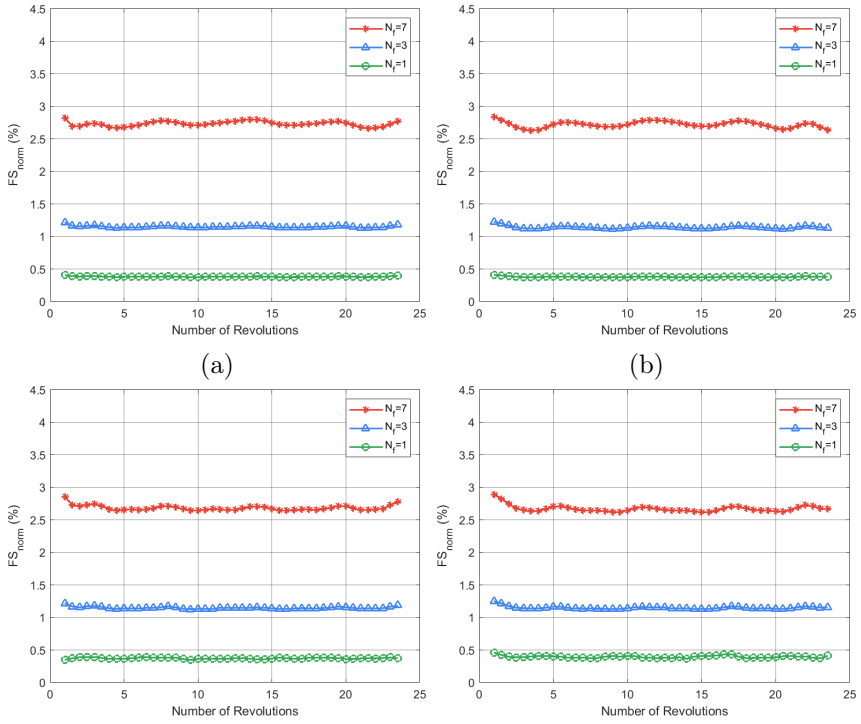

Figure 4.27: Normalised fault severity of $\underline{e}^{-}_{\alpha\beta}$ in speed varying conditions: (a) Motor with $R_f = 1\ m\Omega$; (b) Generator with $R_f = 1\ m\Omega$; (c) Motor with $R_f = 1\ \Omega$; (d) Generator with $R_f = 1\ \Omega$;

Chapter 5

Experimental Results

In the simulation stage it was possible to make the fault resistance as small as 1 $m\Omega$ but in the experimental tests a dead short-circuit would probably permanently damage the machine. Therefore, at this stage, only an incipient short-circuit was studied. Nonetheless, to better analyse the fault under the different numbers of shorted-turns, the fault resistance used was varied according to the number of short-circuited turns. To safeguard the insulation system, a limit was imposed on the fault current magnitude i_f. This limit was arbitrarily chosen as approximately 15 A (measured at 1400 rpm). The different fault resistance values used for each number of short-circuited turns is presented in Table 5.1. Since in Chapter 4 the one-turn short-circuit in an incipient short-circuit scenario was barely detectable, a fourth fault situation was added where two turns are short-circuited. Fig. 5.1 shows a detail on the possible connections for one coil (of 8) of the winding phase.

Figure 5.1: Schematic of the stator winding connections that enables the short-circuit between turns.

Although the rheostat was set to 0% in both the one and two short-circuited turns cases, the actual resistance is never zero, as the resistances from the connecting cables must be accounted for. Nonetheless, the short-circuit current in these two cases did not reach the 15 A limit.

Table 5.1: Fault resistance values used for each number of short-circuited turns.

N_f	R_f (Ω)	I_f (A)
7	0.5	15
3	0.2	15
2	0	14
1	0	7

The proposed methods were validated experimentally in a 4-kW 6-PMSM drive under different operating conditions. The parameters of the 6-PMSM are listed in Table B.1 of Appendix B along with an illustration of the experimental setup.

Before the analysis of the experimental results, an observation needs to be made. In the real world, an electrical machine is never perfectly symmetric. Manufacturing imperfections, rotor eccentricity or a deviation in the stator winding distribution are among the

reasons that can cause a residual asymmetry. As a consequence, when analysing a normal (healthy) signal the information regarding the residual asymmetry will be present. Taking this into consideration, to get the actual fault information, a vector subtraction is made, where the acquired signal (under fault conditions), with some degree of asymmetry in it, will be subtracted by the "healthy" signal, that is, the signal under normal conditions that contains a residual asymmetry. By doing this, the residual asymmetry is effectively removed from the faulty signal and the actual fault information is obtained.

In Fig. 5.2 this effect, along with the vector subtraction result, is illustrated.

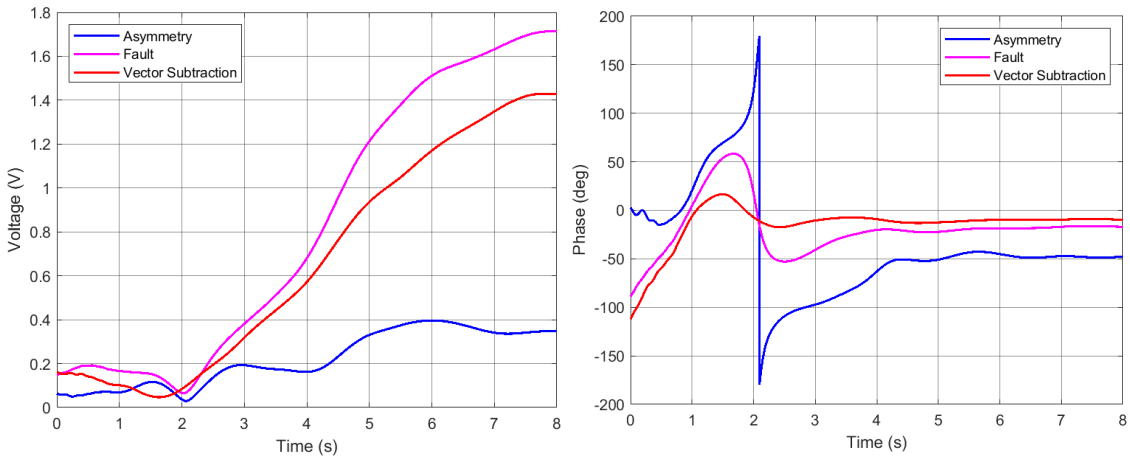

(a) (b)

Figure 5.2: Fault, asymmetry and vector subtraction when analysing the fault indexes: (a) Amplitudes; (b) Phases.

5.1 Offline Method

In this experimental stage, where noisy signals are expected, the window length has to be much higher than the one in the simulation stage, as to increase the frequency resolution. The selected value was empirically chosen as 2880 (8×360), making it possible to analyse speeds from 400 rpm upwards.

5.1.1 Speed Variation

In the speed variation studies, a remote speed controller (see Fig. B.2)(b) was used to make the accelerations for every fault scenario. These accelerations are similar to the accelerations made in the simulation stage, only now, instead of ramping the speed from 0 rpm to 1500 rpm in 2 seconds, this ramping will be done in 8 seconds. As for the simulation stage, the current references were set to $i^*_{qs} = 4.8$ A and $i^*_{ds} = i^*_{xs'} = i^*_{ys'} = 0$ A. The rotor speed, rotor position, fault currents and electromagnetic torque results from this study are illustrated in Fig. 5.3.

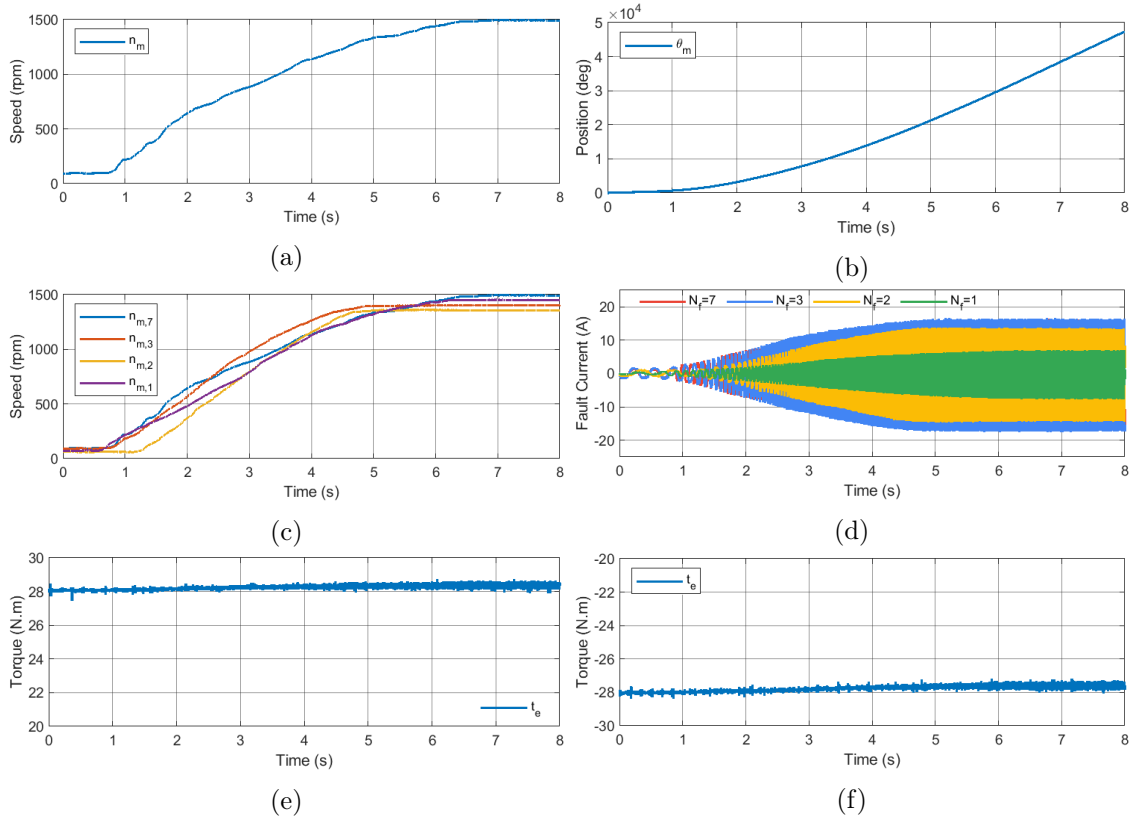

Figure 5.3: Computational results for speed varying conditions with 100% of the rated load: (a) Rotor Speed; (b) Rotor Position; (c) Rotor Speed for different numbers of short-circuited turns; (d) Fault Currents; (e) Electromagnetic Torque (Motor); (f) Electromagnetic Torque (Generator)

Amplitude

Fig. 5.4 and Fig. 5.5 show the result of the speed variation in the amplitudes of the fault indicators $\underline{u}^{-}_{\alpha\beta}$ and $\underline{e}^{-}_{\alpha\beta}$.

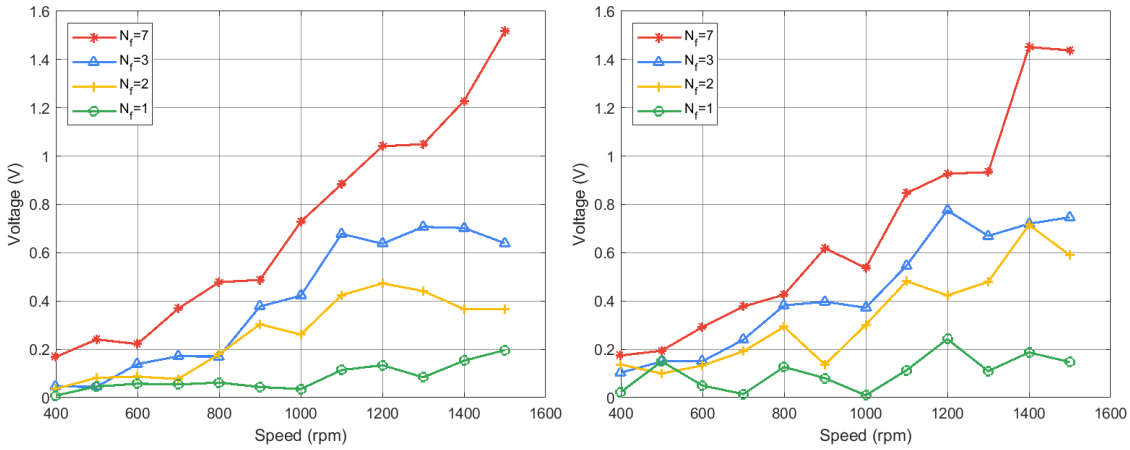

(a) (b)

Figure 5.4: Amplitude variation of $u^{-}_{\alpha\beta}$ in varying speed conditions: (a) Motor; (b) Generator.

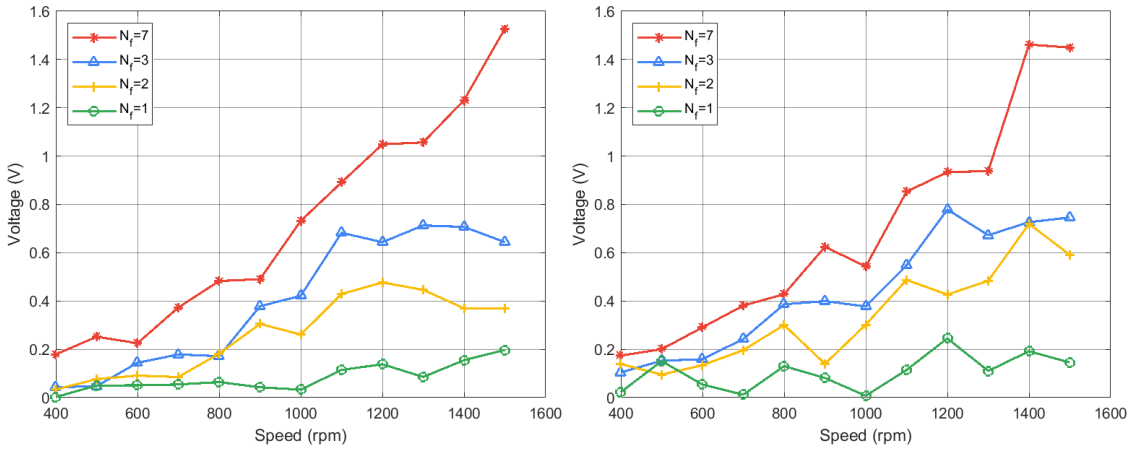

(a) (b)

Figure 5.5: Amplitude variation of $\underline{e}^{-}_{\alpha\beta}$ in varying speed conditions: (a) Motor; (b) Generator.

As expected from the simulation results in the amplitude of the fault indicator increases with the increase in speed.

Phase

In Fig. 5.6 and Fig. 5.7 it is shown the variation of the phases of $\underline{u}^{-}_{\alpha\beta}$ and $\underline{e}^{-}_{\alpha\beta}$ with speed. As expected, the one turn short-circuit is barely detectable and the accurate retrieval of the phase information has worsened. Its oscillations make the visualisation of the other short-circuits harder, but still it is possible to see that the phase variation for the 2, 3 and 7 shorted turns is inside a reasonable interval of 50° at speeds above 600 rpm and as such inside of our limitation to locate the fault (60°). In phase A1 the angle stabilises around $[-20°, 0°]$ in motor operation and $[0°, +20°]$ when operating as generator. With regard

to phase B1, the angle stabilises around the interval $[-130°, -120°]$ when functioning as a motor and around $-100°$ when working as a generator. Lastly, in phase A2, the angle stabilises at 50° and 80° for the operation as a motor and as generator respectively.

Figure 5.6: Phase variation of $\underline{u}^{-}_{\alpha\beta}$ in varying speed conditions: (a) Motor (A1); (b) Generator (A1); (c) Motor (B1); (d) Generator (B1); (e) Motor (A2); (f) Generator (A2).

Figure 5.7: Phase variation of $\underline{e}^{-}_{\alpha\beta}$ in varying speed conditions: (a) Motor (A1); (b) Generator (A1); (c) Motor (B1); (d) Generator (B1); (e) Motor (A2); (f) Generator (A2).

Fault Severity

In Fig. 5.8 and Fig. 5.9 the effects of speed variation in the fault severity of $\underline{u}^{-}_{\alpha\beta}$ and $\underline{e}^{-}_{\alpha\beta}$ are shown, respectively. Since the resistance values used were all different from 1 Ω the fault severity percentage will be different from the one obtained in Chapter 4. As can be seen by Fig. 5.8 and also Fig. 5.9 the fault percentage in this case was around 0.05 % which is 10 times smaller than what was accomplished in Chapter 4 with a R_f value of 1 $m\Omega$. Even though this fault severity percentage is equivalent to that of the three turn short-circuit with R_f being 1 Ω in the simulation stage, this fault is still difficult to measure. The amplitudes barely increase with the increase of speed and as seen by the phases, its variations are too unstable. In contrast, the biggest value used for R_f in this experimental step was 0.5 Ω in the seven turn short-circuit scenario, thus making the fault severity of the seven turns shorted higher than the fault severity seen in Chapter 4.

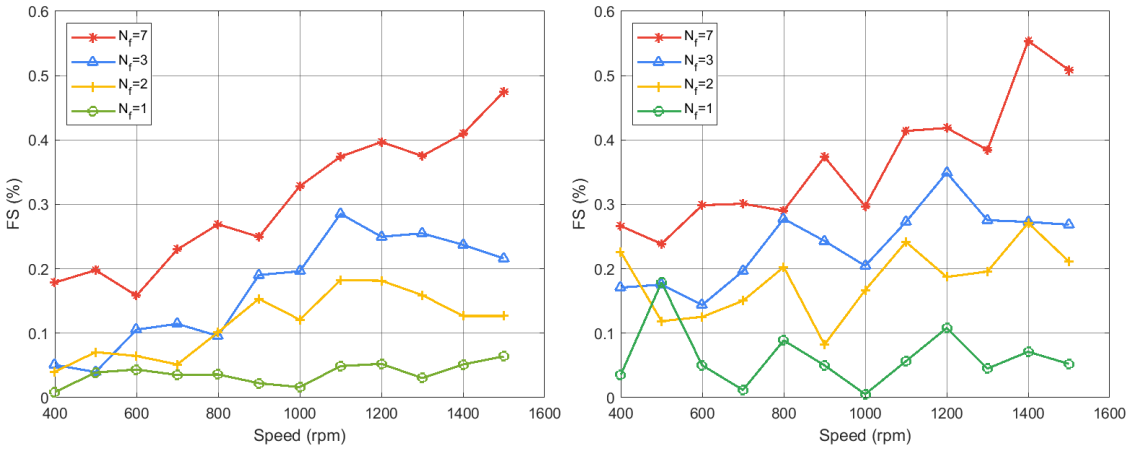

(a) (b)

Figure 5.8: Fault severity variation of $\underline{u}^{-}_{\alpha\beta}$ in varying speed conditions: (a) Motor; (b) Generator.

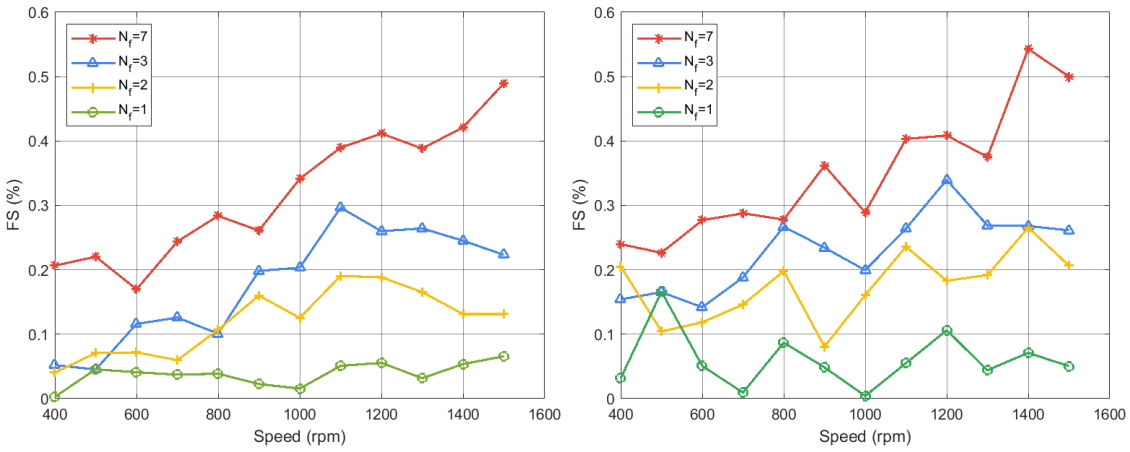

(a) (b)

Figure 5.9: Fault severity variation of $\underline{e}^{-}_{\alpha\beta}$ in varying speed conditions: (a) Motor; (b) Generator.

5.1.2 Load Variation

Amplitude

As seen from Fig. 5.10 and Fig. 5.11, and as expected from the results presented in the previous chapter, the load variation does not have a big effect on the amplitudes of $\underline{u}^{-}_{\alpha\beta}$ and $\underline{e}^{-}_{\alpha\beta}$, remaining mostly constant.

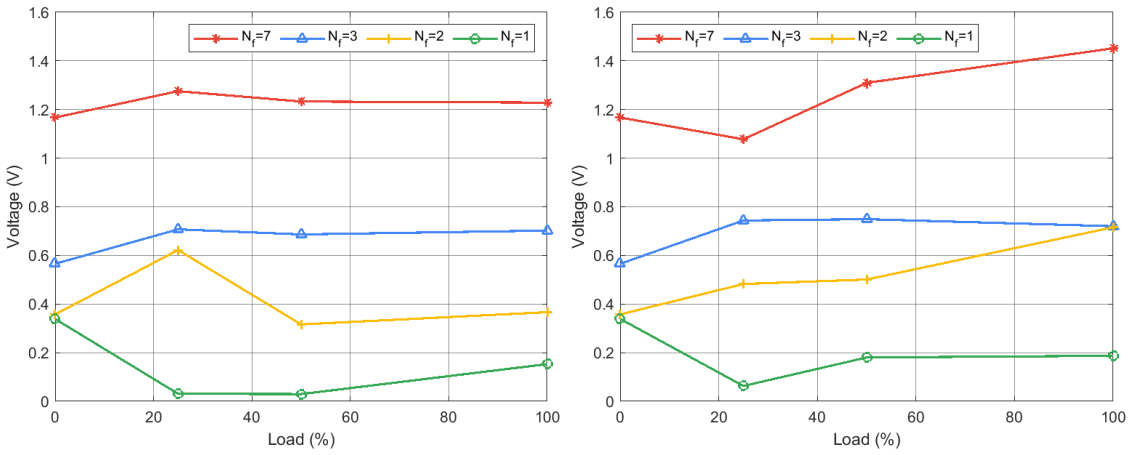

Figure 5.10: Amplitude variation of $\underline{u}^{-}_{\alpha\beta}$ in varying load conditions: (a) Motor; (b) Generator.

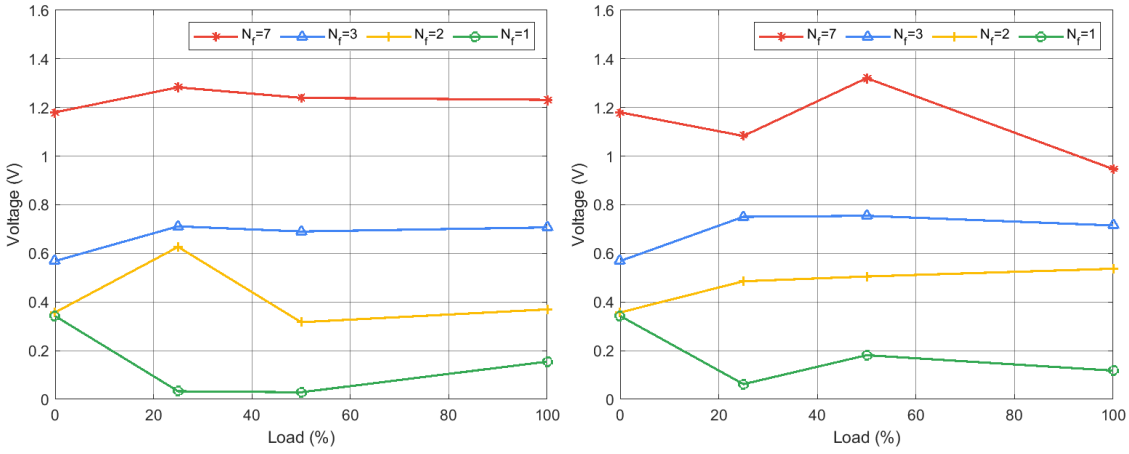

Figure 5.11: Amplitude variation of $\underline{e}^{-}_{\alpha\beta}$ in varying load conditions: (a) Motor; (b) Generator.

Phases

Fig. 5.12 and Fig. 5.13, show the phase variation for $\underline{u}^{-}_{\alpha\beta}$ and $\underline{e}^{-}_{\alpha\beta}$.

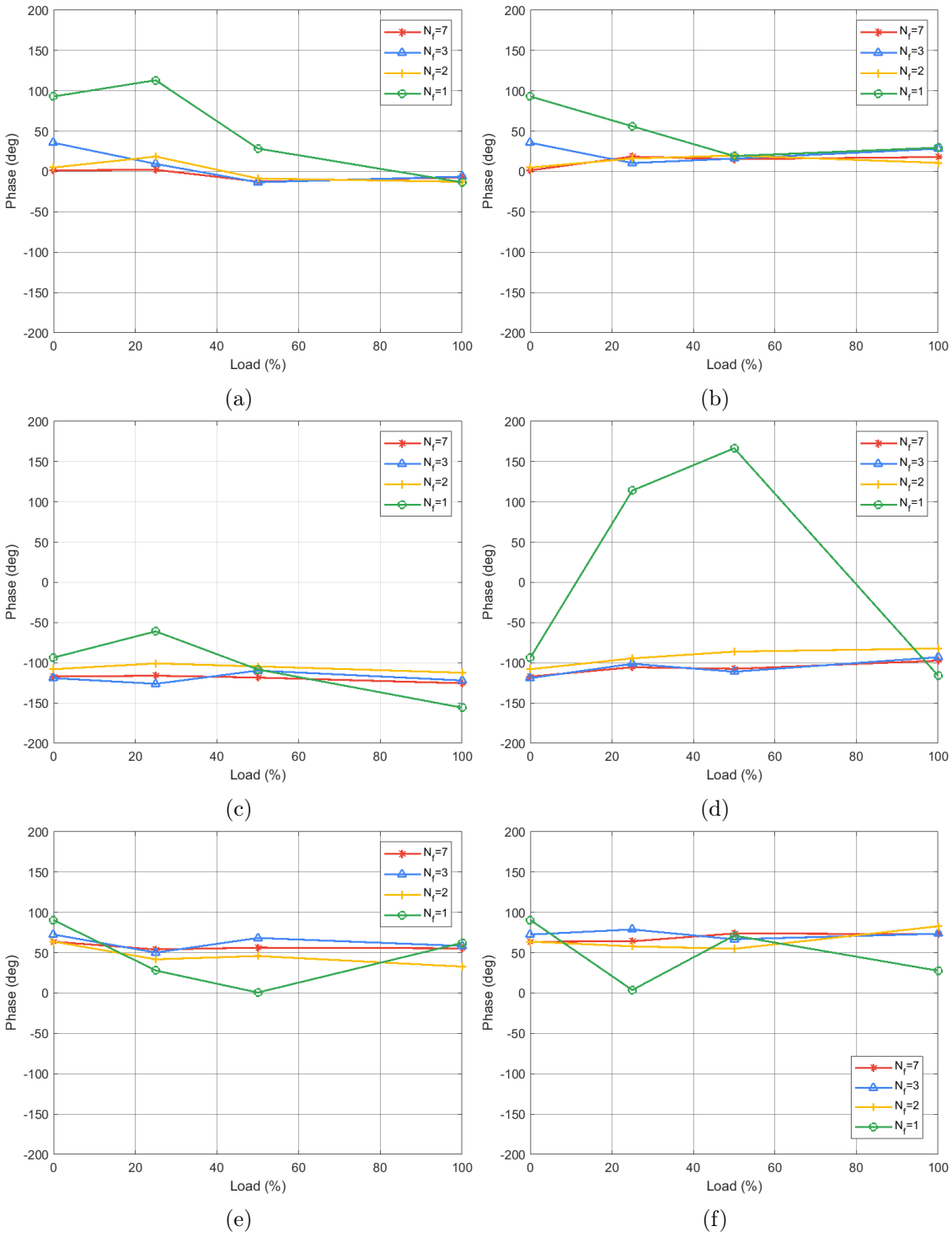

Figure 5.12: Phase variation of $\underline{u}^{-}_{\alpha\beta}$ in varying load conditions: (a) Motor (A1); (b) Generator (A1); (c) Motor (B1); (d) Generator (B1); (e) Motor (A2); (f) Generator (A2).

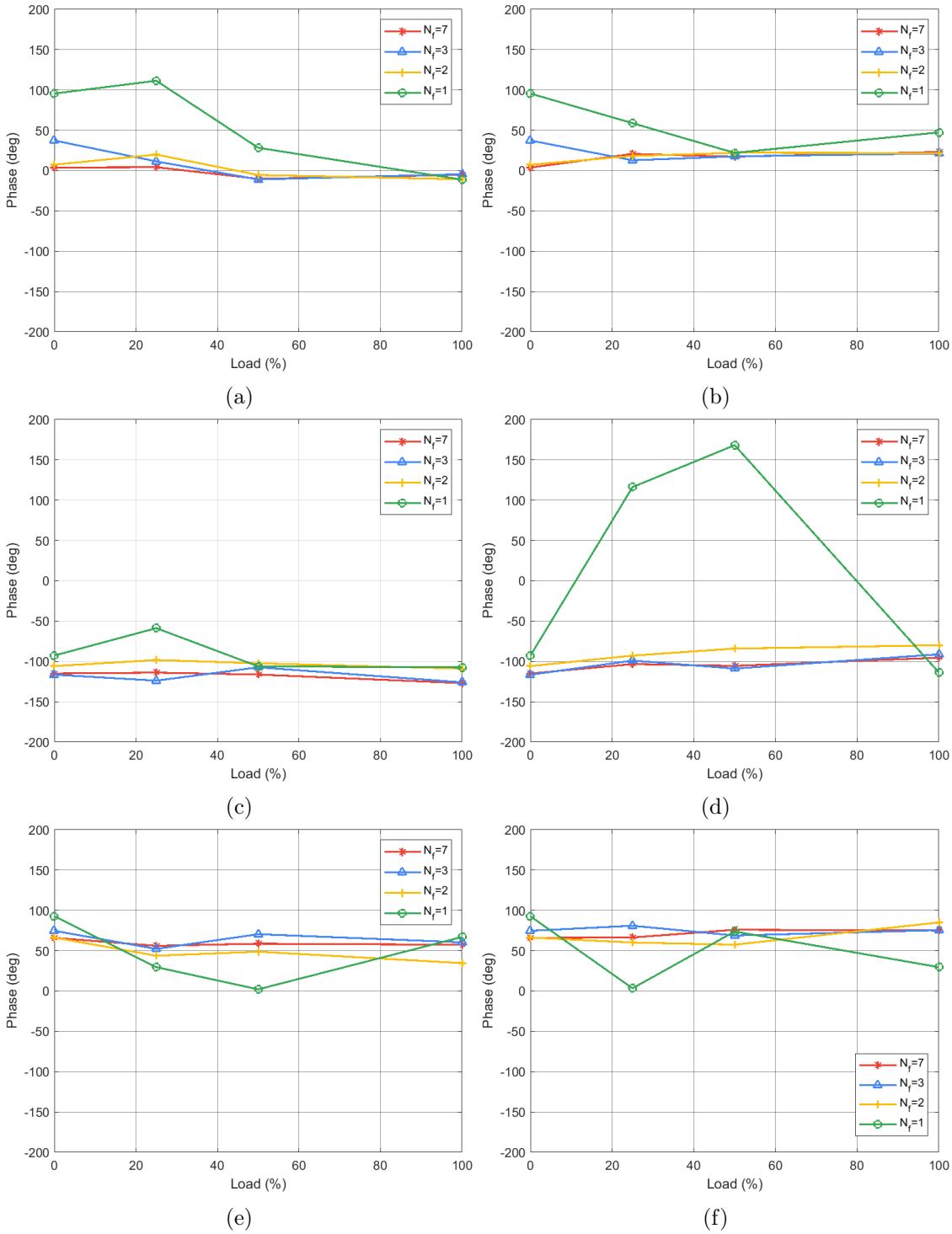

Figure 5.13: Phase variation of $\underline{e}^{-}_{\alpha\beta}$ in varying load conditions: (a) Motor (A1); (b) Generator (A1); (c) Motor (B1); (d) Generator (B1); (e) Motor (A2); (f) Generator (A2).

Overall, without taking into account the one-turn fault phase variation, the phases of $\underline{u}^{-}_{\alpha\beta}$ and $\underline{e}^{-}_{\alpha\beta}$ have a decrease of 20° when the machine is operating as a motor and an increase of 20° when operating as a generator.

Fault Severity

As expected from the amplitude variations, the fault severities of $\underline{u}^{-}_{\alpha\beta}$, in Fig. 5.14 and $\underline{e}^{-}_{\alpha\beta}$, in Fig. 5.15, are mostly constant.

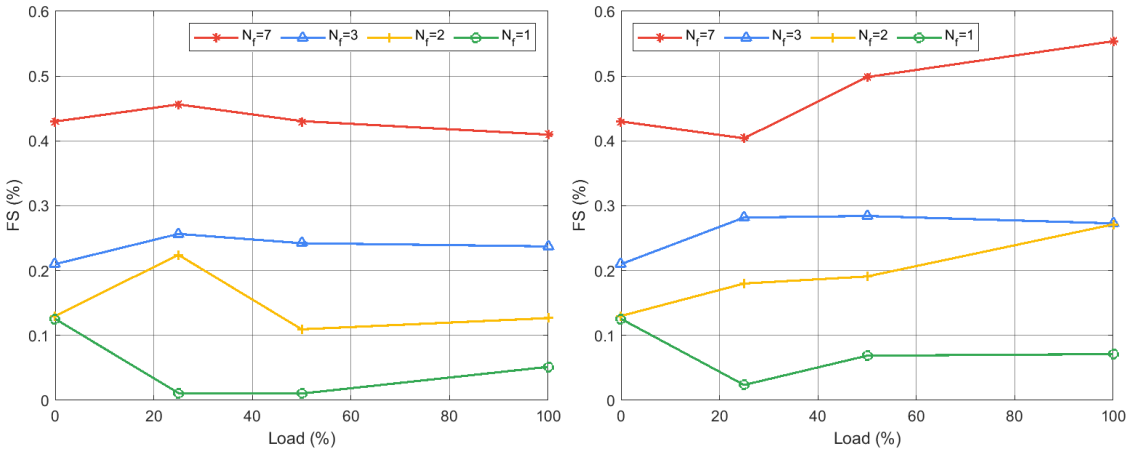

(a) (b)

Figure 5.14: Fault severity variation of $\underline{u}^{-}_{\alpha\beta}$ in varying load conditions: (a) Motor; (b) Generator.

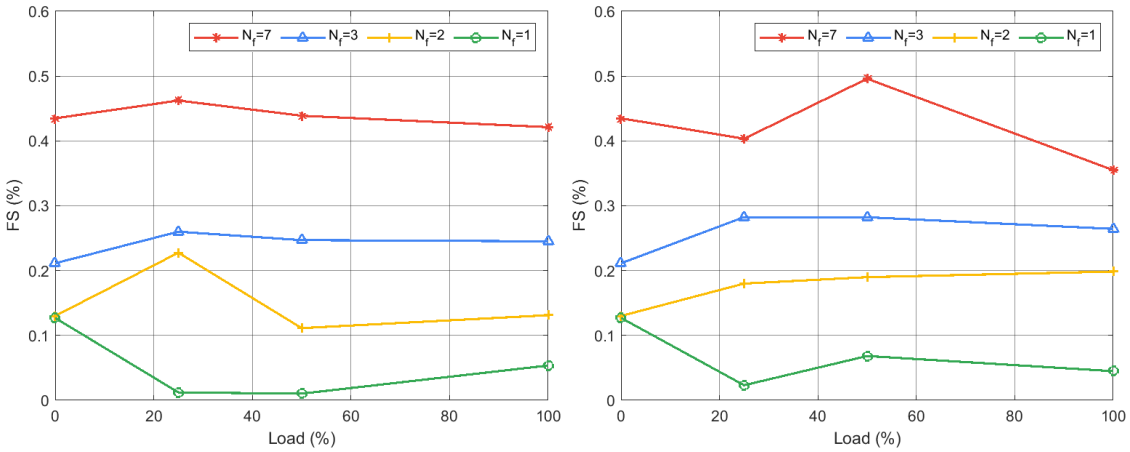

(a) (b)

Figure 5.15: Fault severity variation of $\underline{e}^{-}_{\alpha\beta}$ in varying load conditions: (a) Motor; (b) Generator.

5.2 Online Method

The same conditions applied to the offline method (STFT+SDT) method were use to validate this method. As stated in Chapter 3, the use of the MRF requires the tuning of the LPFs to remove the positive sequence components from the negative sequence ones. The filter used in this experimental stage was a fourth-order low-pass butterworth filter with a cutoff frequency, f_c, of 0.5 Hz.

5.2.1 Speed Variation

Amplitude

Fig. 5.16 and Fig. 5.17 showcase the effect of speed varying conditions in $\underline{u}^{-}_{\alpha\beta}$ and $\underline{e}^{-}_{\alpha\beta}$. Without having to deal with the windowing effect of the STFT the amplitude curves become much smoother than those of the previous method.

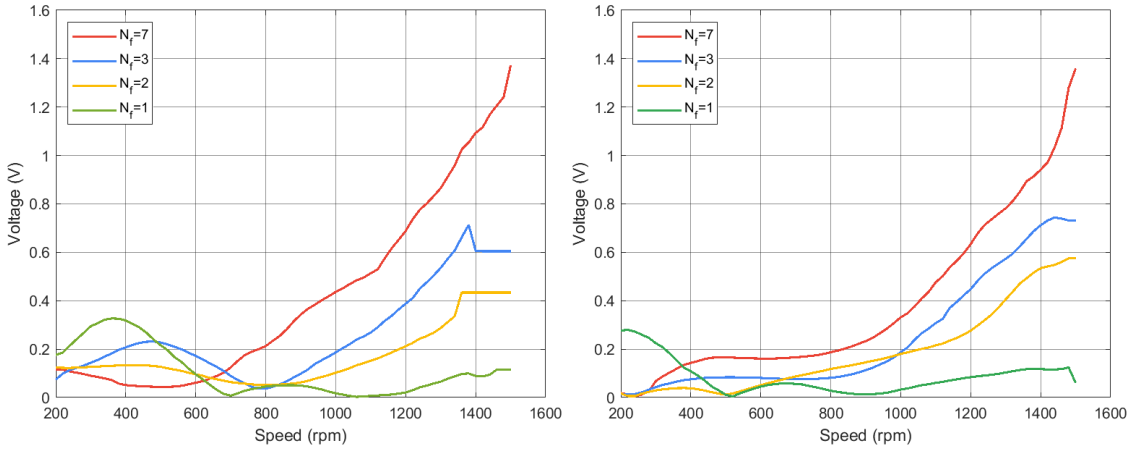

(a) (b)

Figure 5.16: Amplitude variation of $\underline{u}^{-}_{\alpha\beta}$ in varying speed conditions: (a) Motor; (b) Generator.

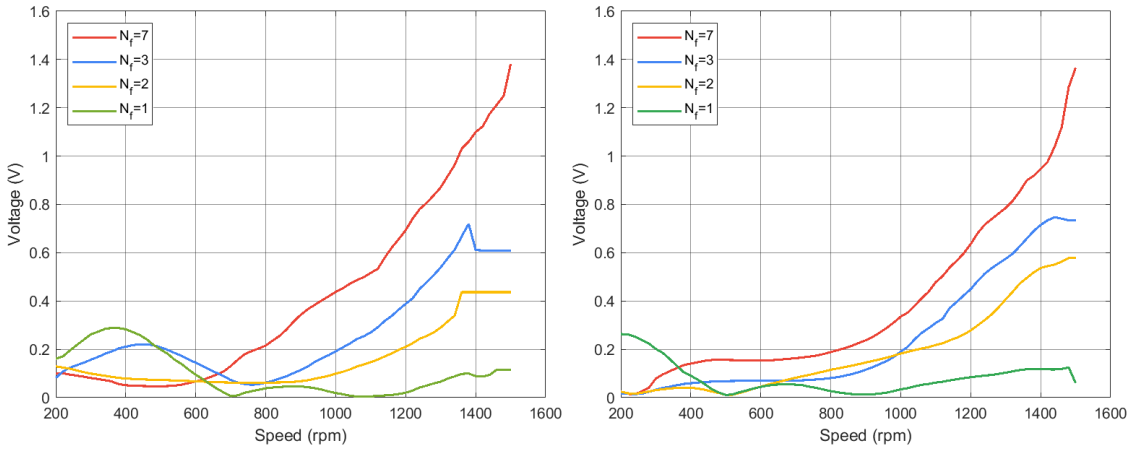

(a) (b)

Figure 5.17: Amplitude variation of $\underline{u}^{-}_{\alpha\beta}$ in varying speed conditions: (a) Motor; (b) Generator.

Phase

The one disadvantage of the MRF method in comparison with the STFT+SDT method is the requirement of the low-pass filter. And, as is illustrated in Fig. 5.18 and Fig. 5.19 this filter greatly affects the phases of the fault indicator. There is however a great deal of improvement to be done in regards to the tuning of this filter. Nevertheless, putting aside the one turn short-circuit scenario, the phase variation from 1000rpm on wards is very stable, thus making the location of the faulty phase possible in higher speeds.

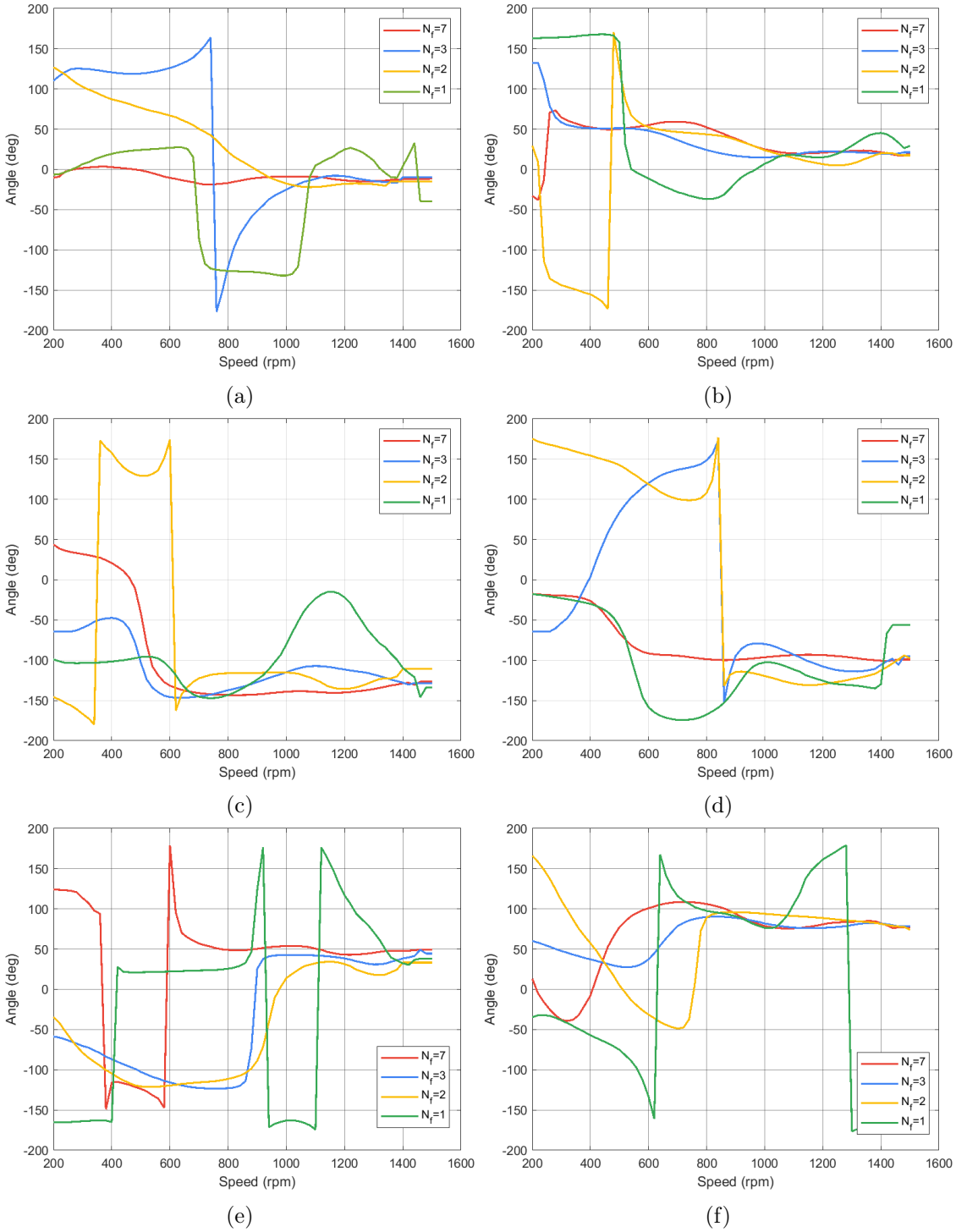

Figure 5.18: Phase variation of $\underline{u}^{-}_{\alpha\beta}$ in varying speed conditions: (a) Motor (A1); (b) Generator (A1); (c) Motor (B1); (d) Generator (B1); (e) Motor (A2); (f) Generator (A2).

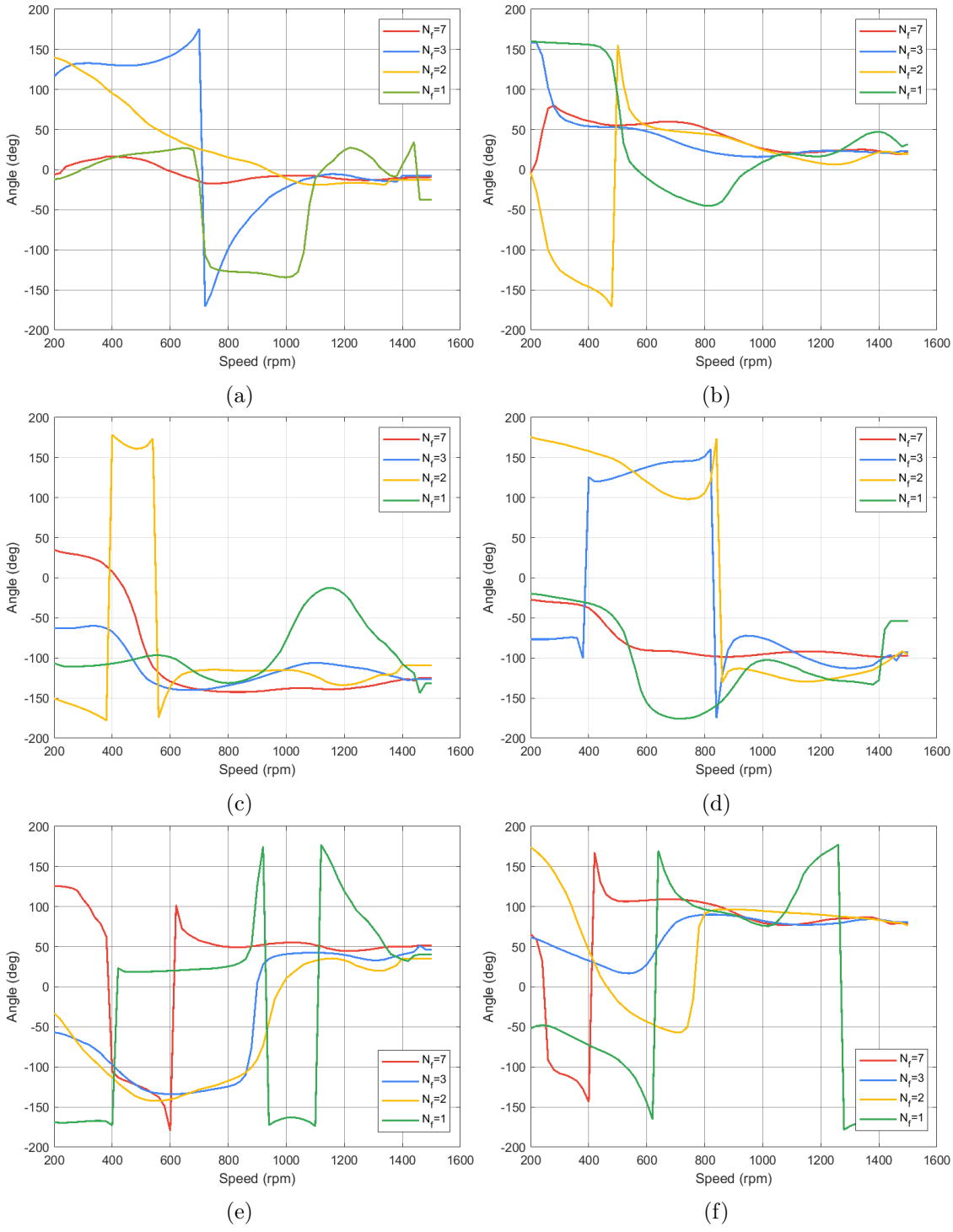

Figure 5.19: Phase variation of $\underline{e}^{-}_{\alpha\beta}$ in varying speed conditions: (a) Motor (A1); (b) Generator (A1); (c) Motor (B1); (d) Generator (B1); (e) Motor (A2); (f) Generator (A2).

Fault Severity

The effect of speed variation on the fault severity indexes is presented in Fig. 5.20 and Fig. 5.21 for $\underline{u}^{-}_{\alpha\beta}$ and $\underline{u}^{-}_{\alpha\beta}$ respectively. The fault severity index provides a measure of the severity of the ITSC fault in the stator, and as the fault indicators amplitudes increase, indicating the presence of a more significant fault, the fault severity index reflects this heightened severity.

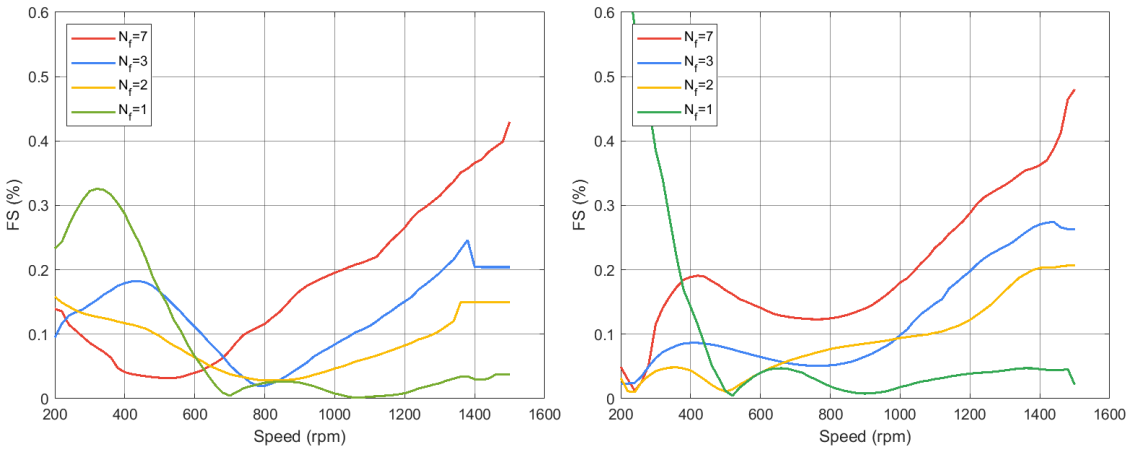

(a) (b)

Figure 5.20: Fault severity variation of $\underline{u}^{-}_{\alpha\beta}$ in varying speed conditions: (a) Motor; (b) Generator.

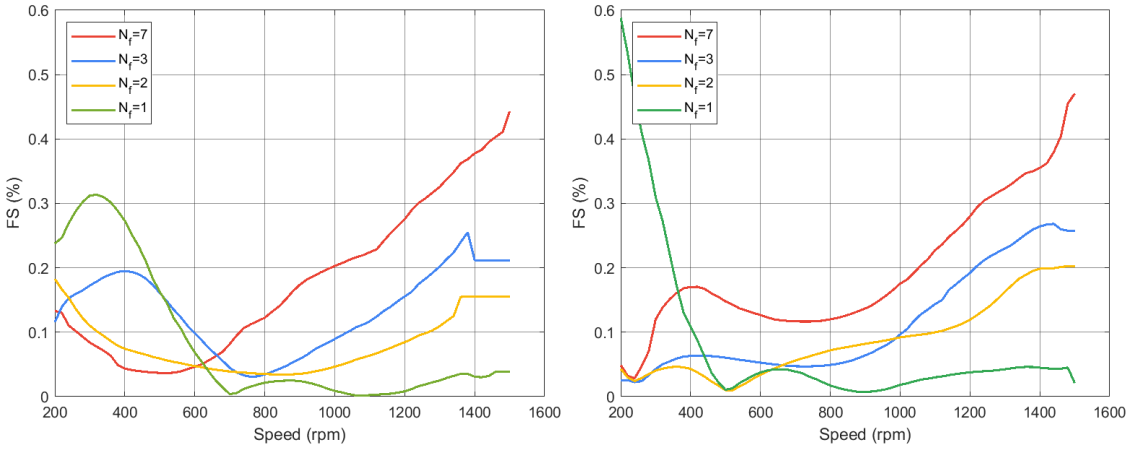

(a) (b)

Figure 5.21: Fault severity variation of $\underline{e}^{-}_{\alpha\beta}$ in varying speed conditions: (a) Motor; (b) Generator.

5.2.2 Load Torque Variation

The load variations were gathered with a constant speed of 1400 rpm under four different load percentages: 0%, 25%, 50% and 100% of the nominal value.

Amplitude

The amplitude variations of $\underline{u}^{-}_{\alpha\beta}$ and $\underline{e}^{-}_{\alpha\beta}$ are seen in Fig. 5.22 and Fig. 5.23. As expected, the varying load does not condition the amplitude values of the fault indicator.

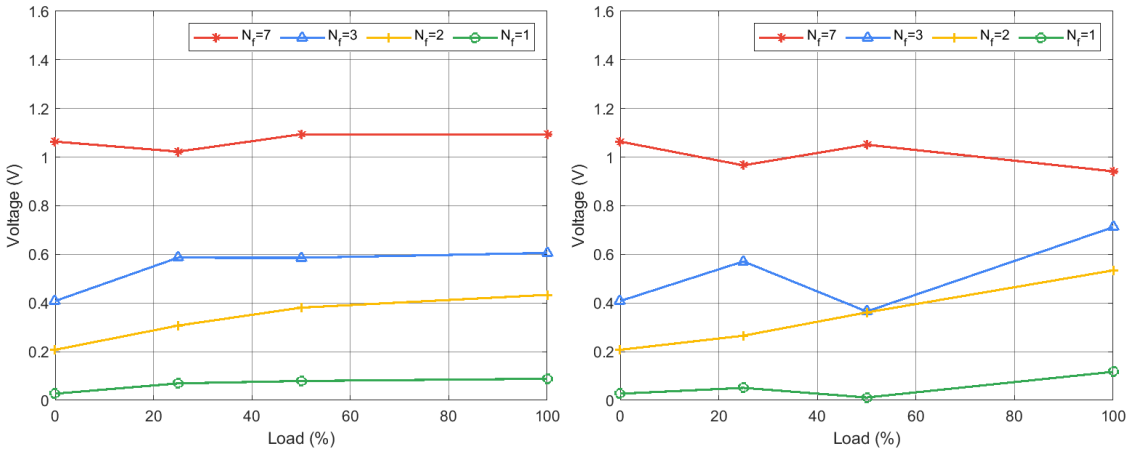

(a) (b)

Figure 5.22: Amplitude variation of $\underline{u}^{-}_{\alpha\beta}$ in varying load conditions: (a) Motor; (b) Generator.

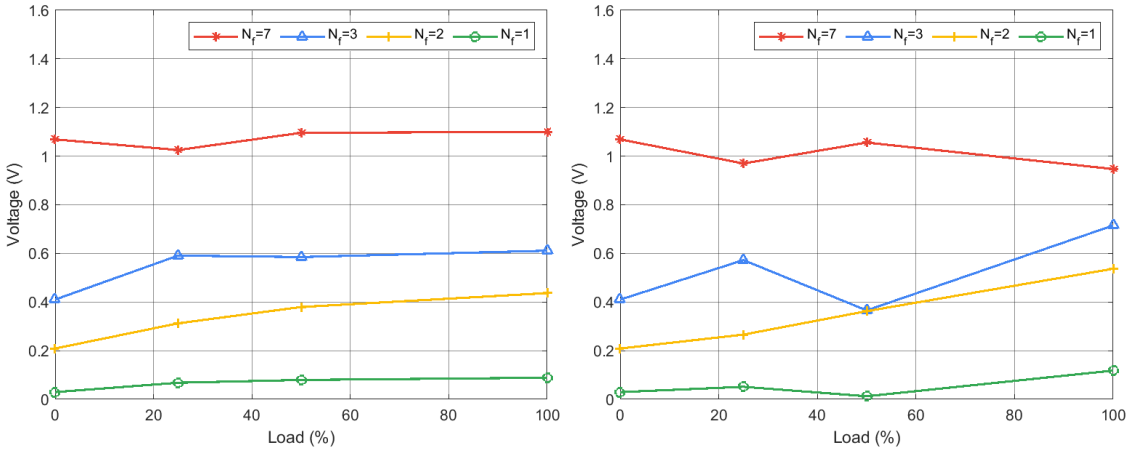

(a) (b)

Figure 5.23: Amplitude variation of $\underline{e}^{-}_{\alpha\beta}$ in varying load conditions: (a) Motor; (b) Generator.

Phase

Since the speed was maintained constant, at around 1400rpm, the filter behaved adequately. As for every case study so far, the one turn short-circuit has an unstable angle variation. In Chapter 4 it was seen that the biggest phase influence was the load variation. As can be seen from Fig. 5.24 and Fig. 5.25 the maximum variation of the phase is 20° across all fault scenarios and modes of operation. Which, allied with a better choice of

filter, would mean an easy location of the faulty phase since the 20° variation is well inside the established limit of 60°.

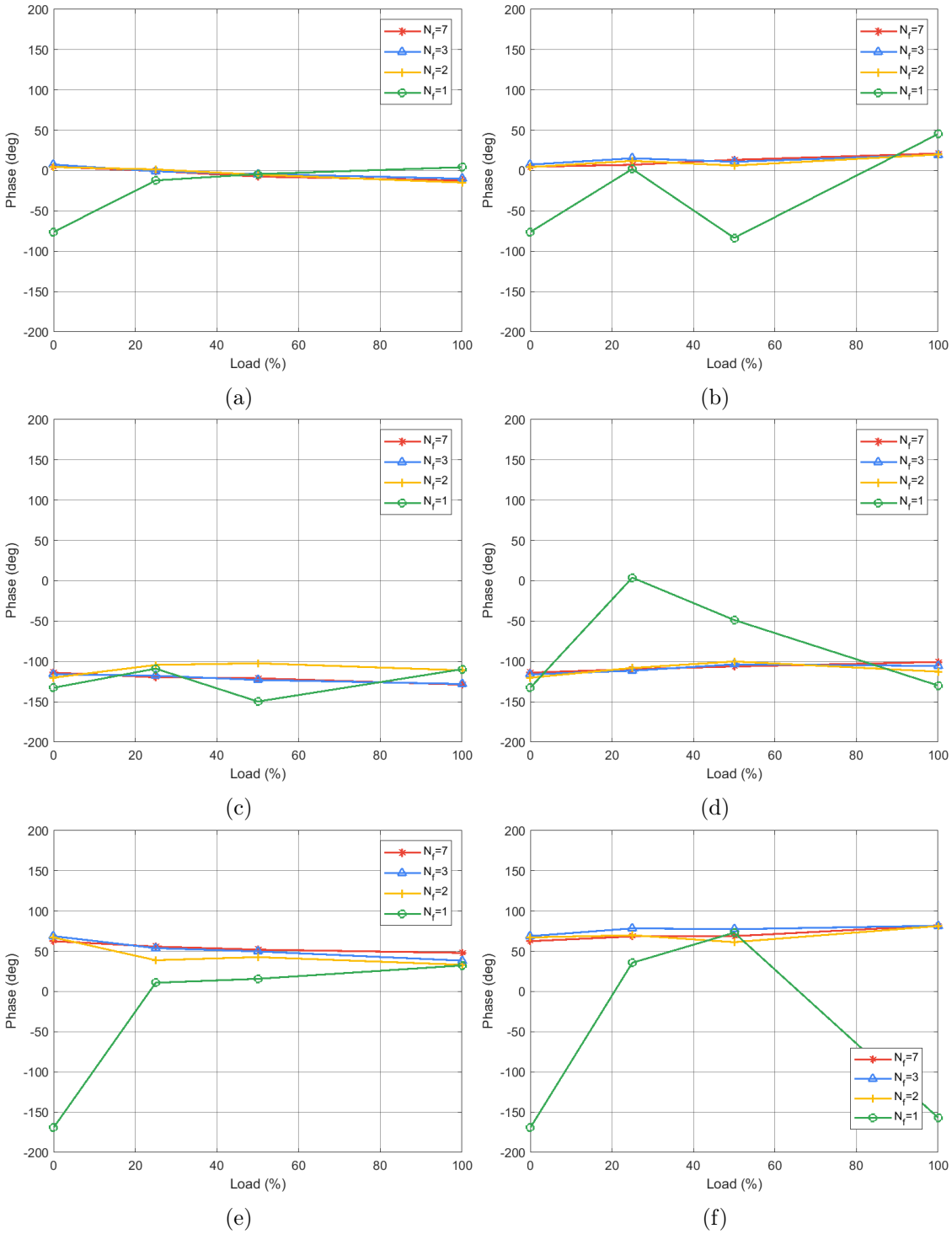

Figure 5.24: Phase variation of $\underline{u}^{-}_{\alpha\beta}$ in varying load conditions: (a) Motor (A1); (b) Generator (A1); (c) Motor (B1); (d) Generator (B1); (e) Motor (A2); (f) Generator (A2).

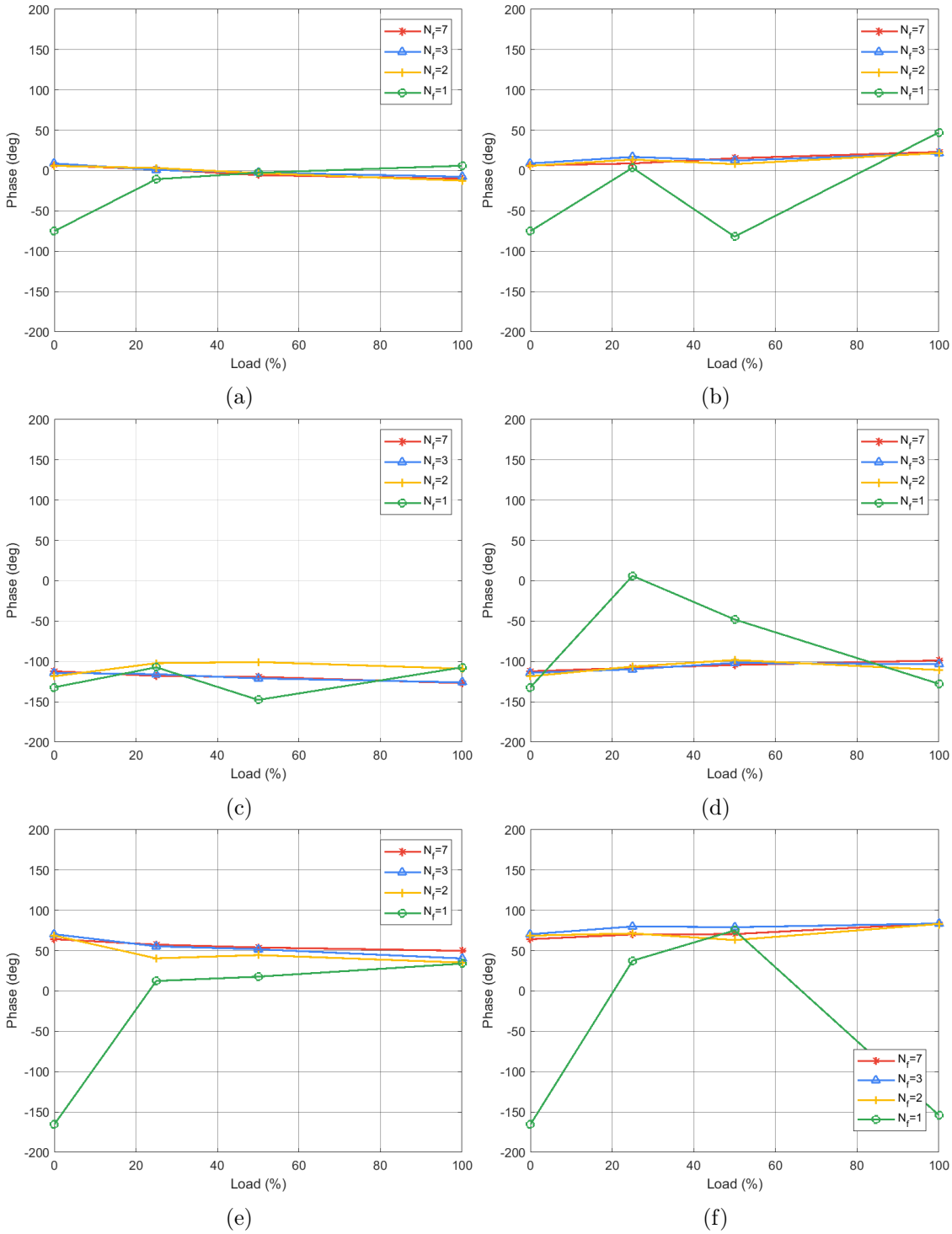

Figure 5.25: Phase variation of $\underline{e}^{-}_{\alpha\beta}$ in varying load conditions: (a) Motor (A1); (b) Generator (A1); (c) Motor (B1); (d) Generator (B1); (e) Motor (A2); (f) Generator (A2).

Fault Severity

Lastly, the fault severity index behaviour with load variations, presented in Fig. 5.26 and Fig. 5.27, corroborates with all the presumptions made so far.

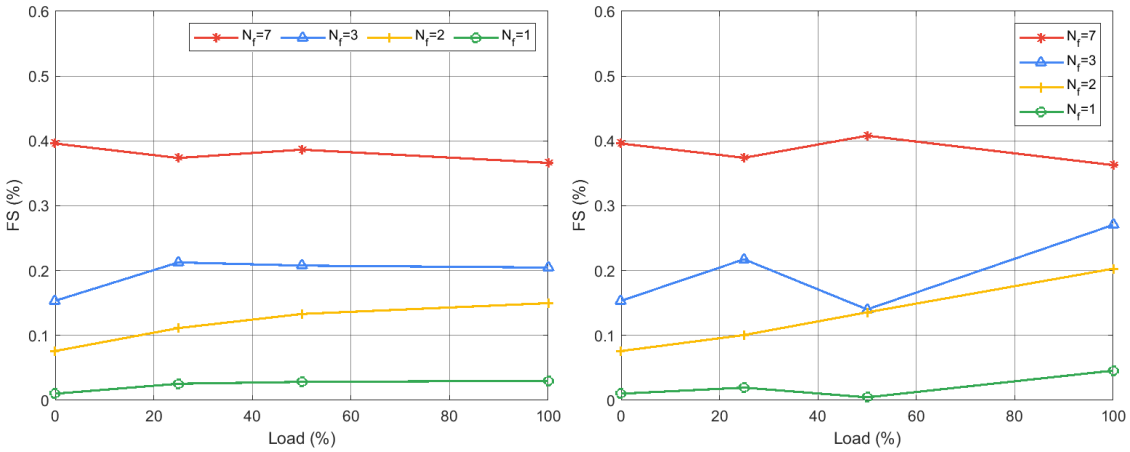

(a) (b)

Figure 5.26: Fault severity variation of $\underline{u}^{-}_{\alpha\beta}$ in varying load conditions: (a) Motor; (b) Generator.

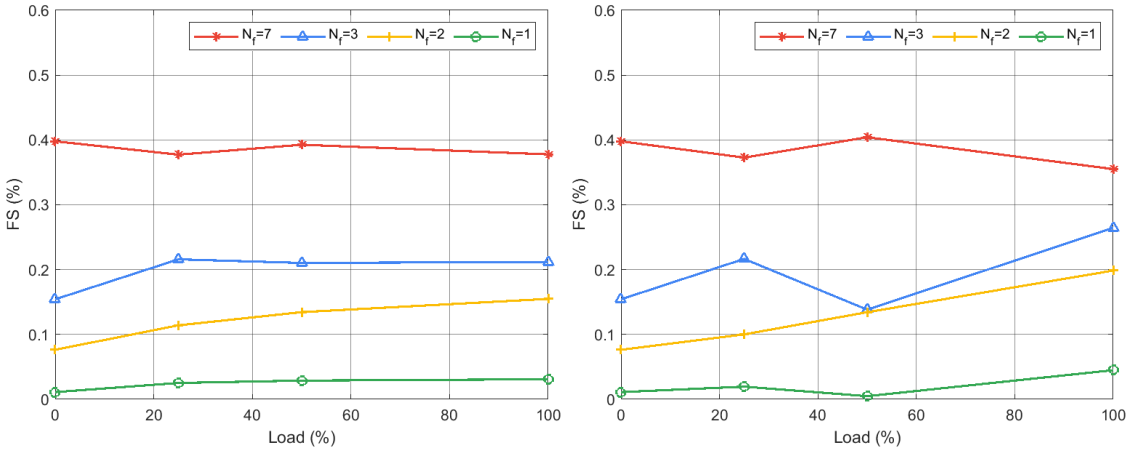

(a) (b)

Figure 5.27: Fault severity variation of $\underline{e}^{-}_{\alpha\beta}$ in varying load conditions: (a) Motor; (b) Generator.

Chapter 6

Conclusion

In this thesis, two fault detection methods were developed and successfully applied to detect interturn short-circuits and locate the faulty phase in a six-phase asymmetrical Permanent Magnet Synchronous Machine (6-PMSM), in both motor and generator modes of operations.

The first fault detection method focused on the use of the STFT. An algorithm was developed to ease the fault frequency tracking before the application of the STFT by transforming the non-stationary time-domain signal into a spatial-domain stationary signal. Through detailed studies of interturn short-circuit faults in PMSMs found in the literature, a fault index was proposed. The voltage signals as well as the estimated back-EMFs were analysed. The positive and negative sequences of the fundamental frequency were used as the fault features and the ratio between these two was used as a fault severity index. A second-term was added to the numerator of this fault index to make it independent of unbalances and/or residual asymmetries. This method demonstrated high accuracy in identifying the interturn short-circuit. This method was able to detect as few as two short-circuited turns, in an incipient fault scenario, corresponding to a fault-severity of only 0.2%. This method was also able to locate the faulty phase, as long as the machine was running above 400 rpm.

The second fault detection method, an online method, was developed to enable real-time detection and to locate the faulty phase during motor/generator operation. By continuously monitoring the electrical signals through the multiple reference frames technique and comparing them with the known fault signature values this fault detection method can efficiently detect an interturn short-circuit when it occurs. Due to the usage of a low-pass filter, this method can only locate the faulty phase at high speeds, struggling to locate the faulty phase at speeds bellow 1000 rpm.

The computational validation was conducted on a co-simulation environment with the 6-PMSM already designed in ANSYS/Simplorer and the control strategy already implemented in MATLAB/Simulink. These simulations helped to characterise the fault behaviour in the voltages and back-emf signals through the extensive testing of multiple fault scenarios.

The experimental validation was conducted on a custom-built six-phase asymmetrical PMSM. The test setup confirmed the effectiveness and reliability of the proposed fault detection methods. The performed tests proved that the offline and online techniques can detect the interturn short-circuit and, under limited speed varying conditions, also locate it. The experimental results validated the feasibility of implementing these techniques in practical systems.

Additionally, a comparison was made between the voltage and back-EMF signals throughout this work, to study which of these signals displayed a higher fault signature sensitivity. It was concluded that both have very similar fault related amplitudes in the negative se-

quence of the fundamental frequency. This outcome favours the voltage signal as it is much simpler to obtain than the back-EMF, which requires an estimator.

The successful application of the offline and online fault detection methods contributes to the field of fault detection in 6-PMSMs. The developed techniques offer enhanced reliability and safety by enabling the early detection of interturn short-circuits, mitigating the risk of catastrophic failures and reducing maintenance costs. The ability to locate the faulty phase in real-time provides valuable information for targeted repairs and improves the efficiency of maintenance procedures.

Future research directions may involve further refinement and optimisation of the fault detection methods to enhance their robustness and adaptability to different motor operating conditions, such as low speeds. With regard to the offline method, other time-frequency representations could be studied to better extract the phase information since in this work only the accuracy of the amplitude readings was considered. As for the online method, a better tuning of the low-pass filter could be sought, in hope of increasing the speed range where the fault location can be determined. The back-EMF estimation done in this work was very simplistic. The question remains as to whether a more complex (and accurate) estimation of this back-EMF could improve these methods sensitivity in the detection of the ITSC. Additionally, the integration of artificial intelligence in both offline and online methods, could be explored as a decision-making tool, improving the overall fault detection accuracy.

In conclusion, this thesis successfully addressed the interturn short-circuit fault detection challenge in six-phase asymmetrical PMSMs through the development of not only one, but two fault detection methods. The research outcomes contribute to the advancement of fault detection techniques for multiphase motor/generator systems, promoting the reliability, safety, and performance of electrical machinery in various applications.

References

[1] P. Xu, J. H. Feng, S. Y. Guo, *et al.*, "Analysis of dual three-phase permanent-magnet synchronous machines with different angle displacements," *IEEE Transactions on Industrial Electronics*, vol. 65, no. 3, pp. 1941–1954, 2018, ISSN: 0278-0046. DOI: 10.1109/tie.2017.2748035. [Online]. Available: https://dx.doi.org/10.1109/tie.2017.2748035.

[2] Y. Gritli, A. Tani, C. Rossi, and D. Casadei, "Detection of rotor magnet demagnetization in asymmetrical six-phase surface mounted permanent magnet synchronous motor drive," IEEE, 2018. DOI: 10.1109/icelmach.2018.8506688. [Online]. Available: https://dx.doi.org/10.1109/icelmach.2018.8506688.

[3] T. Orlowska-Kowalska, M. Wolkiewicz, P. Pietrzak, *et al.*, "Fault diagnosis and fault-tolerant control of PMSM drives–state of the art and future challenges," *IEEE Access*, vol. 10, pp. 59 979–60 024, 2022, Conference Name: IEEE Access, ISSN: 2169-3536. DOI: 10.1109/ACCESS.2022.3180153.

[4] M. Zafarani, E. Bostanci, Y. Qi, T. Goktas, and B. Akin, "Interturn short-circuit faults in permanent magnet synchronous machines: An extended review and comprehensive analysis," *IEEE Journal of Emerging and Selected Topics in Power Electronics*, vol. 6, no. 4, pp. 2173–2191, 2018, ISSN: 2168-6777. DOI: 10.1109/jestpe.2018.2811538. [Online]. Available: https://dx.doi.org/10.1109/jestpe.2018.2811538.

[5] K.-H. Kim, "Simple online fault detecting scheme for short-circuited turn in a PMSM through current harmonic monitoring," *IEEE Transactions on Industrial Electronics*, vol. 58, no. 6, pp. 2565–2568, 2011, ISSN: 0278-0046. DOI: 10.1109/tie.2010.2060463. [Online]. Available: https://dx.doi.org/10.1109/tie.2010.2060463.

[6] B. M. Ebrahimi and J. Faiz, "Feature extraction for short-circuit fault detection in permanent-magnet synchronous motors using stator-current monitoring," *IEEE Transactions on Power Electronics*, vol. 25, no. 10, pp. 2673–2682, 2010, ISSN: 0885-8993. DOI: 10.1109/tpel.2010.2050496. [Online]. Available: https://dx.doi.org/10.1109/tpel.2010.2050496.

[7] J. A. Rosero, L. Romeral, J. Cusido, A. Garcia, and J. A. Ortega, "On the short-circuiting fault detection in a PMSM by means of stator current transformations," IEEE, 2007. DOI: 10.1109/pesc.2007.4342300. [Online]. Available: https://dx.doi.org/10.1109/pesc.2007.4342300.

[8] J. Zhang, Z. Xu, J. Wang, J. Zhao, Z. Din, and M. Cheng, "Detection and discrimination of incipient stator faults for inverter-fed permanent magnet synchronous machines," *IEEE Transactions on Industrial Electronics*, vol. 68, no. 8, pp. 7505–7515, Aug. 2021, Conference Name: IEEE Transactions on Industrial Electronics, ISSN: 1557-9948. DOI: 10.1109/TIE.2020.3009563.

[9] W. G. Zanardelli, E. G. Strangas, and S. Aviyente, "Identification of intermittent electrical and mechanical faults in permanent-magnet AC drives based on time–frequency analysis," *IEEE Transactions on Industry Applications*, vol. 43, no. 4, pp. 971–980, 2007, ISSN: 0093-9994. DOI: 10.1109/tia.2007.900446. [Online]. Available: https://dx.doi.org/10.1109/tia.2007.900446.

[10] N. Haje Obeid, A. Battiston, T. Boileau, and B. Nahid-Mobarakeh, "Early intermittent interturn fault detection and localization for a permanent magnet synchronous motor of electrical vehicles using wavelet transform," *IEEE Transactions on Transportation Electrification*, vol. 3, no. 3, pp. 694–702, Sep. 2017, Conference Name: IEEE Transactions on Transportation Electrification, ISSN: 2332-7782. DOI: 10.1109/TTE.2017.2743419.

[11] J. Hang, J. Zhang, M. Xia, S. Ding, and W. Hua, "Interturn fault diagnosis for model-predictive-controlled-PMSM based on cost function and wavelet transform," *IEEE Transactions on Power Electronics*, vol. 35, no. 6, pp. 6405–6418, 2020, ISSN: 0885-8993. DOI: 10.1109/tpel.2019.2953269. [Online]. Available: https://dx.doi.org/10.1109/tpel.2019.2953269.

[12] J. A. Rosero, L. Romeral, J. A. Ortega, and E. Rosero, "Short-circuit detection by means of empirical mode decomposition and wigner–ville distribution for PMSM running under dynamic condition," *IEEE Transactions on Industrial Electronics*, vol. 56, no. 11, pp. 4534–4547, 2009, ISSN: 0278-0046. DOI: 10.1109/tie.2008.2011580. [Online]. Available: https://dx.doi.org/10.1109/tie.2008.2011580.

[13] A. Sarikhani and O. A. Mohammed, "Inter-turn fault detection in PM synchronous machines by physics-based back electromotive force estimation," *IEEE Transactions on Industrial Electronics*, vol. 60, no. 8, pp. 3472–3484, 2013, Section: 3472, ISSN: 0278-0046 1557-9948. DOI: 10.1109/tie.2012.2222857.

[14] M. A. Mazzoletti, G. R. Bossio, C. H. De Angelo, and D. R. Espinoza-Trejo, "A model-based strategy for interturn short-circuit fault diagnosis in PMSM," *IEEE Transactions on Industrial Electronics*, vol. 64, no. 9, pp. 7218–7228, 2017, ISSN: 0278-0046. DOI: 10.1109/tie.2017.2688973. [Online]. Available: https://dx.doi.org/10.1109/tie.2017.2688973.

[15] B. Aubert, J. Regnier, S. Caux, and D. Alejo, "Kalman-filter-based indicator for online interturn short circuits detection in permanent-magnet synchronous generators," *IEEE Transactions on Industrial Electronics*, vol. 62, no. 3, pp. 1921–1930, 2015, Section: 1921, ISSN: 0278-0046 1557-9948. DOI: 10.1109/tie.2014.2348934.

[16] W. Li, G. Feng, Z. Li, J. Tjong, and N. Kar, "Multireference frame based open-phase fault modeling and control for asymmetrical six-phase interior permanent magnet motors," *IEEE Transactions on Power Electronics*, vol. 36, no. 10, pp. 11 712–11 725, 2021, Section: 11712, ISSN: 0885-8993 1941-0107. DOI: 10.1109/tpel.2021.3072947.

[17] P. F. C. Gonçalves, S. M. A. Cruz, and A. M. S. Mendes, "Online diagnostic method for the detection of high-resistance connections and open-phase faults in six-phase PMSM drives," *IEEE Transactions on Industry Applications*, vol. 58, no. 1, pp. 345–355, Jan. 2022, Conference Name: IEEE Transactions on Industry Applications, ISSN: 1939-9367. DOI: 10.1109/TIA.2021.3120239.

[18] H. Chen, J. He, N. A. O. Demerdash, X. Guan, and C. H. T. Lee, "Diagnosis of open-phase faults for a five-phase PMSM fed by a closed-loop vector-controlled drive based on magnetic field pendulous oscillation technique," *IEEE Transactions on Industrial Electronics*, vol. 68, no. 7, pp. 5582–5593, Jul. 2021, Conference Name: IEEE Transactions on Industrial Electronics, ISSN: 1557-9948. DOI: 10.1109/TIE.2020.3000109.

[19] H. Chen, J. He, X. Guan, N. A. O. Demerdash, A. M. EL-Refaie, and C. H. T. Lee, "High-resistance connection diagnosis in five-phase PMSMs based on the method of magnetic field pendulous oscillation and symmetrical components," *IEEE Transactions on Industrial Electronics*, vol. 69, no. 3, pp. 2288–2299, Mar. 2022, Conference Name: IEEE Transactions on Industrial Electronics, ISSN: 1557-9948. DOI: 10.1109/TIE.2021.3065617.

[20] Y. Gritli, C. Rossi, G. Rizzoli, M. Mengoni, A. Tani, and D. Casadei, "Robust online magnet demagnetization diagnosis in asymmetrical six-phase AC permanent magnet motor drives," *IEEE Access*, vol. 11, pp. 50 769–50 780, 2023, Conference Name: IEEE Access, ISSN: 2169-3536. DOI: 10.1109/ACCESS.2023.3278025.

[21] Z. Yuan, M. Wang, J. Bai, J. Huang, and P. Zheng, "Influence of mutual inductance on high-frequency impedance characteristics of six-phase PMSM under inter-turn short-circuit fault," in *2022 25th International Conference on Electrical Machines and Systems (ICEMS)*, ISSN: 2642-5513, Nov. 2022, pp. 1–5. DOI: 10.1109/ICEMS56177.2022.9982968.

[22] Y. Gritli, A. Tani, C. Rossi, D. Casadei, and G. Serra, "Experimental assessment of winding inter-turn short-circuits in six-phase AC permanent magnet synchronous motors," in *2019 International Conference on Clean Electrical Power (ICCEP)*, ISSN: 2474-9664, Jul. 2019, pp. 29–35. DOI: 10.1109/ICCEP.2019.8890140.

[23] Q. Chen, L. Gu, J. Wang, W. Zhao, and G. Liu, "Remedy strategy for five-phase FTPMMs under single-phase short-circuit fault by injecting harmonic currents from third space," *IEEE Transactions on Power Electronics*, vol. 37, no. 9, pp. 11 152–11 163, Sep. 2022, Conference Name: IEEE Transactions on Power Electronics, ISSN: 1941-0107. DOI: 10.1109/TPEL.2022.3162847.

[24] X. Wang, G. Liu, Q. Chen, A. Farahat, and X. Song, "Multivectors model predictive control with voltage error tracking for five-phase PMSM short-circuit fault-tolerant operation," *IEEE Transactions on Transportation Electrification*, vol. 8, no. 1, pp. 675–687, Mar. 2022, Conference Name: IEEE Transactions on Transportation Electrification, ISSN: 2332-7782. DOI: 10.1109/TTE.2021.3099345.

[25] B. Sen and J. Wang, "Stator interturn fault detection in permanent-magnet machines using PWM ripple current measurement," *IEEE Transactions on Industrial Electronics*, vol. 63, no. 5, pp. 3148–3157, May 2016, Conference Name: IEEE Transactions on Industrial Electronics, ISSN: 1557-9948. DOI: 10.1109/TIE.2016.2515560.

[26] J. Xu, X. Tian, W. Jin, and H. Guo, "PWM harmonic-current-based interturn short-circuit fault diagnosis for the aerospace FTPMSM system even in the fault-tolerant operation condition," *IEEE Transactions on Power Electronics*, vol. 38, no. 4, pp. 5432–5441, Apr. 2023, Conference Name: IEEE Transactions on Power Electronics, ISSN: 1941-0107. DOI: 10.1109/TPEL.2023.3238167.

[27] R. Cui, Y. Fan, and C. Li, "On-line inter-turn short-circuit fault diagnosis and torque ripple minimization control strategy based on OW five-phase BFTHE-IPM," *IEEE Transactions on Energy Conversion*, vol. 33, no. 4, pp. 2200–2209, Dec. 2018, Conference Name: IEEE Transactions on Energy Conversion, ISSN: 1558-0059. DOI: 10.1109/TEC.2018.2851615.

[28] V. Abril, "Diagnóstico e análise de avarias nos enrolamentos estatóricos de um PMSM hexafásico com controlo preditivo," msthesis, University of Coimbra, 2021.

[29] S. Nandi, H. A. Toliyat, and X. Li, "Condition monitoring and fault diagnosis of electrical motors—a review," *IEEE Transactions on Energy Conversion*, vol. 20, no. 4, pp. 719–729, 2005, ISSN: 0885-8969. DOI: 10.1109/tec.2005.847955. [Online]. Available: https://dx.doi.org/10.1109/tec.2005.847955.

[30] R. R. Schoen, T. G. Habetler, F. Kamran, and R. G. Bartheld, "Motor bearing damage detection using stator current monitoring," IEEE. DOI: 10.1109/ias.1994.345491. [Online]. Available: https://dx.doi.org/10.1109/ias.1994.345491.

[31] S. Nandi, T. C. Ilamparithi, S. B. Lee, and D. Hyun, "Detection of eccentricity faults in induction machines based on nameplate parameters," *IEEE Transactions on Industrial Electronics*, vol. 58, no. 5, pp. 1673–1683, 2011, ISSN: 0278-0046. DOI: 10.1109/tie.2010.2055772. [Online]. Available: https://dx.doi.org/10.1109/tie.2010.2055772.

[32] A. Bellini, F. Filippetti, C. Tassoni, and G. A. Capolino, "Advances in diagnostic techniques for induction machines," *IEEE Transactions on Industrial Electronics*, vol. 55, no. 12, pp. 4109–4126, 2008, ISSN: 0278-0046. DOI: 10.1109/tie.2008.2007527. [Online]. Available: https://dx.doi.org/10.1109/tie.2008.2007527.

[33] P. F. C. Goncalves, S. M. A. Cruz, and A. M. S. Mendes, "Diagnosis of open-phase faults and high resistance connections in six-phase PMSM drives," IEEE, 2020. DOI: 10.1109/sest48500.2020.9203465. [Online]. Available: https://dx.doi.org/10.1109/sest48500.2020.9203465.

[34] Z. Ullah and J. Hur, "Analysis of inter-turn-short fault in an FSCW IPM type brushless motor considering effect of control drive," *IEEE Transactions on Industry Applications*, vol. 56, no. 2, pp. 1356–1367, 2020, Section: 1356, ISSN: 0093-9994 1939-9367. DOI: 10.1109/tia.2019.2961878.

[35] Y. Qi, E. Bostanci, M. Zafarani, and B. Akin, "Severity estimation of interturn short circuit fault for PMSM," *IEEE Transactions on Industrial Electronics*, vol. 66, no. 9, pp. 7260–7269, 2019, Section: 7260, ISSN: 0278-0046 1557-9948. DOI: 10.1109/tie.2018.2879281.

[36] S. Zhang and T. G. Habetler, "Transient demagnetization characteristics of interior permanent magnet synchronous machines with stator inter-turn short circuit faults for automotive applications," IEEE, 2018. DOI: 10.1109/ecce.2018.8558143. [Online]. Available: https://dx.doi.org/10.1109/ecce.2018.8558143.

[37] M. Pastura, S. Nuzzo, F. Immovilli, *et al.*, "Partial discharges in electrical machines for the more electric aircraft—part i: A comprehensive modeling tool for the characterization of electric drives based on fast switching semiconductors," *IEEE Access*, vol. 9, pp. 27 109–27 121, 2021, Conference Name: IEEE Access, ISSN: 2169-3536. DOI: 10.1109/ACCESS.2021.3058083.

[38] L. Lusuardi, A. Rumi, A. Cavallini, D. Barater, and S. Nuzzo, "Partial discharge phenomena in electrical machines for the more electrical aircraft. part II: Impact of reduced pressures and wide bandgap devices," *IEEE Access*, vol. 9, pp. 27 485–27 495, 2021, Conference Name: IEEE Access, ISSN: 2169-3536. DOI: 10.1109/ACCESS.2021.3058089.

[39] WEG. "Danos em enrolamentos de motores trifásicos." (), [Online]. Available: https://static.weg.net/medias/downloadcenter/h0b/hbf/WEG-danos-em-enrolamentos-motores-trifasicos-50009255-brochure-portuguese-web.pdf.

[40] J.-C. Urresty, J.-R. Riba, and L. Romeral, "A back-emf based method to detect magnet failures in PMSMs," *IEEE Transactions on Magnetics*, vol. 49, no. 1, pp. 591–598, 2013, Section: 591, ISSN: 0018-9464 1941-0069. DOI: 10.1109/tmag.2012.2207731.

[41] J. Faiz and E. Mazaheri-Tehrani, "Demagnetization modeling and fault diagnosing techniques in permanent magnet machines under stationary and nonstationary conditions: An overview," *IEEE Transactions on Industry Applications*, vol. 53, no. 3, pp. 2772–2785, 2017, ISSN: 0093-9994. DOI: 10.1109/tia.2016.2608950. [Online]. Available: https://dx.doi.org/10.1109/tia.2016.2608950.

[42] P. F. C. Goncalves, "Fault-tolerant predictive control of PMSGs in offshore wind turbines," Ph.D. dissertation, University of Coimbra, Coimbra, 2022.

[43] B. Wang, N. Hu, L. Chen, Y. Yang, Z. Yin, and Y. Zhou, "Demagnetization fault detection in surface-mounted permanent magnet synchronous machine," IEEE, 2021. DOI: 10.1109/phm-nanjing52125.2021.9612845. [Online]. Available: https://dx.doi.org/10.1109/phm-nanjing52125.2021.9612845.

[44] S. Choi, M. S. Haque, M. T. B. Tarek, *et al.*, "Fault diagnosis techniques for permanent magnet AC machine and drives—a review of current state of the art," *IEEE Transactions on Transportation Electrification*, vol. 4, no. 2, pp. 444–463, 2018, ISSN: 2332-7782. DOI: 10.1109/tte.2018.2819627. [Online]. Available: https://dx.doi.org/10.1109/tte.2018.2819627.

[45] J. Urresty, J. Riba, L. Romeral, J. Rosero, and J. Serna, "Stator short circuits detection in PMSM by means of hilbert-huang transform and energy calculation," IEEE, 2009. DOI: 10.1109/demped.2009.5292789. [Online]. Available: https://dx.doi.org/10.1109/demped.2009.5292789.

[46] R. Z. Haddad and E. G. Strangas, "Fault detection and classification in permanent magnet synchronous machines using fast fourier transform and linear discriminant analysis," in *2013 9th IEEE International Symposium on Diagnostics for Electric Machines, Power Electronics and Drives (SDEMPED)*, Aug. 2013, pp. 99–104. DOI: 10.1109/DEMPED.2013.6645703.

[47] S. M. A. Cruz and A. J. M. Cardoso, "Stator winding fault diagnosis in three-phase synchronous and asynchronous motors, by the extended park's vector approach," *IEEE Transactions on Industry Applications*, vol. 37, no. 5, pp. 1227–1233, 2001, ISSN: 0093-9994. DOI: 10.1109/28.952496. [Online]. Available: https://dx.doi.org/10.1109/28.952496.

[48] D. S. B. Fonseca, C. M. C. Santos, and A. J. M. Cardoso, "Stator faults modeling and diagnostics of line-start permanent magnet synchronous motors," *IEEE Transactions on Industry Applications*, vol. 56, no. 3, pp. 2590–2599, May 2020, Conference Name: IEEE Transactions on Industry Applications, ISSN: 1939-9367. DOI: 10.1109/TIA.2020.2979674.

[49] F. Çira, M. Arkan, B. Gümüş, and T. Goktas, "Analysis of stator inter-turn short-circuit fault signatures for inverter-fed permanent magnet synchronous motors," in *IECON 2016 - 42nd Annual Conference of the IEEE Industrial Electronics Society*, Oct. 2016, pp. 1453–1457. DOI: 10.1109/IECON.2016.7793717.

[50] J. Quiroga, L. Liu, and D. A. Cartes, "Fuzzy logic based fault detection of PMSM stator winding short under load fluctuation using negative sequence analysis," in *2008 American Control Conference*, ISSN: 2378-5861, Jun. 2008, pp. 4262–4267. DOI: 10.1109/ACC.2008.4587163.

[51] C. H. Park, J. Lee, G. Ahn, M. Youn, and B. D. Youn, "Fault detection of PMSM under non-stationary conditions based on wavelet transformation combined with distance approach," IEEE, 2019. DOI: 10.1109/demped.2019.8864842. [Online]. Available: https://dx.doi.org/10.1109/demped.2019.8864842.

[52] Z. A. Ping, Y. Juan, and W. Ling, "Fault detection of stator winding interturn short circuit in PMSM based on wavelet packet analysis," IEEE, 2013. DOI: 10.1109/icmtma.2013.141. [Online]. Available: https://dx.doi.org/10.1109/icmtma.2013.141.

[53] F. Alvarez-Gonzalez, A. Griffo, and B. Wang, "Permanent magnet synchronous machine stator windings fault detection by hilbert–huang transform," *The Journal of Engineering*, vol. 2019, no. 17, pp. 3505–3509, 2019, ISSN: 2051-3305. DOI: 10.1049/joe.2018.8173. [Online]. Available: https://onlinelibrary.wiley.com/doi/abs/10.1049/joe.2018.8173 (visited on 06/09/2023).

[54] Z. Dogan and K. Tetik, "Diagnosis of inter-turn faults based on fault harmonic component tracking in LSPMSMs working under nonstationary conditions," *IEEE Access*, vol. 9, pp. 92 101–92 112, 2021, Conference Name: IEEE Access, ISSN: 2169-3536. DOI: 10.1109/ACCESS.2021.3092605.

[55] J. Fang, Y. Sun, Y. Wang, B. Wei, and J. Hang, "Improved ZSVC-based fault detection technique for incipient stage inter-turn fault in PMSM," *IET Electric Power Applications*, vol. 13, no. 12, pp. 2015–2026, 2019, ISSN: 1751-8679. DOI: 10.1049/iet-epa.2019.0016. [Online]. Available: https://onlinelibrary.wiley.com/doi/abs/10.1049/iet-epa.2019.0016 (visited on 06/09/2023).

[56] J. Hang, J. Zhang, M. Cheng, and J. Huang, "Online interturn fault diagnosis of permanent magnet synchronous machine using zero-sequence components," *IEEE Transactions on Power Electronics*, vol. 30, no. 12, pp. 6731–6741, 2015, ISSN: 0885-8993. DOI: 10.1109/tpel.2015.2388493. [Online]. Available: https://dx.doi.org/10.1109/tpel.2015.2388493.

[57] T. Boileau, N. Leboeuf, B. Nahid-Mobarakeh, and F. Meibody-Tabar, "Synchronous demodulation of control voltages for stator interturn fault detection in PMSM," *IEEE Transactions on Power Electronics*, vol. 28, no. 12, pp. 5647–5654, Dec. 2013, Conference Name: IEEE Transactions on Power Electronics, ISSN: 1941-0107. DOI: 10.1109/TPEL.2013.2254132.

[58] G. Ahn, J. Lee, C. H. Park, M. Youn, and B. D. Youn, "Inter-turn short circuit fault detection in permanent magnet synchronous motors based on reference voltage," in *2019 IEEE 12th International Symposium on Diagnostics for Electrical Machines, Power Electronics and Drives (SDEMPED)*, Aug. 2019, pp. 245–250. DOI: 10.1109/DEMPED.2019.8864924.

[59] F. Meinguet, E. Semail, X. Kestelyn, Y. Mollet, and J. Gyselinck, "Change-detection algorithm for short-circuit fault detection in closed-loop AC drives," *IET Electric Power Applications*, vol. 8, no. 5, pp. 165–177, 2014, ISSN: 1751-8679. DOI: 10.1049/iet-epa.2012.0316. [Online]. Available: https://onlinelibrary.wiley.com/doi/abs/10.1049/iet-epa.2012.0316 (visited on 06/13/2023).

[60] B. Du, S. Wu, S. Han, and S. Cui, "Interturn fault diagnosis strategy for interior permanent-magnet synchronous motor of electric vehicles based on digital signal processor," *IEEE Transactions on Industrial Electronics*, vol. 63, no. 3, pp. 1694–1706, 2016, ISSN: 0278-0046. DOI: 10.1109/tie.2015.2496900. [Online]. Available: https://dx.doi.org/10.1109/tie.2015.2496900.

[61] Z. Gao, C. Cecati, and S. Ding, "A survey of fault diagnosis and fault-tolerant techniques part II: Fault diagnosis with knowledge-based and hybrid/active approaches," *IEEE Transactions on Industrial Electronics*, pp. 1–1, 2015, ISSN: 0278-0046. DOI: 10.1109/tie.2015.2419013. [Online]. Available: https://dx.doi.org/10.1109/tie.2015.2419013.

[62] S. Liang, Y. Chen, H. Liang, and X. Li, "Sparse representation and svm diagnosis method for inter-turn short-circuit fault in pmsm," *Applied Sciences*, vol. 9, no. 2, p. 224, 2019, ISSN: 2076-3417. DOI: 10.3390/app9020224. [Online]. Available: https://www.mdpi.com/2076-3417/9/2/224.

[63] J. W. Cooley and J. W. Tukey, "An algorithm for the machine calculation of complex fourier series," *Mathematics of Computation*, vol. 19, no. 90, pp. 297–301, 1965.

[64] D. Gabor, "Theory of communication," 1945.

[65] Y. Meyer, *Wavelets: Algorithms and Aapplications*. Philadelphia: SIAM (Society for Industrial and Applied Mathematics)., 1993.

[66] N. E. Huang, Z. Shen, S. R. Long, *et al.*, "The empirical mode decomposition and the hilbert spectrum for nonlinear and non-stationary time series analysis," *Proceedings of the Royal Society of London. Series A: Mathematical, Physical and Engineering Sciences*, vol. 454, no. 1971, pp. 903–995, 1998, ISSN: 1364-5021. DOI: 10.1098/rspa.1998.0193. [Online]. Available: https://dx.doi.org/10.1098/rspa.1998.0193.

[67] H.-I. Choi and W. J. Williams, "Improved time-frequency representation of multicomponent signals using exponential kernels," *IEEE Transactions on Acoustics, Speech, and Signal Processing*, vol. 37, no. 6, 1989.

[68] Y. Zhao, L. E. Atlas, and R. J. Marks, "The use of cone-shaped kernels for generalized time-frequency representations of nonstationary signals," *IEEE Transactions on Acoustics, Speech, and Signal Processing*, vol. 38, no. 7, pp. 1084–1091, 1990, ISSN: 0096-3518. DOI: 10.1109/29.57537. [Online]. Available: https://dx.doi.org/10.1109/29.57537.

[69] P. F. Gonçalves, S. M. Cruz, and A. M. Mendes, "Design of a six-phase asymmetrical permanent magnet synchronous generator for wind energy applications," *The Journal of Engineering*, vol. 2019, no. 17, pp. 4532–4536, 2019, ISSN: 2051-3305. DOI: 10.1049/joe.2018.8175. [Online]. Available: https://onlinelibrary.wiley.com/doi/abs/10.1049/joe.2018.8175 (visited on 06/14/2023).

[70] Y. Zhao and T. Lipo, "Space vector PWM control of dual three-phase induction machine using vector space decomposition," *IEEE Transactions on Industry Applications*, vol. 31, no. 5, pp. 1100–1109, Sep. 1995, Conference Name: IEEE Transactions on Industry Applications, ISSN: 1939-9367. DOI: 10.1109/28.464525.

[71] E. Etien, A. Allouche, L. Rambault, T. Doget, S. Cauet, and A. Sakout, "A tacholess order analysis method for PMSG mechanical fault detection with varying speeds," *Electronics*, vol. 10, no. 4, p. 418, Jan. 2021, Number: 4 Publisher: Multidisciplinary Digital Publishing Institute, ISSN: 2079-9292. DOI: 10.3390/electronics10040418. [Online]. Available: https://www.mdpi.com/2079-9292/10/4/418 (visited on 09/20/2022).

[72] F. Cheng, L. Qu, W. Qiao, C. Wei, and L. Hao, "Fault diagnosis of wind turbine gearboxes based on DFIG stator current envelope analysis," *IEEE Transactions on Sustainable Energy*, vol. 10, no. 3, pp. 1044–1053, Jul. 2019, Conference Name: IEEE Transactions on Sustainable Energy, ISSN: 1949-3037. DOI: 10.1109/TSTE.2018.2859764.

[73] H. Xiao, X. Zhou, and Y. Shao, "Application of an improved dynamic time synchronous averaging method for fault diagnosis in conditions of speed fluctuation and no tachometer," *Proceedings of the Institution of Mechanical Engineers, Part C: Journal of Mechanical Engineering Science*, vol. 230, no. 14, pp. 2517–2531, Aug. 1, 2016, Publisher: IMECHE, ISSN: 0954-4062. DOI: 10.1177/0954406215597956. [Online]. Available: https://doi.org/10.1177/0954406215597956 (visited on 07/13/2023).

[74] P. C. Krause, "Method of multiple reference frames applied to the analysis of symmetrical induction machinery," *IEEE Transactions on Power Apparatus and Systems*, vol. PAS-87, no. 1, pp. 218–227, Jan. 1968, Conference Name: IEEE Transactions on Power Apparatus and Systems, ISSN: 0018-9510. DOI: 10.1109/TPAS.1968.291992.

[75] S. M. A. Cruz and A. J. M. Cardoso, "Multiple reference frames theory: A new method for the diagnosis of stator faults in three-phase induction motors," *IEEE Transactions on Energy Conversion*, vol. 20, no. 3, pp. 611–619, 2005, ISSN: 0885-8969. DOI: 10.1109/tec.2005.847975. [Online]. Available: https://dx.doi.org/10.1109/tec.2005.847975.

[76] P. F. C. Gonçalves, S. M. A. Cruz, and A. M. S. Mendes, "Multistage predictive current control based on virtual vectors for the reduction of current harmonics in six-phase PMSMs," *IEEE Transactions on Energy Conversion*, vol. 36, no. 2, pp. 1368–1377, Jun. 2021, Conference Name: IEEE Transactions on Energy Conversion, ISSN: 1558-0059. DOI: 10.1109/TEC.2021.3055340.

Appendix A

Co-simulation Details

This appendix discloses the details of the co-simulation that was implemented in Ansys/Simplorer and MATLAB/Simulink to validate the proposed fault diagnosis methods presented in Chapter 3 whose results where discussed in Chapter 4. The parameters used in this co-simulation are also listed in this appendix

A.1 6-PMSM and PCC Strategy Models

The global view of the circuit schematic in Simplorer that connects the 6-PMSM model (FEA block) and the control strategy (C Model), is presented in Fig. A.1. The 6-PMSM model has its stator windings resistances and inductances outside the FEA block, making it possible to implement short-circuit between turns. In the illustrated schematic the fault resistance was added to the seven short-circuited turns scenario. The C Model block has the .dll file that contains the control strategy implemented in MATLAB/Simulink. The global view of this control strategy is presented in Fig. A.2.

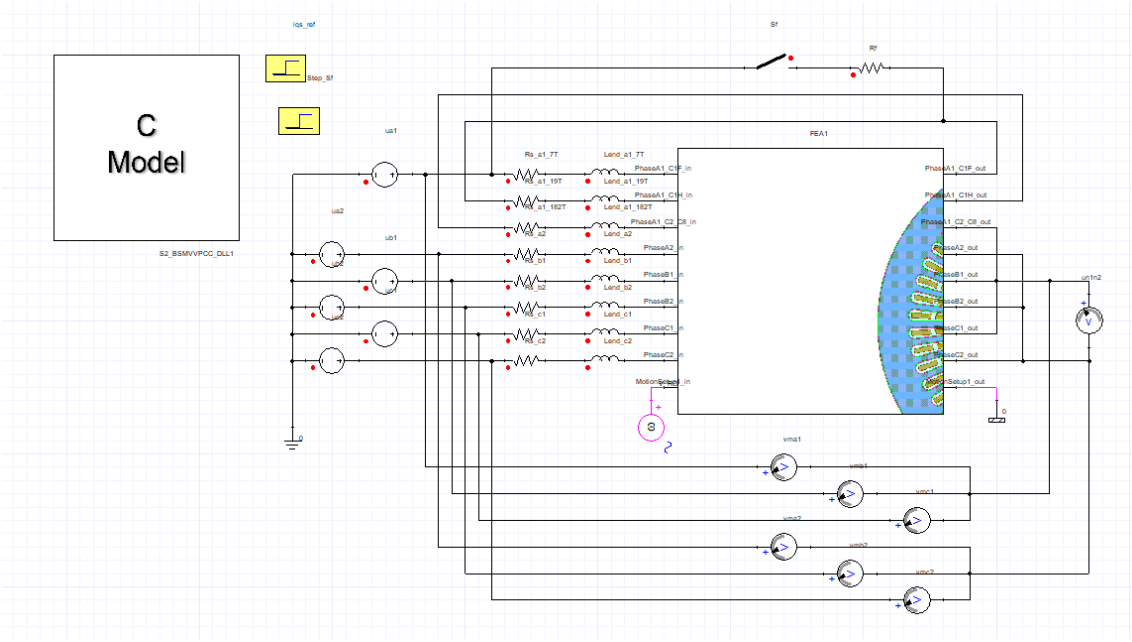

Figure A.1: View of the 6-PMSM model implemented in ANSYS/Simplorer.

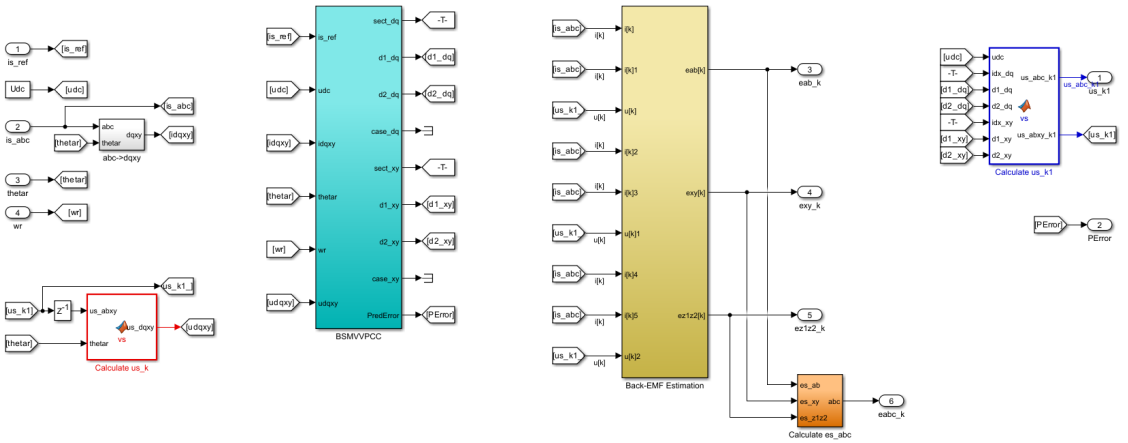

Figure A.2: View of the predictive current control strategy already available in MATLAB/Simulink, together with the developed back-EMF estimation block.

A.2 Simulation Parameters

In Table A.1 the parameters used in this co-simulation are displayed.

Table A.1: Parameters used in MATLAB/Simulink.

Parameter	Symbol	Value
Sampling Period	T_s	125 μs
Rated Voltage	U_{dc}	650 V
Pole-pairs	p	2
Stator Resistance	R_s	1.6 Ω
Inductance in the dq subspace	L_dq	53.51 mH
Inductance in the xy subspace	L_xy	2.48 mH
Inductance in the z1z2 subspace	L_z1z2	7.94 mH

Appendix B

Experimental Rig

This appendix presents in greater detail the experimental setup used to acquire the experimental results presented in Chapter 5.

B.1 Drive Overview

The experimental rig in this dissertation requires a voltage level of 650 V on the dc-link, and so, a 6 kVA step-up power transformer is connected to the standard three-phase grid of 400 V (50 Hz) to supply this setup. A 17.5 kVA auto-transformer is then employed to manually adjust the supply voltage of the diode bridge rectifier and thus adjust the dc-link voltage level.

In order to rectify the AC voltage supplied by the auto-transformer, a six-pulse diode bridge rectifier is used. This rectifier bridge, model VUO82-12N07 from INXYS, has a maximum repetitive reverse voltage of 1.2 kV and a maximum average forward current of 88 A.

The dc-link capacitors consist of two electrolytic capacitors from EPCOS (B43456 series) with a capacitance of 6800 μF, rated voltage of 400 V, and an equivalent series resistance of 0.024 Ω. To handle a dc-link voltage level of 650 V, the two capacitors are connected in series, and thus the equivalent capacity of the dc-link is reduced to 3400 μF.

The 2L-VSIs that power 6-PMSM consist of two Semikron SKiiP 132 GD120 - 3DUL converters, which use IGBTs with a maximum collector emitter voltage of 1.2 kV and a rated collector current of 150 A. The two three-phase power converters are connected to the same dc-link, using a single dc-link configuration.

B.2 Parameters of the Electric Machines

The 6-PMSM is mechanically coupled to a three-phase induction machine (IM) (Fig. B.1), used as load. The nameplate parameters of the 6-PMSM are presented in Table B.1 as well as the IM nameplate parameters in Table B.2.

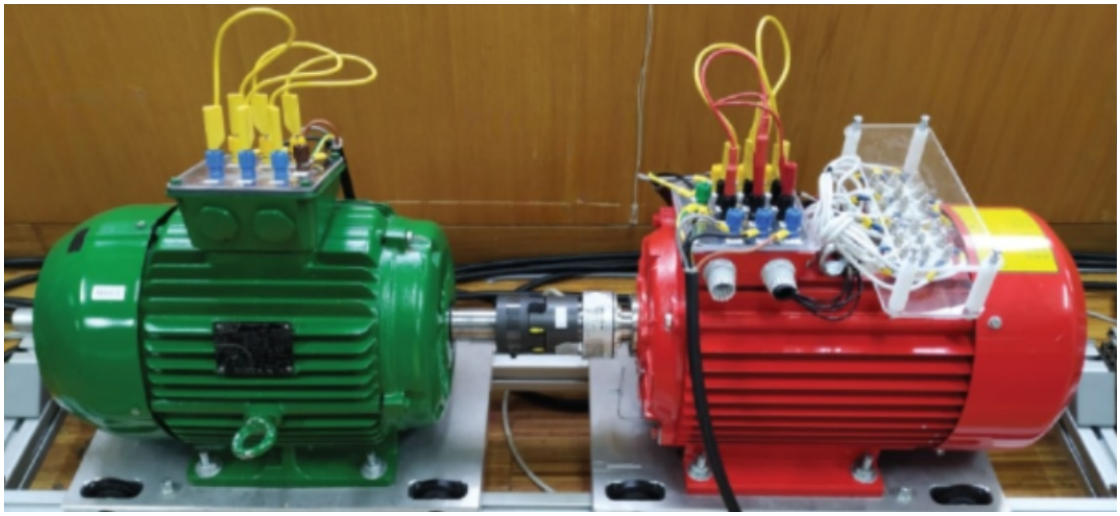

Figure B.1: View of the 6-PMSM coupled to the 3-IM with the incremental encoder.

Table B.1: Nameplate parameters of the 6-PMSM.

Parameter	Symbol	Value
Rated Power	P_n	4 kW
Rated Voltage	U_n	340 V
Rated Current	I_n	4.8 A
Rated Speed	n_n	1500 rpm
Rated Frequency	f_n	50 Hz
Efficiency	η	95%
Frame Size	FS	132M
Pole pairs	p	2
Permanent Magnet Flux	Ψ_{PM}	0.97 Wb

Table B.2: Nameplate parameters of the induction machine.

Parameter	Symbol	Value
Rated Power	P_n	7.5 kW
Rated Voltage	U_n	380 V
Rated Current	I_n	14.4 A
Rated Speed	n_n	1460 rpm
Rated Frequency	f_n	50 Hz
Power Factor	PF	0.87
Efficiency	Eff.	91.2% (IE3)
Number of phases		3
Frame Size	FS	132M-04
Ingress Protection	IP	55
Insulation Class	INS. CL	F
Temperature Rise	$\Delta\, t$	80 k
Ambient Temperature	AMB.	40° C
Service Duty	S	1
Service Factor	SF	1

B.3 Other Components

The IM is supplied by a CFW11 variable speed drive from WEG (Fig. B.2(a)), which is operated in speed mode to control the rotational speed of the 6-PMSM (Fig. B.2(b)). In addition, the rotor position of the six-phase PMSM is measured with an Hengstler incremental encoder (RI 76TD) with 2048 pulses per revolution.

(a) (b)

Figure B.2: CFW11 variable speed drive that supplies the IM (a) and remote speed controllers to control the rotational speed of the 6-PMSM (b).

A circular rheostat from OFICEL, with a power rating of 1kW and a maximum resistance of 5 Ω is used as a variable-resistance for the fault resistance of the ITSC (Fig. B.3(a)). The measurement circuit (Fig. B.3(b)), with a voltage gain of 65 and a current gain of 3, is used to measure the fault current and voltage.

(a) (b)

Figure B.3: Variable-resistance load used as fault resistance (a) and current and voltage sensors used to measure the fault current and voltage (b).

The control strategy and the developed back-EMF estimation and MRF-based fault diagnostic method are programmed into the DS1103 control platform using MATLAB/Simulink

and the dSPACE RTI library. This implementation is shown in Fig. B.4. The "Measurements" block handles the measured signals. The "Speed" block calculates the PMSM rotor speed in rpm from the rotor position, measured with the incremental encoder, and is executed with a sampling period ten times higher than the control sampling period (T_s). The PCC strategy is implemented within the "PCC" block and maintains the same structure as implemented in the simulation model shown in Fig. A.2. Finally, the "Write digitalPort" block contains the implementation of the communication protocol with the cRIO-9066.

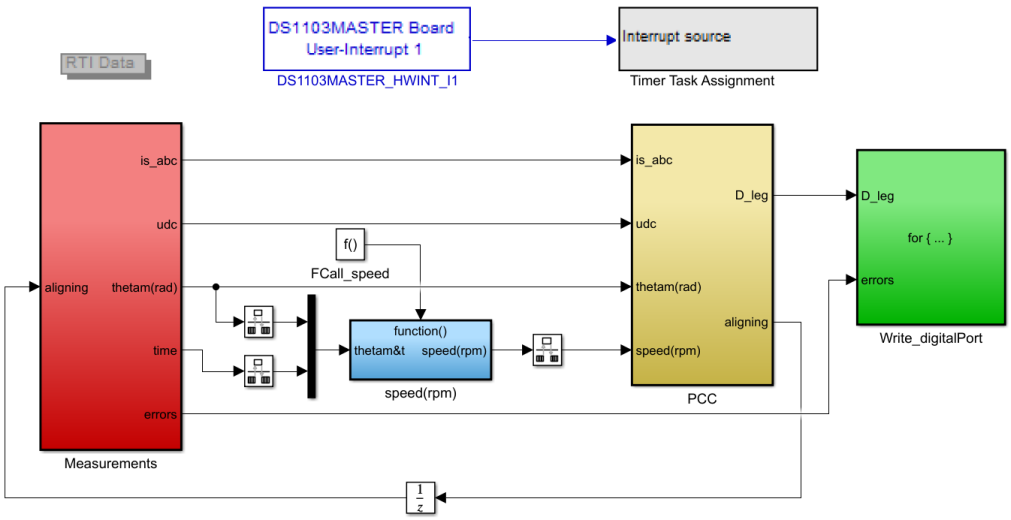

Figure B.4: View of the model in MATLAB/Simulink with the PCC strategy that allows the implementation of the back-EMF estimation as well as the MRF-based fault detection method into the dSPACE DS1103.

To enable the control and monitoring of the control strategy in real-time, a control panel was used through the ControlDesk software. In addition to displaying the variables of interest of the drive (measured or calculated), the control panel allows changing current references in real-time and acquiring the displayed variables. This control panel is shown in Fig. B.5.

The modulator, which generates the switching signals for the power converters, is implemented in the cRIO-9066 controller using LabVIEW. The front panel of the implemented modulator is shown in Fig. B.6.

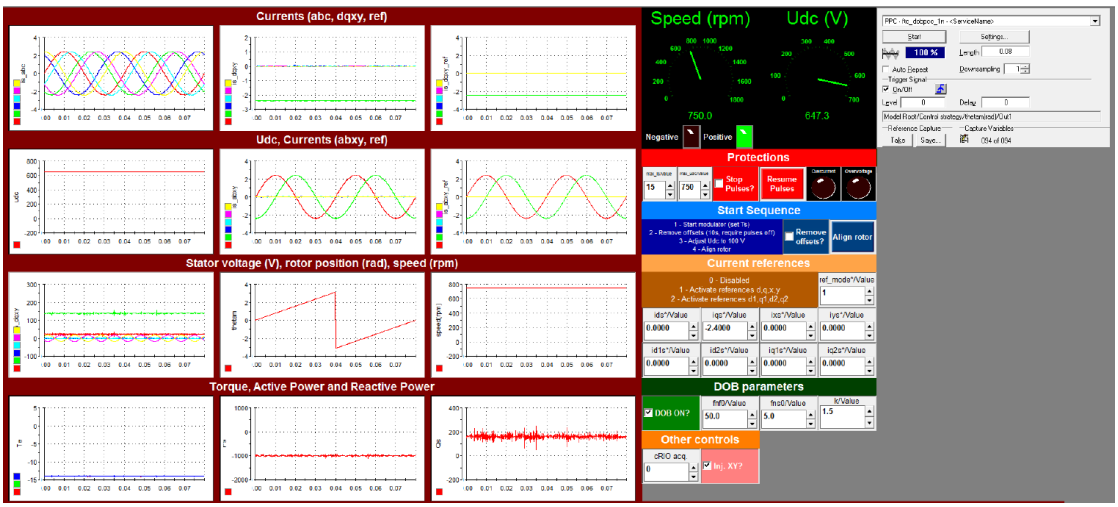

Figure B.5: Control panel implemented with ControlDesk software.

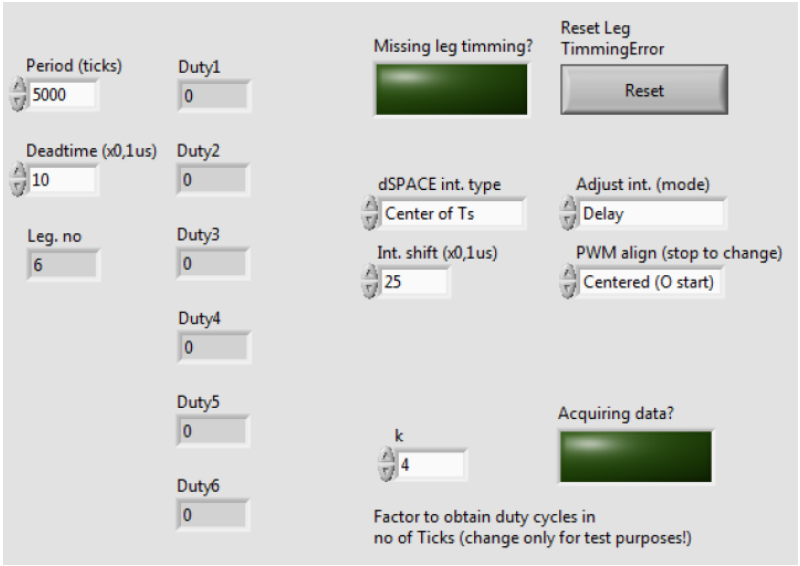

Figure B.6: Front panel in labVIEW to monitor and control the modulator running in the cRIO-9066.